Studies on Pulsed Laser Deposited Ruby and Barium Titanate Thin Films for Tunable Optical Delay and Temperature Sensing Applications

A Thesis Submitted in partial fulfillment of the requirements for
the award of the degree
of

DOCTOR OF PHILOSOPHY

by

SATCHI KUMARI

DEPARTMENT OF PHYSICS
INDIAN INSTITUTE OF TECHNOLOGY GUWAHATI
GUWAHATI-781039, INDIA
JUNE 2013

Dedicated to my Parents

Satchi Kumari
Resistatrion No. 08612110
Department of Physics
Guwahati 781039, India

STATEMENT

I hereby declare that the matter embodied in this thesis is the result of investigations carried out by me at the Department of Physics, Indian Institute of Technology Guwahati, Guwahati, India, under the supervision of **Prof. Alika Khare**. This thesis has not been submitted to any university/ institute or elsewhere for the award of the any degree, diploma or associateship.

Date: **Satchi Kumari**

भारतीय प्रौद्योगिकी संस्थान गुवाहाटी
Indian Institute of Technology Guwahati
Department of Physics
Guwahati-781039, Assam State, INDIA
Phone: +91 361 2582705, 2582701, 2690321 to 328 (extn. 2705),
Fax: +91 361 2582749
Dr. Alika Khare
Professor
E-mail: alika@iitg.ernet.in, k_alika@yahoo.com

Date: June , 2013

Certificate

This is to certify that work contained in the thesis entitled '**Studies on Pulsed Laser Deposited Ruby and Barium Titanate Thin Films for Tunable Optical Delay and Temperature Sensing Applications**' by **Ms Satchi Kumari** (Roll no. 08612110), a student of Department of Physics, Indian Institute of Technology Guwahati, for the award of degree of Doctor of Philosophy, has been carried out under my supervision and that the same has not been submitted elsewhere for a degree.

(Alika Khare)

ACKNOWLEDGEMENT

First and foremost I would like to express my sincere thanks towards my thesis supervisor, Prof. Alika khare for her enthusiasms and support during my Ph. D. Her deep knowledge of many fields has been an invaluable resource. Her intense curiosity towards research had been always inspiring for me. I consider it a great privilege to be her student and will fondly remember the time I spent in her lab. Apart from professional suggestions she gave me personal care and strengthened my skills in various ways.

I am thankful to my doctoral committee members, Dr. Pratima Agarwal, Dr. Ashish Kr. Gupta and Dr. Amarendra Kr. Sarma for timely reviewing progress of my thesis and providing valuable suggestions which steered the thesis in right direction. I owe my thanks to H.O.D, Department of Physics, IIT Guwahati for providing me the necessary facilities to fulfill my PhD thesis objectives. I am also thankful to CIF IIT Guwahati for instrumentation facilities. In particular, I would like to extend my sincere thanks to Mr. Chandan Burgohain, Mr. K. K. Senapati, Dr. Sidananda Sarma, Mr. Atul Chandra Deka, Mr. Bimal Kumar Sarma and Mr. Madhurjya Borah for their kind help with various instruments. I would like to thank material science lab, Dept. of mechanical engineering, for providing optical micrograph and furnace facilities.

I would like to thank Department of science and technology, New Delhi, for providing me the financial assistance during my thesis work.

It has been pleasure to work with my research lab members Gaurav, Arpita, Archanadi, Abu, Indrajeet, Poulami, Partha, Gyan, Shanta, Rahul and Prahlad. Thanks to them for their suggestions, time, help in experiments and kindness throughout my PhD.

I am deeply indebted to all my friends' Himanshu, Prabhakar, Meenu, Mayadi, Mukesh, Onkar, Nisha and Asha at IIT Guwahati for making me feel like at home during all these years. I am thankful to my friends Anupam, Aaparajita and Mukesh. I must acknowledge all my friends for their love, encouragement and support.

I want to thank my best friend and fortunately my husband Dr. Dilip Kumar Singh for his unconditional love and support. He always overestimated my capabilities and boosted me to face challenges of life with lots of patience, dignity and hope. I want to thank all my family members for loving me so much. My papa and mummy, for keeping faith in me. My sisters Annu di and Aruna di for their love and care, and my sweet brother Rakesh for all the humors and fun, for bringing smile on my face. My father-in–law and my mother-in-law for giving me an important place in their life. My sister-in-law Kiran, Neha, Kushboo, Shikha and Chanda, for loving me so much. My brother in-laws Shekher, Munna, Siki and Bittu for being so humors and nice with me.

Finally, I express my sincere thanks to all who helped me in whatever form during my stay at IIT Guwahati and successful completion of this thesis.

ABSTRACT

The present work aimed towards deposition of high quality ruby ($Al_2O_3:Cr^{3+}$) and barium titanate (BTO) thin film via pulsed laser deposition (PLD) technique, for optical delay and temperature sensing applications.

The ruby thin film was deposited as a function of substrate temperature, laser fluence, oxygen gas pressure and deposition time on quartz as well as sapphire substrate.The quality of film deposited via PLD depends on laser produced plasma (LPP). Therefore, LPP of ruby plasma has been studied by using planar copper Langmuir probe. The optimum deposition parameters obtained for the growth of highly C-axis oriented film of ruby were laser fluence ~ 23 J/cm^2, gas pressure ~ 5 mbar and deposition temperature ~ 750° C. At optimum deposition parameters, epitaxial ruby thin film of thickness ~ 3500 nm was deposited on both side polished sapphire substrate for a deposition time of 6 hrs.The R-line width of this film was ~ 11.7 cm^{-1}, comparable to single crystal of ruby, confirms highly crystalline nature of PLD ruby film. The nonlinear absorption coefficient and nonlinear refractive index of the film was measured using Z-scan technique. The film was subjected to optical delay studies using 200 ns Gaussian pulse from Nd:YAG laser (532 nm) via degenerate two-wave mixing setup. Delay of 17 ns and pulse advancement of 12 ns corresponding to a group velocity of 205.9 m/s and -291.7 m/s at +45° and -45° film orientation, respectively was observed. The temperature dependence of R_1 and R_2 line of epitaxial ruby thin film via PLD confirms its application as a photonic temperature sensor.

Polycrystalline BTO thin film with tetragonal phase was deposited via PLD. The nonlinear coefficient of BTO film having thickness ~ 3300 nm was measured using Z-

scan technique. This film was subjected to optical delay studies using the same setup as that of used for ruby film. Subluminal as well as superluminal pulse propagation was observed on tuning the film orientation. The temperature dependent Raman spectrum of the BTO film was studied from 146 K - 506 K. This showed that BTO thin film can be explored as Raman temperature sensor.

The optical delay was also studied in Ce:BaTiO$_3$ crystal using millisecond pulses of CW He:Ne laser (632.8 nm). Effect of signal pulse width, pump intensity, pump-signal polarization and crystal orientation on optical delay is systematically performed in the BTO crystal.

Contents

3. Laser induced plasma of Ruby 41

4. Pulsed laser deposition and characterization of Ruby thin film 57

List of figures

List of Tables

ABBREVIATIONS

A	Aperture
AFM	Atomic force microscopy
ATCC	Automatic target carrousel control
BS	Beam splitter
BTO	Barium titanate
CPO	Coherent population oscillation
DL	Double layer
DSO	Digital storage oscilloscope
EIT	Electromagnetically induced transparency
FWHM	Full Width at Half Maximum
GS	Glass plate
HRTEM	High resolution Transmission Electron microscopy
L	Lens
LIBS	Laser induced breakdown spectroscopy
LO	Longitudinal optical
LPP	Laser produced plasma
M	Mirror
MgO	Magnesium oxide
NDF	Neutral density filter
NDTWC	Non-degenerate two-wave coupling
NLO	Nonlinear optics
OES	Optical emission spectroscopy
PD	Photodiode
PL	Photoluminescence
PLD	Pulsed laser deposition
PR	Photorefractive
RF	Radio frequency
RT	Room temperature
SBS	Stimulated Brillion scattering
SCCM	Standard cubic centimeters per minute
SRS	Stimulated Raman scattering
TEM	Transverse electromagnetic wave
TO	Transverse optical
TOF	Time of flight
TPA	Two-photon absorption
TWM	Two-wave mixing
UV	Ultra Violet
XRD	X-Ray Diffraction

SYMBOLS

α	Absorption coefficient
β	Nonlinear absorption coefficient
n_2	Nonlinear refractive index
I_s	Signal intensity
N_g	Ground state population
τ	Life time of metastable state
n_r	Real part of refractive index
$n_r(\omega)$	Frequency dependent refractive index
$\sigma_t(\omega)$	Frequency dependent absorption Cross section
T_s	Substrate temperature
k	Boltzmann constant
h	Planck’s constant
N_e	Electron density (of laser induced Plasma)
T_e	Electron temperature (of laser induced Plasma)
λ	Wavelength
ω	Angular frequency of laser
L_{eff}	Effective sample length
z_o	Rayleigh length
w_o	Beam diameter at focus
f	Focal length
T_{open}	Open aperture transmittance
T_{closed}	Closed aperture transmittance
D	Laser beam diameter
ε	Second order dielectric tensor
Δn	Change in refractive index
Δt	Time delay between reference and signal pulse
r_{eff}	Effective electro- optic coefficient
I_i	Saturation current for ion
I	Probe current
I_s	Signal beam intensity
I_p	Pump beam intensity
V_p	Floating potential
A	Area of probe
$\chi^{(3)}$	Third order nonlinear Susceptibility
n_o	Linear refractive index
c	Speed of light
v_i	Electron and ion velocities
d	Distance of the probe from the target

t	Time taken by the maximum number of electron/ions to reach the probe surface
v_g	Group velocity inside PR medium
R	Reflectivity
e	Electronic charge
n_i	Ion density
T	Transmittance
I_0	Peak irradiance at the centre of focal spot
z	Position of sample w.r.t. the focal spot
E	Space charge electric field
L	Propagation distance of signal beam inside crystal
I_b	Transmitted signal during grating buildup
I_b^o	Transmitted signal after completion of grating buildup
I_d	Transmitted signal during grating decay
I_d^o	Transmitted signal after completion of grating decay
τ_1	Grating build up time
τ_2	Grating decay time
α_s	Angle between propagation vectors of signal & pump beam for S-polarization
α_p	Angle between propagation vectors of signal & pump beam for P-polarization
n_e	Extraordinary refractive index
Δk	Phase mismatch
κ	Coupling constant
η_1	Index modulation of volume index grating

Chapter 1

Introduction

Ruby crystal is a well- known lasing material delivering high power laser in R_1 & R_2 lines at 694.2 nm and 692.8 nm respectively **[1-4]**. It possesses favorable combination of relatively narrow line width, a long fluorescence lifetime, high quantum efficiency, and broad and well-located pump absorption bands **[5-7]**. It consists of chromium doped in alumina sites ($Al_2O_3:Cr^{3+}$). The energy levels of Cr^{3+} ion gives rise to R-line transition. The R-line of ruby is also accompanied by nearby red shifted weak bands in both emission and absorption spectra, these bands are referred as vibronic side bands **[8-10]**. These are predominantly one-phonon transition. This fact makes ruby well suited for phonon-spectroscopy by optical means, which can be used as a detector or tunable generator for high frequency phonons **[10]**. The dependence of intensity, wavelength and fluorescence lifetime of R_1 and R_2 line on temperature and pressure makes the basis for ruby as a variety of photonic sensor for various applications **[11-19]**. Single crystal of ruby is shown to act as fiber optic thermometer **[13, 14]**. It has also been used as ion-irradiation damage sensor **[15]**. In ruby, avalanches of phonons take place by stimulated emission within the Zeeman-spilt ^2E levels **[16-17]**. Therefore, it can also behave as a SASER (Sound amplification by stimulated emission of radiation) **[18]**. Thus, ruby can act as photonic based temperature, stress and acoustic sensor **[20-26]**. Apart from sensing applications, ruby is a very good candidate to study nonlinear optical effects **[27-34]**. It exhibits transverse self -phase modulation, two-wave mixing, non-degenerate two-wave mixing and spectral hole burning [**29, 30, 32, 34**]. It is a well know saturable absorber [**35**]. It is documented that when a modulated laser beam passes through a ruby crystal, it increases the modulation depth and introduces a phase delay of this modulation **[35]**.

Recently, subluminal as well as superluminal pulse propagation at room temperature has been demonstrated in ruby crystal **[36-39]**. Slowing down of light to 57.5±0.5 m/s is demonstrated by Bigelow et al. in a ruby crystal of length 7.25 cm **[37]**. When a TEM_{00} beam is introduced in ruby, various phenomenon; population oscillations, self-phase modulation, Fraunhofer diffractions and non-degenerate two-wave coupling mechanism competes with each other and brings a new phenomenon of self-superluminal group velocity propagation **[38]**. Slowing down at room temperature in solid state material has enormous application in the field of nonlinear optics [**40-42**].

Another solid state material, in which very large optical delay of light has been observed at room temperature, is photorefractive barium titanate (BTO) crystal in tetragonal phase **[43-46]**. It is one of the most promising ceramic for nonlinear optics (NLO) and electro-optic applications in bulk as well as in the form of thin film in tetragonal phase **[47-52]**. At low temperature, barium titanate shows phase change from low temperature rhombohedral to high temperature cubic phase **[53-55]**. It has very high value of electro-optic coefficients, fast response time and excellent phase conjugate reflectivity **[47-48]**. Large electro-optic coefficient allows one to achieve very high gain in two-beam coupling and optical amplification at low power of laser. It exhibits two-wave mixing, four-wave mixing, slow and fast light etc. in the tetragonal pervoskite phase at room temperature **[48, 43-46]**. Light speed reduction to 0.025 cm/s was observed experimentally in barium titanate crystal **[43]**. Fast light was also reported in barium titanate crystal for gravitational wave detection **[46]**. The slow-light based devices can find application in optical router, quantum computation, micro-wave photonic devices, solar cell etc. [**40-42, 56-60]**. It can act as a variable optical delay device. Various mechanisms responsible for the optical delay or slow/fast light are briefed in the following section.

1.1 Optical delay of light

Slow and fast light is generated due to group velocity dispersion inside the medium. Various mechanisms responsible for the production of slow and fast light are electromagnetically induced transparency (EIT) **[61-67]**, stimulated Brillion scattering (SBS), stimulated Raman scattering (SRS) **[68-81]**, passive and active manipulation in periodic structures and resonators **[82-83]**, photorefractive (PR) two wave mixing **[43-46, 84-88]**, coherent population oscillation (CPO) **[36-37, 89-90]**, saturation absorption **[91-98]** etc.

The first experimental observation of light speed reduction to 17 ms^{-1} was demonstrated in ultra-cold atomic gas of sodium via EIT **[99]**. The first solid state material demonstrating the slowing down action was a crystal of Pr doped Y_2SiO_5, maintained at cryogenic temperature of 5 K **[100]**. The mechanism of slowing down action of light was based on EIT and speed reduction was reported to be 45 ms^{-1}. Subsequently, there were many reports on slowing down based on EIT [**61-67**]. The initial observations on slowing down of light, involved complicated experimental setup and the requirement of single frequency laser with a bandwidth ~ MHz or less **[99-100]**, put serious limitations onto its practical utility. Later on, ultraslow light propagation in solids at room temperature via temporal evolution of the photorefractive (PR) grating in a degenerate two-wave mixing process was reported in a relatively simple experimental setup [**84-88**]. Crystal of $LiNbO_3$, $BaTiO_3$, SBN, BSO, GaAs, InP etc. have been used to control the group delay as well as advancement for the demonstration of slow and fast light respectively via photorefractive effect **[43-46, 84-88, 101]**. The group delay via coherent population oscillation is another promising mechanism at room temperature in solids **[36-37]**. Slow light propagation with a group velocity of ~ 57.5 ± 0.5 m/s in a ruby crystal at room temperature was demonstrated by Bigelow et.al. **[37]** via coherent population oscillations. Slow light based on CPO mechanism is being demonstrated in semiconductor quantum wells and quantum dots also **[89-90]**. Optical delay can also be observed via saturation absorption **[91-97]**.

1.1.1 Mechanism for studying group delay in solids at room temperature

The optical delay can be easily demonstrated in solid state materials at room temperature in a relatively simple experimental setup via photorefractive degenerate two-wave mixing, coherent population oscillations (CPO) and saturable absorption. The details of these mechanisms are explained in the subsequent sections.

1.1.1.1 Photorefractive degenerate two-wave mixing

In photorefractive (PR) two-wave mixing (TWM) [**102-108**], a strong pump beam and a weak signal beam is incident on a PR crystal as shown in figure 1.1 (a). Interference between the beams results in a pattern of periodic dark and bright fringes within the crystal as shown in figure 1.1 (b)_(i). In the regions of bright fringe, electrons undergoes photo excitation from an impurity level to the conduction band of the material, leaving behind a hole. Once in the conduction band, the electrons are free to move and diffuse throughout the crystal. Since the electrons are being excited preferentially in the bright fringes, the net electron drift is towards the region of dark-fringe. While in the conduction band, the electrons may with some probability recombine with the holes and return back to the impurity levels. The rate at which this recombination takes place

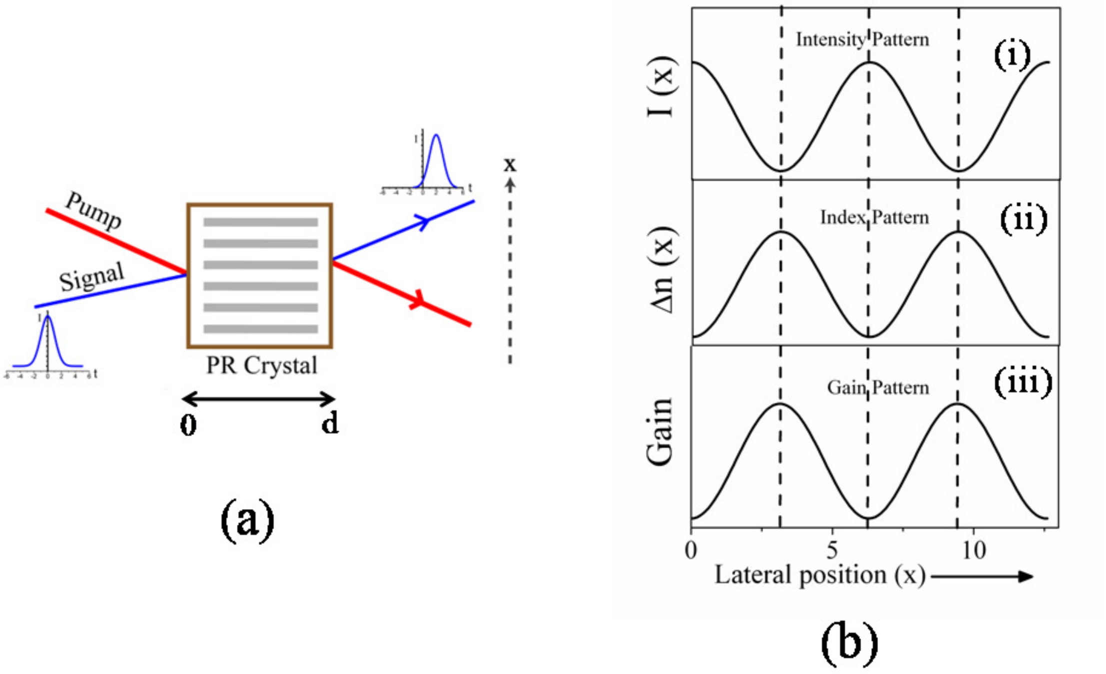

Figure 1.1 *(a) Schematic of TWM in PR crystal, (b) (i) intensity pattern (ii) refractive index pattern and (iii) gain pattern.*

determines how far the electrons diffuse, and thus the overall strength of the coupling between pump and signal beam inside the PR medium is determined. The net redistribution of electrons into the dark regions of the material, leaving behind holes in the region of bright fringes inside the crystal, gives rise to an electric field, known as space charge field. The internal space charge field, via the Pockel's effect, causes the refractive index of the crystal to change. Thus a spatially varying refractive index grating is formed inside the crystal as shown in figure 1.1 (b)_(ii). The refractive index grating is 90° shifted w.r.t. the intensity pattern, as a result, the pump energy will be diffracted along the signal beam and the transmitted signal beam will get amplified and delayed.

The delay in the transmitted signal beam is observed due to phase shift of beam inside the PR medium resulted from refractive index modulation [**43-44**]. The amplification of the signal beam due to energy transfer from the pump beam is known as gain and defined as; ratio of transmitted signal beam by travelling a distance L inside the crystal, in pump on condition and pump off condition, given by equation (1.1).

$$Gain(g_{TWM}) = \frac{I_S(L)\ with\ pump\ on}{I_S(L)\ with\ pump\ off} \tag{1.1}$$

The gain pattern in the medium developed due to refractive index pattern is shown in figure 1.1 (b)_(iii). The energy from pump is transferred to signal depending upon the coupling of these two beams known as photorefractive two-wave mixing. The output intensity, phase and gain of pump and signal beam depends upon various input parameters viz. nonlinear refractive index of PR medium, electro-optic coefficient of PR crystal, length of crystal (d), crystal orientation, polarization states of pump and signal beam etc. The amplification and delay of signal beam in photorefractive two-wave mixing can be tuned by varying these inputs parameters [**84-85, 101**].

1.1.1.2 Coherent population oscillation

Coherent population oscillation (CPO) is another mechanism for demonstrating slowing down of light in solids at room temperature. In ruby crystal, slowing down via CPO is experimentally and theoretically reported **[36, 37, 39]**. Ruby is a three level system as shown in figure 1.2. When a laser beam in resonant with 1→3 transition, is launched, the ground state population density (N_g) gets depleted due to excitation to the pump band 3. In a time scale of 1.1 ns it decays from level 3 to level 2. The life time of level 2, τ_2~ 3 ms. Due to the longer lifetime of the level 2 the ground state population remains depleted. Therefore, the further absorption of the pump beam is reduced. Later on, the medium recovers the population of the ground state by 2→1 transitions, in a time scale of the order of 3 ms and this cycle continues. Therefore, the ground state population oscillates between level 1 & 2.

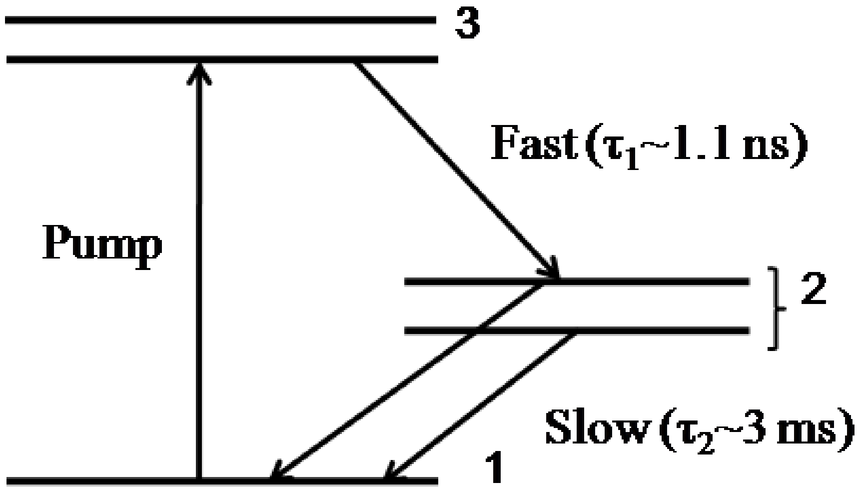

Figure 1.2 *Schematic of two-level system.*

The ground state population, N_g is related to the real part of refractive index n_r by Kramers-Kronig relation equation (1.2) [**39**].

$$n_r(\omega) = 1 + \frac{cN_g}{\pi} \int_0^{\infty} \frac{\sigma_t(\omega')}{\omega' - \omega^2} d\omega' \tag{1.2}$$

Where, $n_r(\omega)$ is the frequency dependent real part of refractive index, c is the velocity of light in vacuum, N_g is the ground state population of Cr^{3+} ions, $\sigma_t(\omega')$ is the frequency dependent absorption cross section. Thus, population oscillations produce rapid variation of refractive index. This results in optical delay of the propagating beam.

1.1.1.3 Saturable absorption

Apart from CPO, the other mechanism which could be responsible for optical delay in ruby is saturable absorption [**91**]. The narrowing, skewing and the time delay of pulse has been explained by A. C. Selden, based on the theory of saturable absorption [**92, 95-97**]. In this process, the absorption of the medium reduces when a laser pulse with intensity higher than the saturation intensity passes through it. Therefore, a pulsed laser passing through such medium undergoes modulation in intensity. The transmitted pulse shows phase shift and hence optical delay w.r.t. the pulse travelling in air. In case of ruby, the optical delay is observed with laser pulses of duration larger or comparable to the lifetime of metastable state (~ 3 ms). For short laser pulses having pulse duration smaller than the lifetime of excited state, saturation can even be achieved when the peak power of laser pulse is larger than the saturation intensity of medium [**98**] and hence optical delay can be observed via saturation absorption [**95**] even with the laser pulse of duration shorter compared to the lifetime of state.

1.2 Photonic temperature sensors

Temperature measurement is a key issue in many devices. Various types of temperature sensors are designed to serve this purpose **[109-114]**. Thermocouple and diode sensors are not suitable in RF environment due to electromagnetic perturbation. Photonic sensors offer alternative solution, as these are immune to electromagnetic interference, small in size and robust. Optical fibres have shown to act as a photonic temperature sensor but it cannot be used at very high temperatures **[115-124]**. Temperature sensing using luminescence lifetime measurement was reported in $LaF_3:Er^{3+}$ **[125]**. But this sensor can only work in the high temperature range. Bulk ruby crystal has been reported as a photonic temperature sensor over a broad range of temperature measurement from 0 K to 600 K **[11]**. Its temperature sensing capability is based on the dependence of R-line position on the temperature **[11]**. The quantum efficiency of R-line fluorescence is very high and thus offers high signal to noise ratio. It is known to be among the hard materials and hence can be used even in the harsh environment **[2]**. It can be used in compact photonic circuits and opto-electronic chips. Melting point of ruby is 2044 ˚C **[2]** and hence can be used in high temperature environment. For an ideal thin film photonic temperature sensor, R-line fluorescence of ruby should be very strong, line-width should be narrow and sensitivity of the sensor should be linear. The fluorescence line-width of R-line in ruby depends on crystal perfection, stress, strain and temperature **[126]**. Therefore, the grown film for temperature sensing application should be highly crystalline, uniform and free from stress and strain. Any inhomogenity and stress in the deposited film will cause additional line broadening apart from the temperature dependent contribution and hence will reduce the accuracy of measurement **[127]**.

Another suitable candidate which can be used as a photonic temperature sensor in the harsh environment is barium titanate. The Raman bands of BTO are temperature sensitive. The intensity and FWHM of 308 cm^{-1} LO band of BTO show temperature dependence. Therefore, it is suitable for temperature sensing applications [**54**].

For coupling the technology of optical delay line and photonic based temperature sensor in device, the medium should be miniaturized in the form of a thin film. Ruby and barium titanate (BTO) can be two potential materials in which pulse propagation as well as temperature sensing can be explored in the thin film geometry. The deposition of ruby thin film has been reported by solid phase epitaxy **[128]**, electron beam evaporation **[129]**, chemical vapor deposition **[130]** and pulsed laser deposition technique (PLD) **[131]**. Out of these, PLD is the most promising technique for deposition of crystalline thin films of ruby as well as BTO [**132-141**].

1.3 Pulsed laser deposition technique for thin film growth

Pulsed laser deposition technique is the most suitable technique for growth of stoichiometric thin films of wide range of materials; metals, semiconductors, ceramics, etc. **[142-158]**. This technique provides tunability over a large range of physical and chemical properties of the deposited thin films by controlling the process parameters; target composition, laser fluence, pulse repetition rate, background gas pressure and target-substrate distance **[151-153]**. The advantage of PLD technique over other deposition techniques includes its simplicity, adaptable to various operational modes, and effective in synthesizing thin films of complex composition. PLD was first proposed in the early 1960's and was demonstrated in 1965 by Smith and Turner **[159]**. In 1980's PLD emerged as a powerful technique for deposition of various functional materials, multilayer, hetero-structures and nanostructures **[160-169]**. Highly crystalline and C-axis oriented thin film of various ceramic materials has been successfully deposited via PLD technique **[52, 54, 170-176]**.

In PLD technique, a high power laser is focused on a suitable target placed inside the laser ablation chamber as shown in figure 1.3 **[149-153]**. The focusing of high power laser results into formation of plasma of the target material which expands in the presence of background gas, undergoes dynamical and chemical changes and then finally deposited in the form of thin film on a substrate placed few centimetre away from the target. The substrate is usually mounted on a substrate assembly with a provision of controlling the temperature during deposition. The ablation chamber is initially evacuated to a base pressure of ~10^{-6} mbar. Depending upon the requirement for a particular film, background gas is purged inside the vacuum chamber using appropriate gas inlet ports. The quality of deposited film depends upon the laser fluence, gas pressure, substrate temperature, target-substrate distance, etc. The dynamics of deposition of ceramic thin films via PLD technique is quite complex **[158]**. The deposition is normally performed at a laser fluence > 10^8 W/cm^2. In this fluence regime, the initial absorption of the radiation is dominated by multiphoton absorption. This causes the mutiphoton ionization of the target atom/molecules resulting in emission of positive ions and electrons. This results into plasma formation of target material in the focal regime of the laser. The plasma expands in the presence of background gas and the expanding plasma absorbs further energy from the laser via inverse bremsstrahlung

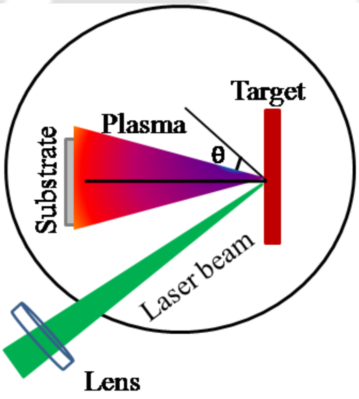

Figure 1.3 *Schematic of pulsed laser ablation setup.*

process. The plasma temperature and density in the neighbourhood of the target are very large but decreases very rapidly on moving away from the target due to very high plasma expansion velocities ~ 10^6 m/s **[168-169]** because of pressure gradient**.** In case of gaseous ambient, the gas molecules also undergoes ionization/plasma formation via multiphoton absorption of laser energy. The target plasma and background gas plasma undergoes adiabatic cooling and under suitable dynamics form the molecular species. These molecular species condenses and nucleate onto the substrate surface and growth of thin film begins. The quality of deposited thin film is governed by the kinetic energies of species impinging on the substrate. High kinetic energy allows epitaxial growth even at low substrate temperature due to creation of additional crystallization centres. Moreover, other deposition parameters like laser fluence, background gas pressure, substrate temperature, target-substrate distance, deposition time, etc. can be tuned to obtain desired quality thin film. These deposition parameters govern the physical and chemical properties of laser produced plasma (LPP). These plasma parameters in turn affect the quality of the deposited thin film. Thus, to understand the correlation between the plasma properties of LPP and its effect on PLD thin films, it is important to study LPP. This study will help in obtaining optimum deposition parameters for the growth of highly crystalline thin film.

The laser produced plasma is normally studied by laser induced breakdown spectroscopy (LIBS) and Langmuir probe technique **[177-192]**. LIBS is a line integrated technique and provides information about dynamics of various atomic and molecular species [**178**]. Langmuir probe technique enables local measurement of plasma temperature, average ion density, plume shape, plasma flow velocity and plasma potential **[181, 185-192]**.

1.4 Organization of present thesis

The present thesis aims towards study of group delay and temperature sensing properties of thin film of ruby and barium titanate (BTO). The pulsed laser deposition technique is used to fabricate thin films of ruby and BTO. Laser fluence, background gas pressure, deposition time, substrate annealing, post annealing of films, etc. during PLD growth has been varied to optimize the film quality. The laser produced plasma under various deposition conditions was studied using planar Langmuir probe, to understand and optimize the growth parameters. The deposited PLD films were subjected to structural, optical and morphological studies. The nonlinear coefficients of the deposited films were measured by Z-scan technique. The slowing down action of light was studied in the optimized thin film of ruby and barium titanate. In addition, thin film of ruby and barium titanate have been demonstrated to act as photonic temperature sensor.

The present thesis is organized in 9 chapters as summarized below.

Chapter 1, "Introduction", presents relevant literature survey on the subject with a brief discussion on slowing down of light, PLD of thin film and photonic temperature sensor.

Chapter 2, "Experimental Details", describes various experimental setups developed to grow thin films of ruby and barium titanate, Langmuir probe for measurement of electron temperature and ion density. The Z-scan setup assembled to measure the nonlinear absorption coefficient and nonlinear refractive index of ruby and BTO thin film. The degenerate two-wave mixing setup for the group delay study is also detailed in this chapter. *Chapter 3, "Laser induced plasma of ruby",* discusses the measurement of various plasma parameters using planar Langmuir probe. *Chapter 4, "Pulsed laser deposition and characterization of ruby thin film",* describes the effect of various deposition parameters on structural and optical properties of ruby thin film. *Chapter 5, "Pulsed laser deposition and characterization of Barium titanate thin films",* describes effect of deposition time & annealing on tetragonality of PLD deposited BTO thin films. *Chapter 6, "Optical delay of light in photorefractive Barium titanate crystal and PLD thin film",* discusses the group delay via degenerate two-beam propagation of laser beam in crystal and thin film of barium titanate. *Chapter 7, "Optical delay of light in epitaxial ruby thin film",* presents the results on pulse propagation in ruby thin film via degenerate two-wave mixing. *Chapter 8, "Ruby and Barium titanate thin films as a photonic temperature sensor",* describes the application of ruby and BTO thin film as a photonic temperature sensor. The last chapter of thesis *Chapter 9, "Conclusion",* sums up the salient features of the present research work along with the possibilities of future explorations.

Chapter 2

Experimental Details

Pulsed laser deposition (PLD) technique is highly successful for growth of thin films of ceramic materials **[148-151]**. The quality of deposited film is governed by the dynamics of laser produced plasma (LPP). In the present thesis, the effect of laser fluence, deposition time, gas pressure, substrate temperature and substrate on to the quality of ruby thin film was studied to obtain the optimum parameters for PLD. The LPP of ruby was studied by Langmuir probe and an attempt is made to correlate it with the quality of PLD ruby thin films. For deposition of barium titanate (BTO) thin films, optimized parameters were taken from literature [**132-141**].

The PLD thin films of ruby and BTO deposited at optimum deposition parameters were subjected to Z-scan measurement to determine the nonlinear absorption coefficient and nonlinear refractive index. The sub and superluminal pulse propagation of light in both these films were studied via degenerate two-wave mixing technique. The effect of relative polarization and pump intensity on slowing down action in BTO crystal was also studied by using the chopped pulses from He:Ne laser. The experimental details of target preparation, PLD setup, plasma diagnostic setup, Z-scan technique, crystallographic axis determination of Ce:BaTiO_3 crystal, optical delay setup, low temperature PL/Raman setup and other assembled setups are presented in this chapter.

2.1 Target preparation

For the deposition of ruby thin film via PLD, ruby target was prepared by taking a mixture of high purity powder of Al_2O_3 (99.998%) (Merck) and Cr_2O_3 (Loba Chemie) in appropriate proportion. The mixed powder was annealed in the furnace for six hours at 1000˚C to make it moisture free.

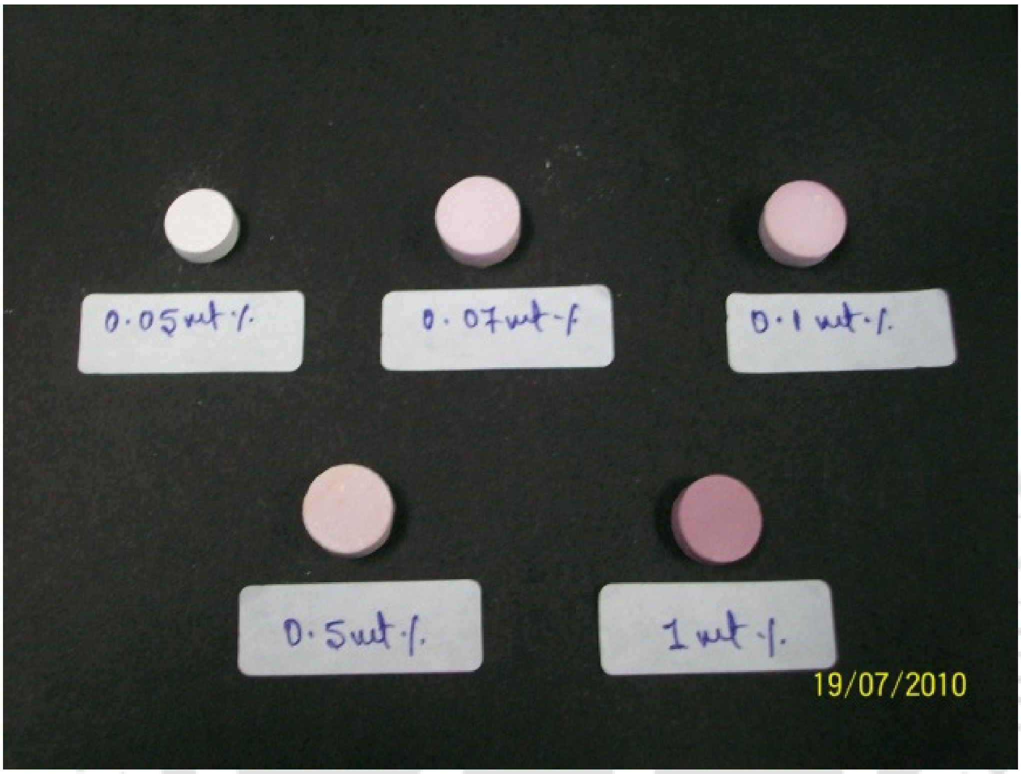

Figure 2.1 *Ruby pellets of various chromium concentrations.*

After annealing the coarse powder was grinded in the form of fine powder and pressed into round pellets of ~ 13 mm diameter. Finally, ruby targets were obtained after sintering the pellets at 1400˚C for 24 hrs and then at 1700˚C for 2 hrs. Figure 2.1 shows the ruby pellets of various chromium concentrations ranging from 0.05 wt% to 1 wt%. Sintered pellets appeared pink in color.

For the PLD of barium titanate thin film, pellets of barium titanate were prepared from barium titanate powder (99%) (Alfa Aesar). The powder was pressed into circular shape with a diameter of ~13 mm using a pellet maker, and sintered at 1400˚C for 2 hrs.

2.2 Pulsed laser deposition of thin film of Ruby & Barium titanate

Figure 2.2 shows the schematic of PLD setup assembled to deposit the thin films of ruby and barium titanate. The corresponding photograph is shown in figure 2.3.

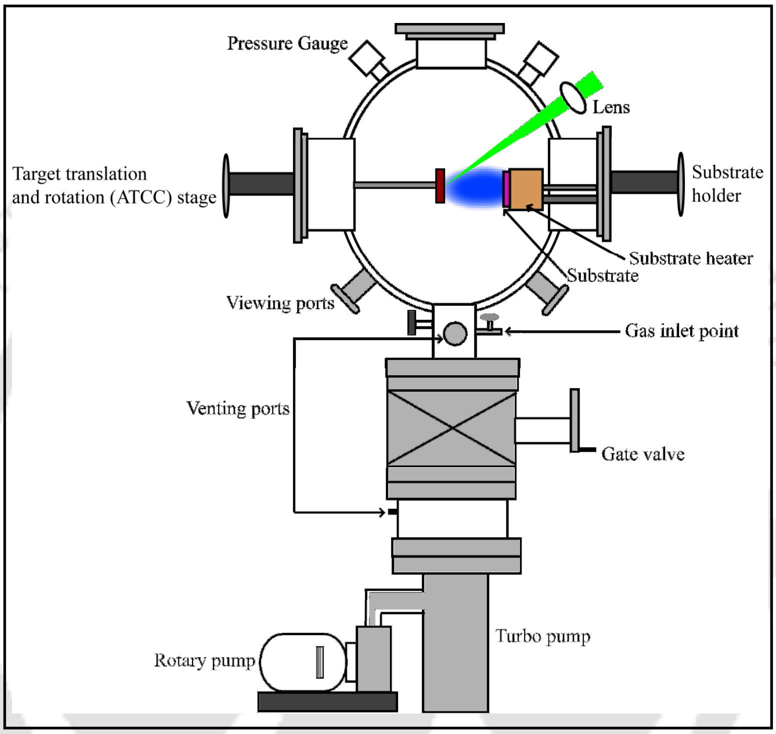

Figure 2.2 *Schematic of Pulsed Laser Deposition (PLD) setup.*

The second harmonic of Q-switched Nd:YAG laser (Quanta-Ray INDI-HG) delivering ~ 200 mJ/pulse energy in 8 ns pulse duration at 10 Hz repetition rate was focused on to the target with a plano convex lens of focal length 35 cm. The target was mounted on a motorized target carrousel, interfaced with automatic target carrousel controller (ATCC). The target carrousel was mounted on one of the 150 CF port of a multiport spherical vacuum chamber of diameter 12 inch made up of stainless steel (Figure 2.2). The bottom port (100 CF) of the chamber was connected to a turbo molecular pump (model no: Hi Pace 300 C) through a 100 CF gate valve for vacuum isolation. The turbo pump was backed by the rotary pump. The pressure inside the chamber was monitored using pirani, penning and capacitance gauges connected at various ports of the chamber. The chamber was evacuated up to a base pressure of ~ 10^{-6} mbar before deposition and then filled with required O_2 gas in the pressure range ~ 10^{-2} to ~ 10 mbar. The gas line from oxygen cylinder was connected to the chamber via gas flow controller to a 16 CF port as shown in the figure 2.3. The gas flow rate was maintained between 20 Standard cubic centimeters per minute (SCCM) to 40 SCCM. The high power laser was focused on to the ruby and barium titanate targets at an angle of 45° as shown in figure 2.2, in the oxygen ambient. The breakdown of target material in the focal region and the breakdown of gas in its neighborhood take place resulting into plasma formation. This plasma, consisting of neutrals, ions and clusters of the target material as well as that of

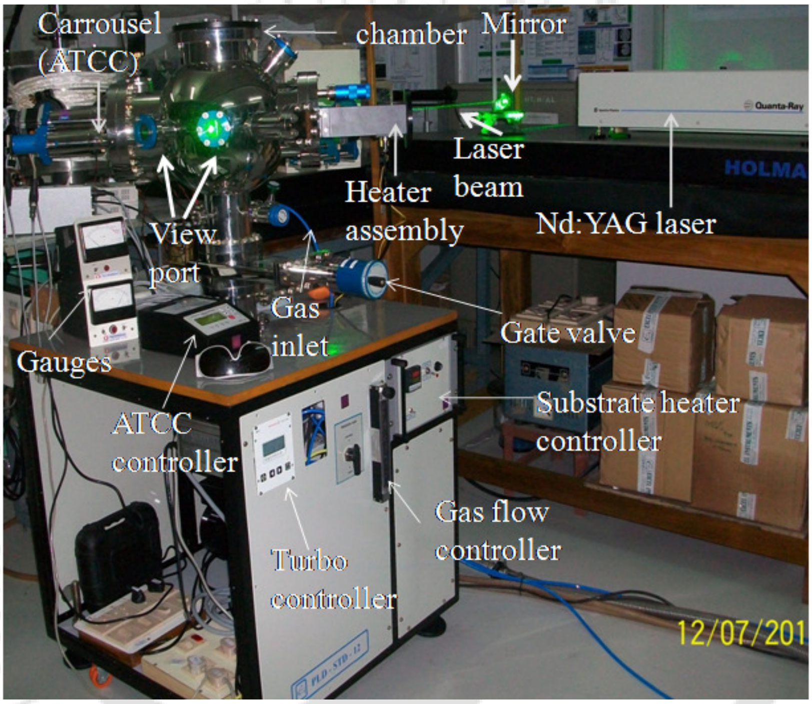

Figure 2.3 *Photograph of PLD setup.*

background gas, expands and undergoes the molecular formation under the suitable dynamics and is finally deposited on to cleaned quartz and sapphire substrate placed parallel to and at a distance of 4 cm away from the target. The substrate was mounted on a substrate holder assembly with a provision of resistive heater to control the substrate temperature from room temperature to 750°C during and after deposition in a programmable fashion. This substrate holder was mounted on another 150 CF port of the ablation chamber, facing the target assembly. PLD thin films of ruby were deposited over a large range of deposition parameters to obtain the optimum condition for the epitaxial growth of the film as described in chapter 4.

BTO thin film was deposited at a laser fluence of ~ 10 J/cm^2, substrate to target distance was 4 cm and oxygen pressure at ~ 0.1 mbar and substrate temperature ~ 750°C. These parameters were obtained from literature **[132-141]**. In order to study the effect of deposition time on thickness of PLD deposited BTO thin film, the film was fabricated for deposition time of 30 min, 1 hr, 2 hrs, 3 hrs, 4 hrs and 6 hrs.

2.3 Laser induced plasma studies

The quality of thin films fabricated via PLD depends upon the dynamics of laser produced plasma (LPP). To study the LPP dynamics and to find its correlation with the quality of deposited thin film via PLD, it is important to analyze the spatial and temporal evolution of electrons and ions. For this purpose, a flat plate Langmuir probe setup was assembled as shown in figure 2.4. The corresponding photograph of inside view of chamber is shown in figure 2.5 (a) and the probe mounted on Wilson feed through is shown in figure 2.5 (b). The electron and ion time of flight (TOF) signals were obtained by displaying the voltage drop across a 10 Ω ceramic resistor, connected towards the grounding end as shown in figure 2.4, using a digital storage oscilloscope (DSO, Tektronix, DPO-3034) interfaced with a computer. The DSO was triggered w.r.t. the Nd:YAG laser pulse for recording the signals from the plasma. For acquiring the trigger signal, a glass plate with 10% reflectivity was placed in the path of Nd:YAG laser beam as shown in figure 2.4.

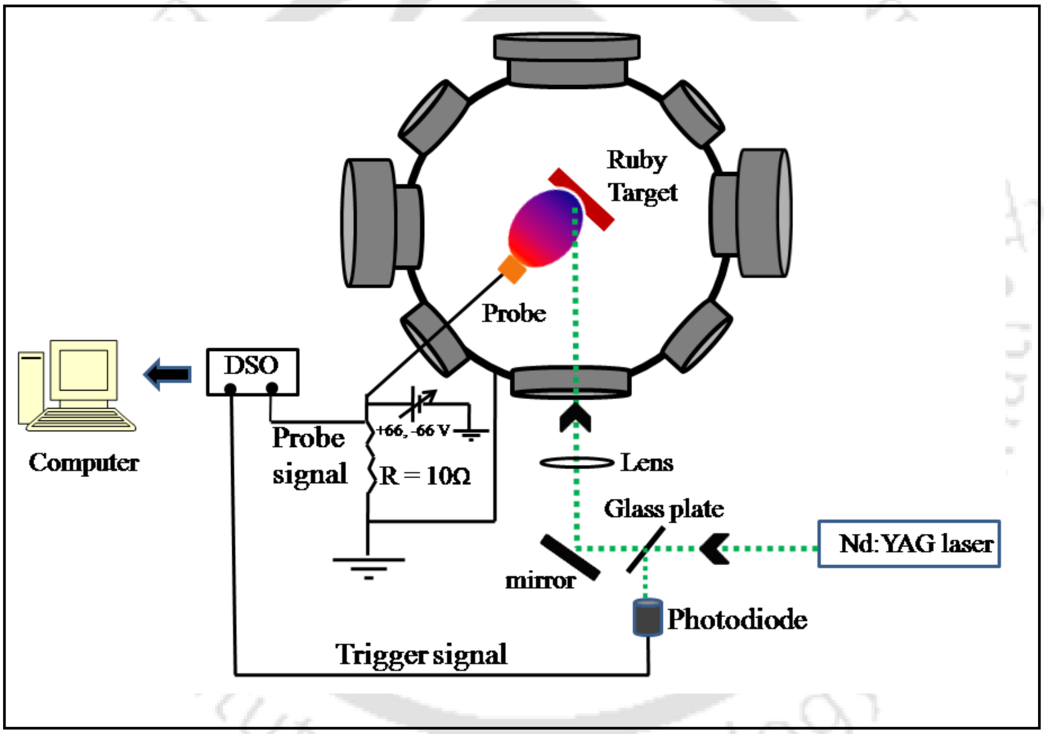

Figure 2.4 *Schematic of Langmuir probe setup.*

The reflected beam from the glass plate was detected by a fast photodiode. The signal from photodiode was displayed onto one of the channel of DSO by using a 50 Ω terminator. The vacuum chamber was grounded properly to complete the electrical circuit. To record the spatial evolution of plasma, the probe was scanned from 10 mm to 80 mm from the target.

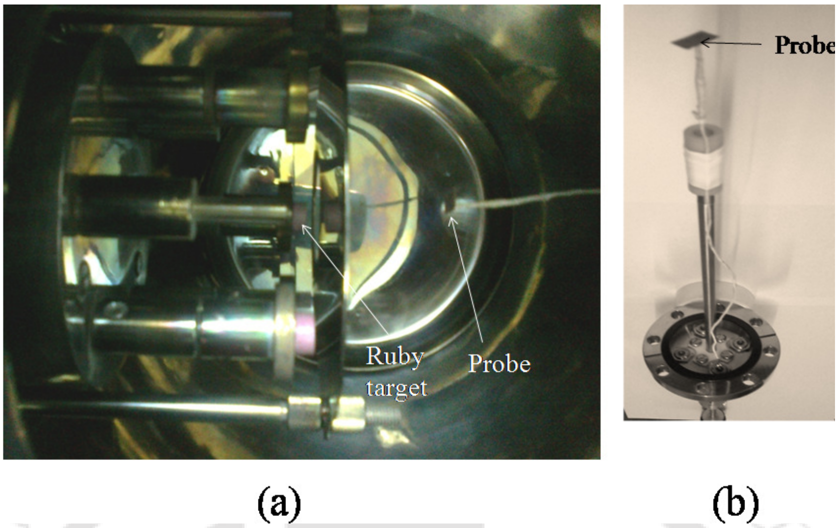

Figure 2.5 *Photograph of (a) inside view of chamber and (b) Langmuir probe mounted on a wilson feed through.*

The DSO traces of electron and ion time of flight (TOF) signals at bias voltages of + 66 V & -66 V respectively are shown in figure 2.6 (a) & (b). Both electron and ion current shows the twin peak structure **[191-192]** labeled as 'slow' and 'fast' peaks.

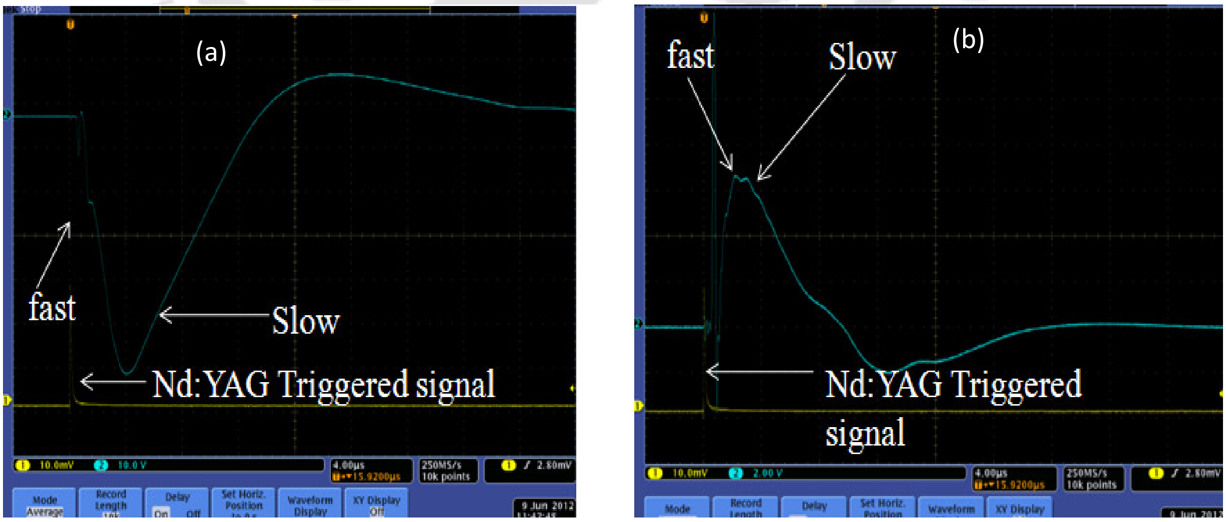

Figure 2.6 *DSO traces of TOF signal (a) electron & (b) ion.*

The electron and ion current from the probe were recorded by varying the bias voltage from -66 V to +66 V. The electron temperature can be estimated from the slope of semi-logarithmic plot of ln(I) vs V [**186-189**] given by equation 2.1.

$$\frac{d\ln(I)}{dV} = \frac{1}{T_e} \tag{2.1}$$

Where, I is the probe current and V is the bias voltage. The ion density, n, can be calculated by using equation 2.2;

$$I_i = Aenv_i \tag{2.2}$$

where, I_i is the saturation current for ion obtained from I-V characteristics of Langmuir probe, A is the area of probe and v_i is the velocity of ion obtained from the TOF measurement.

$$v_i = d/t \tag{2.3}$$

Where, d is the distance of the probe from the target and t is the delay in the peak position of the probe current at saturation w.r.t. the Nd:YAG triggered signal as shown in figure 2.6 .

2.4 Characterization of PLD deposited thin films

The crystal structure of PLD thin films of ruby and barium titanate was studied via XRD [Seifert 3003 T/T] pattern. XRD measurements were performed at the grazing incidence angle of 5° using 0.154 nm wavelength of Cu K_α radiation. The thickness of the deposited films was measured by Veeco Dektak 150 profilometer. AFM images [NT-MDT Smena -B] were recorded for measurement of rms surface roughness and average grain size. Height histograms of the scanned AFM images were used to estimate average grain sizes using "Grain Analysis" program (provided by NT-MDT Co., Russia). The emission and excitation spectra of the PLD thin films were recorded by using Edinburg, FS-920 P fluorimeter by exciting with 532 nm light from a Xenon lamp. The fluorescence lifetime measurement was performed by using a microsecond flash lamp of fluorimeter. Raman spectra of films were recorded by using Horiba Jobin Yvon, LabRam HR800 micro Raman spectrometer using 488 nm of argon ion laser. The temperature dependent Raman of BTO PLD thin film was performed by placing the sample on Linkam stage coupled with the LabRam HR800 micro Raman spectrometer. Using the same setup, temperature dependent photoluminescence (PL) of PLD ruby thin film was recorded. The ruby film was excited using 632.8 nm He:Ne laser to explore its applications as a photonic temperature sensor. The linear absorption coefficient of ruby and BTO film was estimated from the UV-Visible spectra by using envelope approximation [**193**].

2.5 Z-scan setup for the measurement of NLO parameters of Ruby and Barium titanate thin films

Z-scan is a simple technique to measure non linear absorption coefficient (β) and nonlinear refractive index (n_2) of bulk/thin film [**194-195**]. The experimental setup assembled to record open Z-scan of PLD deposited thin films of ruby is shown in figure 2.7. Second harmonic of Nd:YAG laser (model no: INDI-HG) was steered with the 90° prism towards the glass plate GS1. The reflected light from the glass plate was allowed to fall on the beam splitter BS. The direct transmitted beam from BS was focused on to the PLD thin film sample, mounted on a motorized translation stage for Z-scanning, with a 25 cm focal length lens (L1). The open aperture signal beam from the sample was focused by 5 cm focal length lens (L2) on the photodiode PD1 (model no: 13DSI007 melles griot). The reflected light from BS was steered with glass plate GS2 and detected with a photodiode PD2 for reference signal. Neutral density filter (NDF) (O.D = 4) was placed in front of both the PD1 & PD2 to avoid the saturation of photodiodes. The glass plates GS1 & GS2 were used to reduce the laser intensity in order to avoid damage of ruby film as well as that of photodiodes at higher laser intensities. The signals from PD1 and PD2 were fed on to the DSO interfaced with the computer. Both these signals were averaged over 64 pulses. The thin film was scanned on either side of the focal spot to a distance of 30 mm. By fitting the open aperture Z-scan signal using equation 2.4 below, non-linear absorption coefficient (β) for PLD ruby thin film was estimated.

$$T_{open} = 1 - \frac{\beta I_0 L_{eff}}{(2)^{3/2}[1+(z/z_0)^2]} \tag{2.4}$$

Where, T_{open} is the signal obtained after normalizing the ratio of transmitted signal from PD1 & PD2 w.r.t. the maximum ratio. z is the position of sample w.r.t. the focal spot, z_o is Rayleigh length, β is the two photon absorption (TPA) coefficient, L_{eff} is the effective sample length and I_0 is the peak irradiance at the centre of the focal spot.

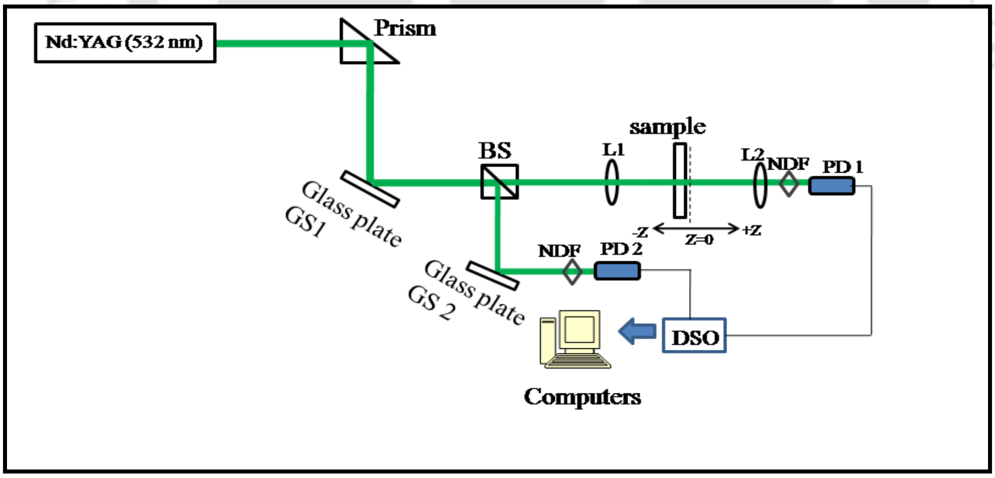

Figure 2.7 *Schematic of open aperture Z-scan setup using Nd:YAG laser.*

The effective sample length L_{eff} can be estimated using,

$$L_{eff} = \frac{1-\exp(-\alpha L)}{\alpha} \tag{2.5}$$

where, α is the linear absorption coefficient of the sample. L is the actual film thickness measured using profilometer. The Rayleigh length z_0 is given by,

$$z_0 = \frac{\pi w_0^2}{\lambda} \tag{2.6}$$

Where, w_o is the beam diameter at the focus (z=0) which was calculated using the relation,

$$w_0 = \frac{f\lambda}{D} \tag{2.7}$$

where, f is the focal length of lens L1 (25 cm), D is the laser beam diameter ≈ 10 mm, measured from the burn pattern of laser and λ is the laser wavelength (532 nm). From the equation 2.7 the estimated beam waist, w_o, was ~ 13.3 μm and Rayleigh length was ~ 1 mm in the present case. The transmittance T_{open} was measured from the ratio of PD1 and PD2 signals as a function of z and normalized w.r.t. transmittance at $z >> z_0$.

To estimate the value of non-linear refractive index n_2, a close Z-scan setup (Figure 2.8) was assembled. It is similar to open Z-scan setup except an aperture was inserted in front of lens L2. The first order solution for the normalized transmittance through the sample for close Z-scan is given by [**194**],

$$T_{closed} = 1 - \frac{4\omega\beta n_2 I_0 L_{eff}(z/z_0)}{c[(z/z_0)^2+1][(z/z_0)^2+9]} \tag{2.8}$$

where, T_{closed} is obtained by dividing the normalized closed and open aperture (T_{open}) Z-scan signals, ω is the angular frequency of laser, c is the speed of light and n_2 is the nonlinear refractive index. The transmittance T_{closed} was fitted to equation 2.8 to determine the nonlinear refractive index, n_2.

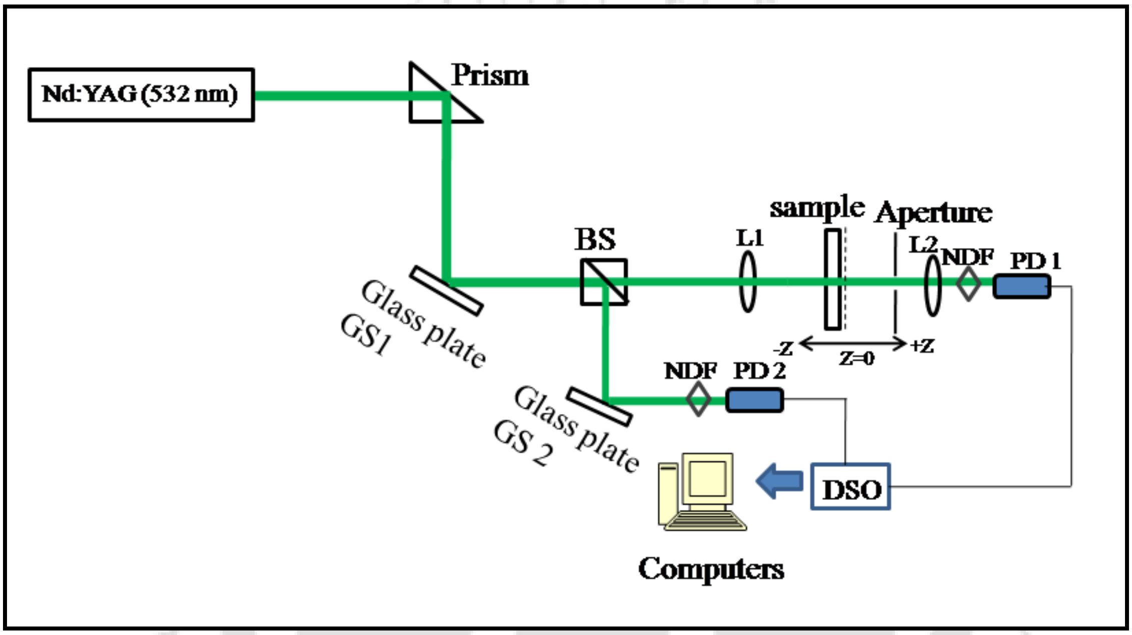

Figure 2.8 Schematic of closed aperture Z-scan setup using Nd:YAG laser.

In order to record the open and closed Z- scan spectra of barium titanate thin film the assembled set up is as shown in figure 2.9 and 2.10 respectively. In this, He:Ne laser at a wavelength of 632.8 nm with beam diameter ~ 1.23 mm (model no: 05-LHP-927, melles griot) was focused onto the PLD thin film of BTO of thickness ~ 3300 nm with a lens L1 of focal length 10 cm. The sample was placed on a motorized translational stage to move the sample 30 mm on either side of focus. The transmitted signal from the thin film sample was focused onto the photodiode using lens L2 of focal length 5 cm.

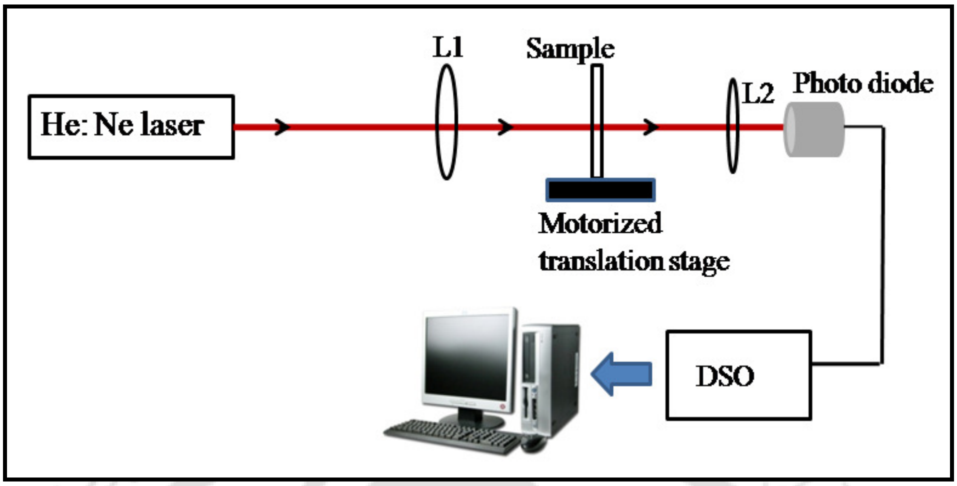

Figure 2.9 *Schematic of open aperture Z-scan setup using He:Ne laser.*

The signal from the photodiode was displayed onto the DSO interfaced with the computer. The normalized open aperture signal was fitted to equation 2.4. In this setup the beam waist, w_o, estimated from equation 2.7 was ~ 51.4 μm and Rayleigh length (equation 2.6) was ~ 13 mm and the laser power at focus was ~ 17.3×10^6 W/m^2.

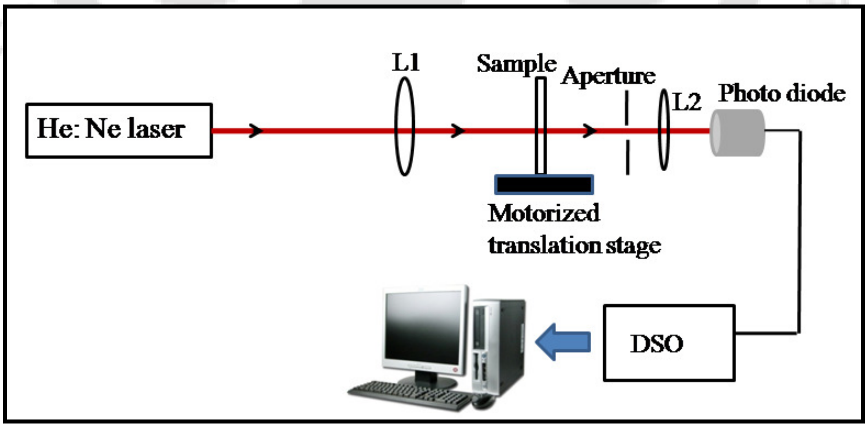

Figure 2.10 *Schematic of closed aperture Z-scan setup using He:Ne laser.*

To acquire the closed aperture Z-scan signal an aperture was placed in front of lens L2 as shown in figure 2.10.

2.6 Optical delay of light in BTO crystal & PLD deposited thin films of Barium titanate & Ruby

In order to study optical delay of light inside PLD deposited optimized thin film of BTO & ruby, degenerate two-wave mixing technique was used. To ensure the validity of this technique, initially the experiment was performed on BTO single crystal. BTO is an anisotropic crystal and therefore pulse propagation inside it will depend upon the orientation of the crystal. The crystallographic axes of BTO crystal was identified via backward two-wave mixing [**196**] as detailed in section 2.6.1.

2.6.1 Determination of crystallographic axis of BTO crystal

Barium titanate is a photorefractive uniaxial crystal in the tetragonal phase at room temperature with the crystallographic axes a=b≠c as shown in figure 2.11. The experimental setup used to identify the crystallographic axes is shown in figure 2.12. A transmitted S-polarized He:Ne laser beam at 632.8 nm through a beam splitter BS was incident normal onto the BTO crystal (5 mm × 5 mm × 7 mm). The transmitted beam from crystal back face was imaged onto the photodiode (PD1).

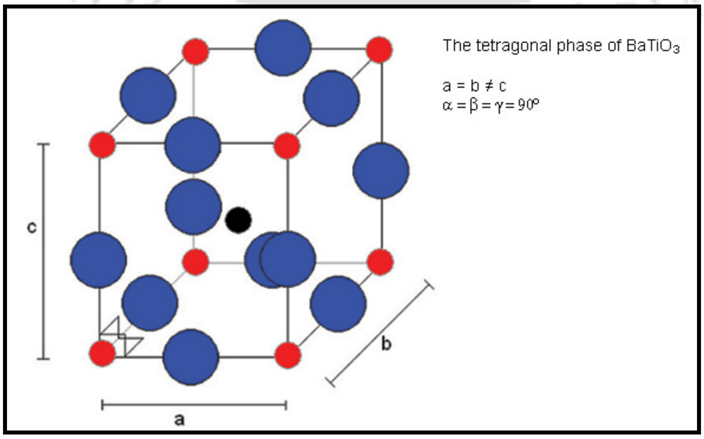

Figure 2.11 *Crystal structure of tetragonal BaTiO$_3$.*

The reflected beam from crystal's back face retraces its path along the direction of incident beam and was reflected from BS and detected by a photodiode PD2 as shown in figure 2.12. The output of both the photodiode was displayed onto a Digital storage oscilloscope (DSO), interfaced with a computer. The temporal evolution of transmitted and reflected signals from the back surface of the crystal was compared for both S and P polarization. To attain the P-polarization, a half wave plate was inserted before the BS, as shown in figure 2.12.

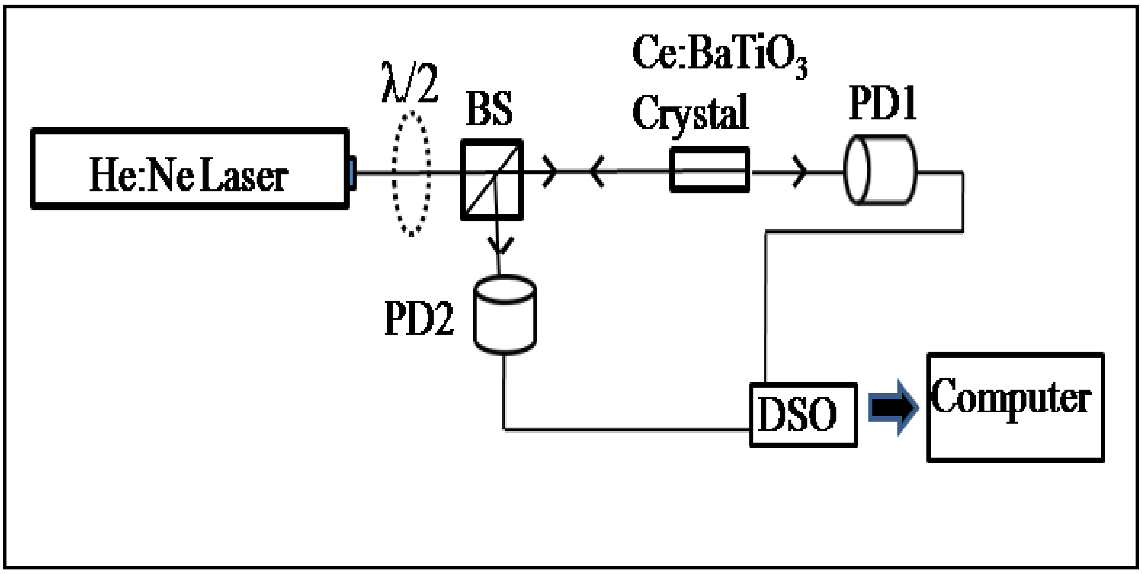

Figure 2.12 *Experimental setup for determination of crystallographic axis of BTO crystal.*

The intensity variations of the transmitted and reflected wave for S and P polarization of the incident beam as a function of time, incident normal to all the three faces of the crystal are shown in the Figure 2.13, 2.14 and 2.15. Figure 2.13 (a) and (b), for face I, shows that the intensity variation with time for both S and P-polarized beam respectively, were similar in nature.

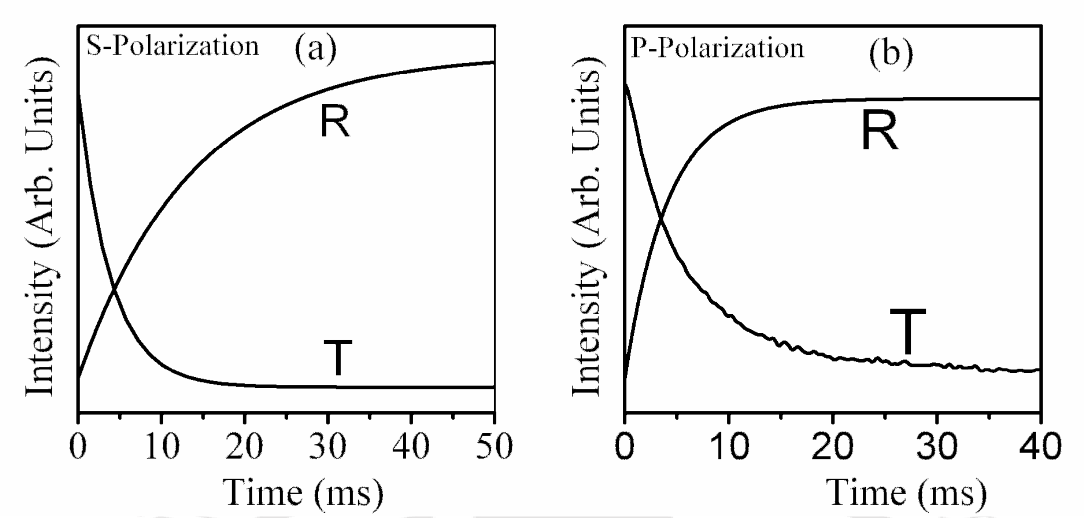

Figure 2.13 *DSO traces for transmitted (T) and reflected beam (R) for face I. For incident beam (a) S-polarized (b) P-Polarized.*

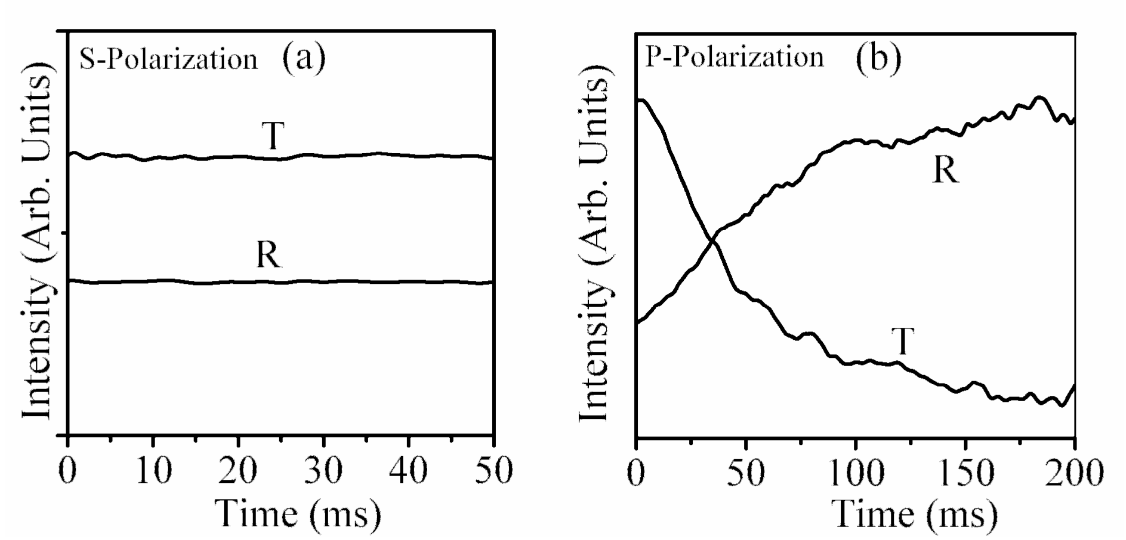

Figure 2.14 *DSO traces for transmitted (T) and reflected beam (R) for face II. For incident beam (a) S-polarized (b) P-Polarized.*

The intensity of the transmitted beam was decreasing with time, while the reflected beam was amplified for both the polarizations. It can be seen from Figure 2.14 (a) that for face

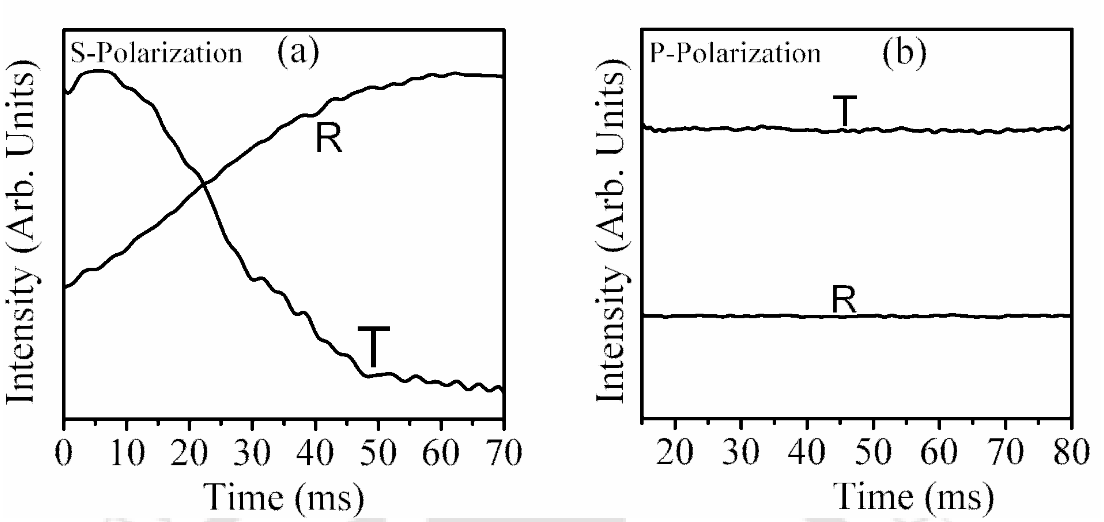

Figure 2.15 *DSO traces for transmitted (T) and reflected beam (R) for face III. For incident beam (a) S-polarized (b) P-Polarized.*

II, there was no intensity variation for both the transmitted and reflected beams in case of S-polarized beam. For P-polarized beam, as shown in Figure 2.14 (b) the intensity of the transmitted beam was decreasing with time, while the intensity of the reflected beam was increasing with time. For the third face of the crystal, face III, as shown in Figure 2.15 (a), for S-polarized beam, the intensity of the transmitted beam was decreasing with time, while the intensity of the reflected beam was increasing with time. For a P-polarized beam, as shown in Figure 2.15 (b) there was no intensity variation for both the transmitted and reflected beams.

The light incident onto the crystal, as shown in figure 2.12, interacts with the light reflected from its back surface within the crystal. These two coherent laser beams on interference inside the crystal leads to the formation of intensity grating **[197]**. The intensity grating will generate space charge electric field via either the photovoltaic process or diffusion of charge carriers. In $BaTiO_3$ crystal, diffusion is the dominant process for the transport of the charge carriers **[49]**. Such a field induces refractive index change via the pockel's effect given by equation 2.9.

$$\Delta n = -\frac{1}{2} n^3 r_{eff} E \tag{2.9}$$

where r_{eff} is the efficiency electro-optic coefficient. The refractive index grating formed now can diffract the energy from one beam to another.

For the geometry of figure 2.12 (contra-directional two-wave mixing) the efficiency electro-optic coefficient is given by **[197]**

$$r_{eff} = \hat{e}_1.[\varepsilon.(r.\hat{k}).\varepsilon].\hat{e}_2 / n^4 \tag{2.10}$$

where, $\hat{e}_1$ and $\hat{e}_2$ are unit vectors in the direction of propagation of laser beams, $\hat{k}$ is the unit vector in the direction of the grating vector, ε is the second-order dielectric tensor, and r is the third order electro-optic tensor [**197**]. The electro-optic tensor depends on the rotational symmetric properties of the material and thus is different for different point group symmetries of crystals. The $BaTiO_3$ crystal is of tetragonal symmetry and belongs to the 4 mm point group symmetry. Its electro-optic tensor is given by equation 2.11 **[197]**.

$$r = \begin{bmatrix} 0 & 0 & r_{13} \\ 0 & 0 & r_{13} \\ 0 & 0 & r_{33} \\ 0 & r_{42} & 0 \\ r_{42} & 0 & 0 \\ 0 & 0 & 0 \end{bmatrix} \tag{2.11}$$

The values of the electro-optic coefficients for $BaTiO_3$ crystal are r_{13}=19.5 m/V, r_{33}=97 m/V and r_{42}=1640 m/V **[197]**.

For light incident along the C-axis of crystal, $r_{eff} = r_{13}$, for both S-polarized and P-polarized light. From equation 2.9, $\Delta n > 0$ [**196**]. Hence in this case, for both the polarization the reflected beam will be amplified via backward two-wave mixing and there wouldn't be any effect of polarization of light. Thus, it can be concluded that figure 2.13 corresponds to the propagation of laser beam along the C-axis.

For light incident along the Y-axis of crystal, for S-polarized light $r_{eff} = 0$, so $\Delta n = 0$ and $r_{eff} = r_{42}$ for P-polarized light. Hence, in case of S-polarization no energy transfer between the two beams will take place while in case of P-polarization, the intensity of the reflected beam will be amplified and that of the transmitted beam will fall down with time. Thus face II, figure 2.14, is normal to the Y-axis.

For light incident along the X-axis of crystal, from equation 3, $r_{eff} = r_{42}$ for S-polarized light and $r_{eff} = 0$, so $\Delta n = 0$ for P- polarized light. Therefore, the S-polarized beam will show the effect of backward two-wave mixing. The P-polarized beam will remain unaffected. Thus, it can be concluded that the figure 2.15, and hence face III is normal to X axis.

2.6.2 Experimental set-up for slowing down of light in BTO crystal & PLD Barium titanate & Ruby thin film

2.6.2.1 Slowing down of light in BTO crystal using chopped pulses from He:Ne laser

A degenerate two-wave mixing configuration is used to study the pulse propagation inside the $Ce:BaTiO_3$ (5 mm × 5 mm × 7 mm) PR crystal in the present work. The schematic of experimental set-up is shown in the figure 2.16 and the corresponding photograph in figure 2.17. The two coherent degenerate waves were derived from a single S-polarized He-Ne laser (model number: 05 LHP 927, Melles Griot). The laser beam coming out from the He:Ne laser was steered with mirror M1 and then splitted into two coherent beams by 50/50 non-polarizing cube beam splitter BS1. The direct transmitted beam from BS1 falling on the crystal acted as a pump beam. The other beam reflected from BS1 steered with the help of mirror M2 was chopped to generate square pulses. The pulse width T of square pulses was controlled by the chopper controller unit (model SR 540). The duration of the chopped pulse was varied from 2 ms to 20 ms by changing the frequency of chopper. This chopped beam was further sub divided into two beams with the help of another 50/50 cube beam splitter BS2.

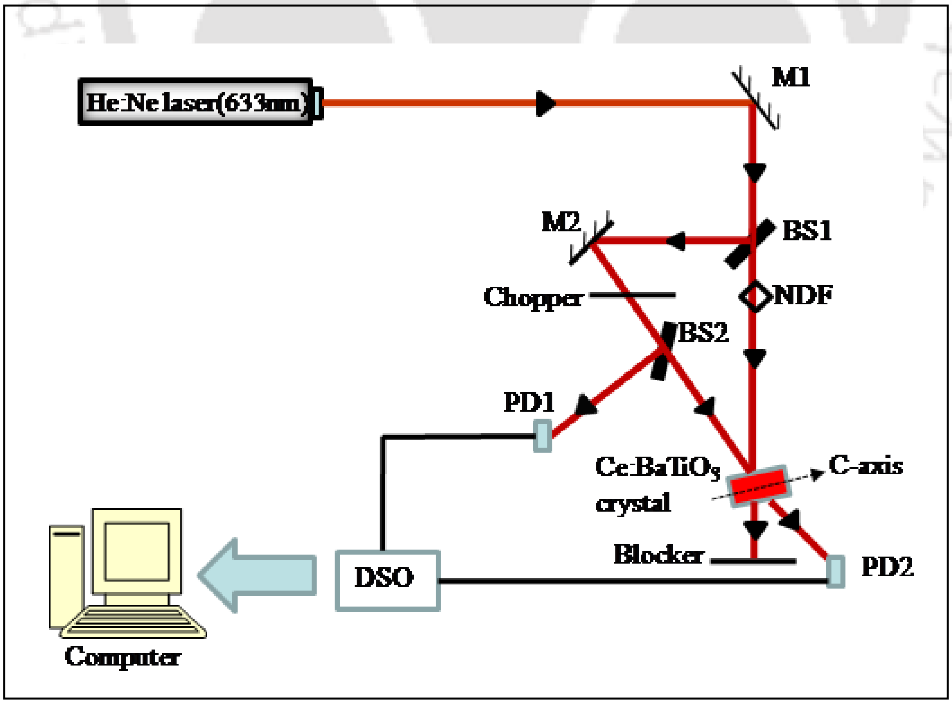

Figure 2.16 *Schematic of experimental setup for studying effect of pump intensity on slowing down of light.*

The reflected beam from BS2 served as a reference and was detected by the photodiode PD1 and fed onto one of the channel of Digital storage oscilloscope (DSO) (model no: TDS 2012, 100 MHz). Other beam was used as signal beam. The pump and signal beam were incident onto the PR crystal at a beam crossing angle of 31°. The transmitted signal beam was detected by another photodiode PD2, and was displayed onto the other channel of DSO. Time delay Δt experienced by the transmitted signal pulse from PD2 was measured w.r.t. the reference pulse. PD1 & PD2 were identical photodiode (model no:13DSI007, melles griot). The group velocity of the signal beam is measured by $v_g = L/\Delta t$, where L is the propagation distance of the signal beam inside the crystal. The incident signal beam intensity was kept fixed at ~ 0.45 W/cm^2 throughout the experiment. The pump intensity was varied by placing neutral density filter (NDF) in the path of the transmitted beam from BS1 as shown in figure 2.16. The incident pump beam was measured by a power meter (model no: 13PEM001, melles griot) after the NDF.

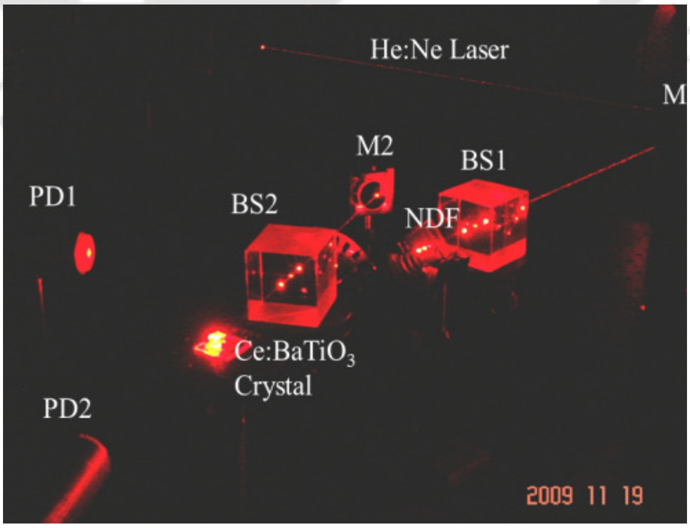

Figure 2.17 *Photograph of experimental setup for studying effect of pump intensity on slowing down of light.*

The building up and decay time of PR grating was also recorded as a function of pump intensity to understand the self-diffraction phenomenon from the photo grating.

To study the effect of polarization and crystal orientation on the pulse propagation inside the Ce:BaTiO$_3$ crystal, the setup shown in figure 2.16 is modified by placing a λ/4 plate after mirror M1 and λ/2 plate alternately before pump and probe beam, as shown in figure 2.18. Also the non-polarizing cube beam splitter BS1 was replaced by polarizing cube beam splitter. The λ/4 plate was used to convert the linearly polarized laser beam into circularly polarized beam. This circularly polarized light was split into two beams by a polarizing cube beam splitter (BS1), figure 2.18. The direct transmitted beam was P-polarized whereas, the reflected beam was S-polarized. The polarization state of the pump and probe beam were changed with the help of λ/2 plate. The experiment was conducted for all four combinations; S-S, S-P, P-S, and P-P of pump–signal polarization respectively.

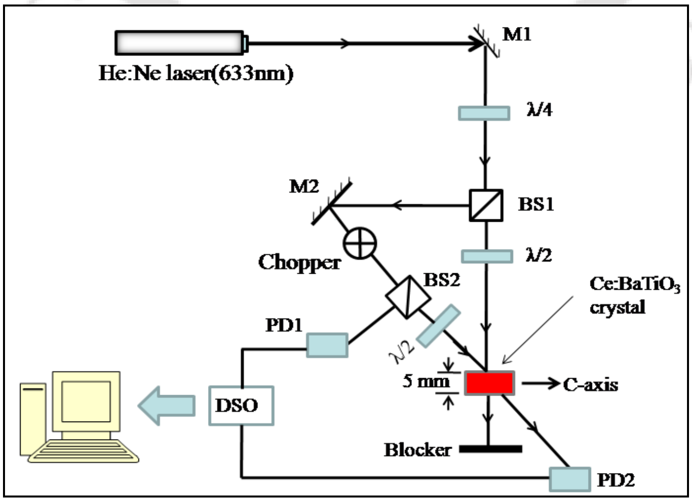

Figure 2.18 *Schematic to study effect of pump-signal polarization and crystal orientation.*

The crystal was mounted on a rotational stage. Initially, the crystal was aligned with C-axis normal to the pump beam as shown in Figure 2.18. To study the effect of incident angle on the pulse propagation, the crystal was rotated using a rotational stage in a step of 2° from its initial position. The signals were detected in the manner explained earlier.

2.6.2.2 The experimental setup for slowing down of light in Ruby & Barium titanate thin film

In case of PLD deposited thin film of ruby and BTO, the film thickness was of the order of microns, so the delay will be of the order less than μs. Therefore, the millisecond pulses of He:Ne laser will not be suitable for observing optical delay in PLD thin films. Hence, nanosecond pulses derived from Nd:YAG laser was used for studying pulse propagation inside thin film geometry. The setup of figure 2.16 was modified accordingly and shown in figure 2.19. High damage threshold optics were used for this

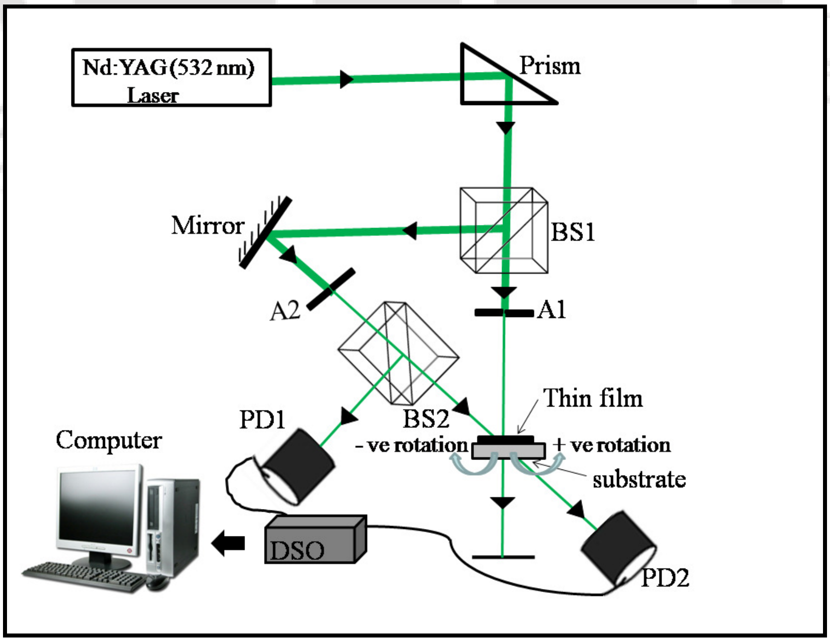

Figure 2.19 *Schematic of experimental setup for studying slowing down of light via degenerate two-wave mixing.*

setup in order to withstand the high power of Nd:YAG laser. The two coherent degenerate waves were derived from 2nd harmonic of S-polarized Nd:YAG laser (Quanta system model no. INDI-HG). The laser was used in the broad pulse mode having FWHM of ~ 200 ns. Two apertures A1 & A2 of diameter 1 mm, were placed after BS1 and BS2 as shown in figure 2.19, to reduce the size of laser beam. The identical photodiodes PD1 & PD2 of the setup 2.16 were replaced by fast photodiodes (model no: 13DSI001, melles griot) with response time of 0.35 ns. The cable lengths from both the photodiodes were kept equal and the optical path lengths travelled by the pump and signal beam before entering the thin film were also maintained same. The signal was detected by 1 GHz DSO (model no: Tektronix DPO 4104B). The pump and signal beams were made to incident onto the PLD BTO & ruby thin films at a beam crossing angle of 31°. Time delay, Δt experienced by the transmitted signal pulse from PD2 was measured w.r.t. the reference pulse. Initially, the film was placed normal to the pump beam. This was defined as the initial zero degree position of the film. The film was mounted on a rotational stage and rotated in a step of 5° from its initial position in both the directions, to study the effect of angle of incidence on the propagation of light. The laser energy was measured using energy meter (coherent field $\mathrm{Max}_{\mathrm{II}}$). The corresponding average pump intensity was ~ 63.69 $\mathrm{W/cm^2}$ and the probe intensity was ~ 25.40 $\mathrm{W/cm^2}$.

2.7 Temperature dependent studies of PLD Ruby & Barium titanate thin film

The R_1 and R_2 line of ruby crystal shows the temperature dependence [**11**]. The Raman bands of BTO crystal also show dependence on temperature [**53-55**]. But in order to make a photonic based temperature sensor, the thin film of these materials is required to be tested for temperature dependent properties. The thin film of ruby deposited via PLD on sapphire substrate for 3 hrs (sample 11, table 4.I, chapter 4) was chosen for temperature dependent studies. The temperature dependent PL spectra of ruby thin film was recorded by mounting the sample on low temperature Linkam stage, THMS 600 coupled with LabRam (resolution ~ 0.2 cm^{-1}) as shown in figure 2.20, the film was excited with 632.8 nm source. The temperature of sample was varied from 138 K to 468 K. The PL signals were recorded in a temperature step of 5 K.

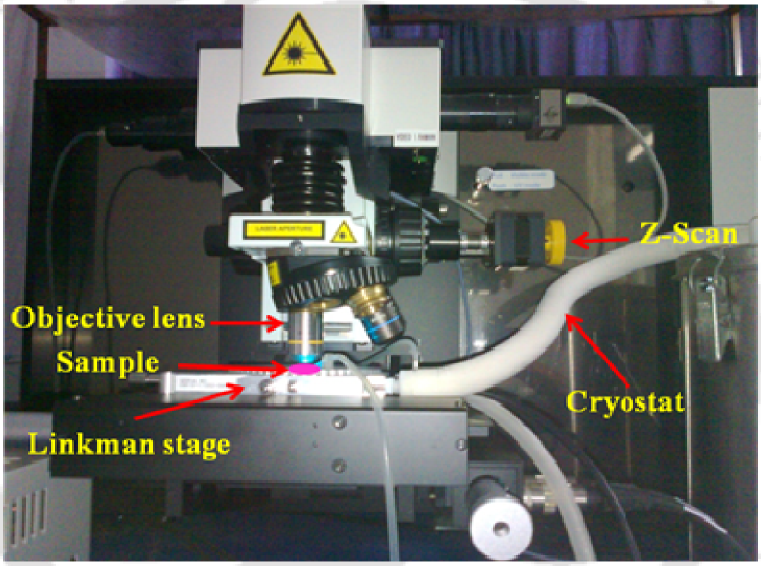

Figure 2.20 *Photograph of low temperature assembly coupled with LabRam setup.*

The variation of positions of R_1 and R_2 line and FWHM is analyzed as a function of temperature to test the suitability of ruby thin film as photonic sensor. In case of BTO thin film, the sample of maximum thickness, BTO 6 (chapter 5, table 5.I, sample BTO 6) having thickness ~ 3300 nm was subjected to temperature dependent Raman studies. The temperature dependent Raman spectra were recorded by using the same setup shown in figure 2.20. The temperature was varied from 146 K to 523 K. The 308 cm^{-1} Raman band was found to be temperature dependent. The FWHM of 308 cm^{-1} was analyzed as a function of temperature. The details are discussed in chapter 8.

Conclusion

This chapter describes the various experimental setups developed to fabricate and characterize the ruby and BTO thin film. Further, the optical delay of light in optimized PLD ruby & BTO thin film and BTO crystal via degenerate two-wave mixing is described. Finally, the reading of temperature dependent R_1 and R_2 lines of ruby and Raman spectra of BTO thin film is detailed to explore the suitability of these thin films for photonic temperature sensors.

Chapter 3

Laser induced plasma of Ruby

The optical and structural properties of PLD thin films are governed by the laser produced plasma (LPP) parameters; electron/ion velocity, electron temperature, ion density, etc. The dynamics of LPP can be studied by using optical emission spectroscopy (OES) and Langmuir probe technique [**177-192, 198**]. The values of plasma parameters obtained by OES are line integrated, whereas, Langmuir probe technique provides local measurement. In the present chapter, the measurement on electron/ion velocities, ion density and electron temperature of laser produced ruby plasma by Langmuir probe technique is reported [**181, 185-192**]. The effect of background gas pressure, laser fluence and target to substrate distance on the various plasma parameters is presented in this chapter.

The schematic of experimental setup is shown in figure 2.4 (chapter 2). The flat plate copper Langmuir probe (4 mm × 4 mm) was placed in front of the target and scanned along the direction of plasma expansion. The I-V characteristics were recorded for biasing voltage from -66 volt to +66 volt. Plasma temperature was estimated from I-V characteristics. From the time of flight (TOF) signals, ion and electron velocity and density were measured.

3.1 The dependence of electron and ion velocities, electron temperature & ion density on the distance from the target

Initially, the effect of distance from target on plasma parameters is studied by moving the probe from 10 mm to 80 mm from the ruby target along the plasma expansion direction, inside the ablation chamber maintained at a vacuum ~ 10^{-5} mbar, figure 2.4 (chapter 2), at a laser fluence of ~ 60 J/cm^2. The typical electron and ion time of flight (TOF) signals collected by the probe, for probe biasing voltage ranging from -66 volt to +66 volt at a target-probe distance of 60 mm is shown in the figure 3.1. The peak in the broad TOF curve actually corresponds to the arrival time of optimum electrons/ions flux at the probe. Figure 3.1 shows that the electron current is larger than that of ion current.

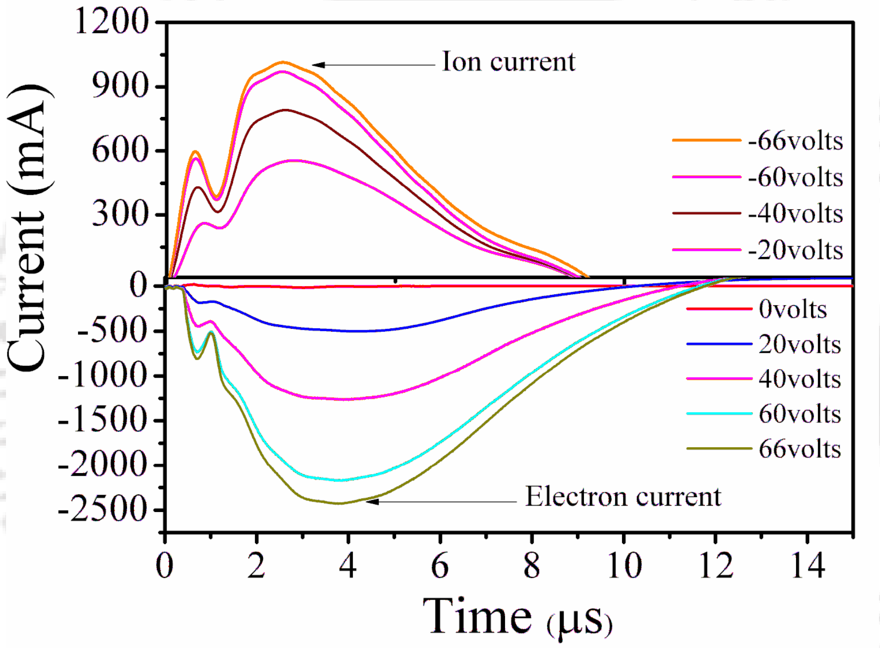

Figure 3.1 *Ion and electron current signals for various bias voltages from planar Langmuir probe placed at a distance of 60 mm from the target.*

The electron & ion current was measured as a function of bias voltage at various distances from the peak of TOF signal and then I-V characteristics was obtained. The I-V characteristics at various distances is plotted in figure 3.2. Upto 0 volt to ± 10 volt, the signals were recorded in a step of 1 volt. Beyond this, it was recorded in a step of 5 volt. At zero bias, the current is negative. This is predominantly due to the electrons in the plasma, which possess higher mobility as compared to ions. On increasing the negative bias from zero to -20 volt and beyond, the net ion current drawn from the plasma shows saturation. With increase in bias voltage from 0 volt to +66 volt, the electron current was found to increase due to collection of more and more number of negatively charged species from the plasma as shown in figure 3.2.

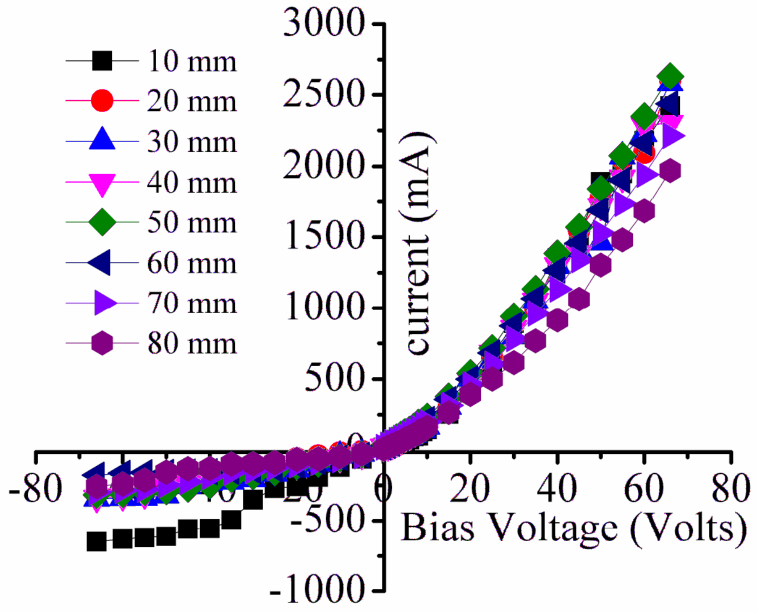

Figure 3.2 *I-V characteristic as a function of distance from the target.*

The voltage at which the probe current becomes zero is known as floating potential. For example, at a distance of 60 mm, the probe current is zero at -2 volt. Therefore, floating potential, V_p at this distance is -2 volt. At floating potential, number of ions and electrons collected from the plasma are equal, making the net current zero. With increase in distance from 10 mm to 40 mm the ion/electron signal has been found to increase. On increasing the distance beyond 40 mm, the ion as well as electron signal was reduced significantly as observed from figure 3.2. The spatial evolution of TOF electron and ion signals as shown in figure 3.3 (a) & (b), at a bias voltage of +66 volt and -66 volt respectively, at various distances. With increase in distance from 10 mm to 40 mm, two distinct peaks were observed in the TOF electron as well as in ion signal, marked by an arrow in the figure 3.3. The first peak is very sharp (duration ~ 0.5 μs). The second peak is relatively broad (duration ~ 5 μs). This confirms the plasma splitting in LPP [**192**].

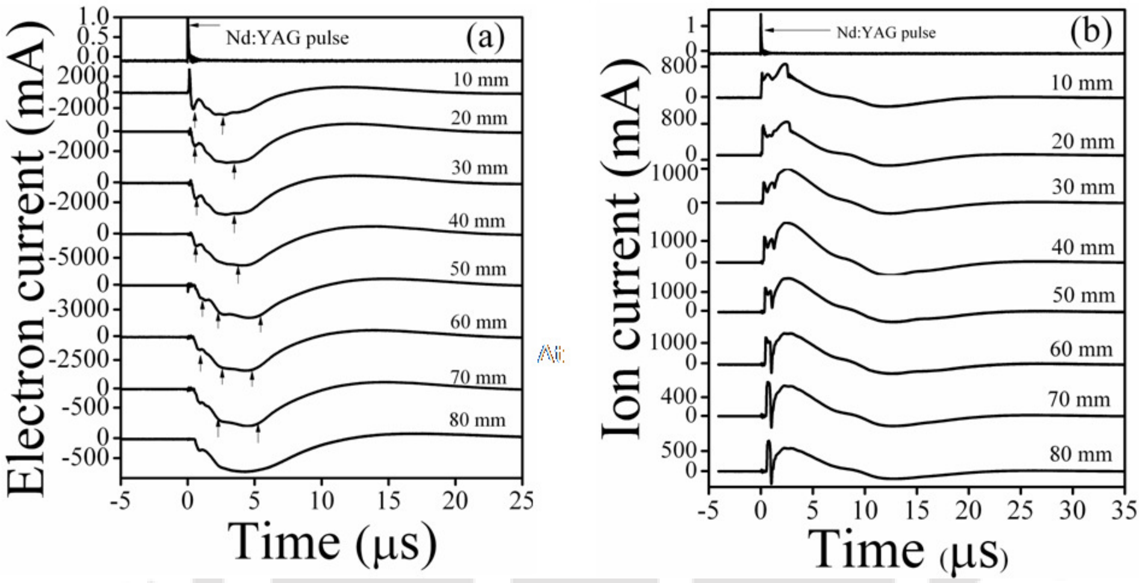

Figure 3.3 *(a) Electron & (b) ion TOF signal as a function of distance from the target.*

On increasing the distance from 40 mm to 60 mm, the second peak in electron TOF signal (slow) further splits into two parts, as indicated in figure 3.3 (a). Thus, a triple peak structure is observed at a distance of 50 mm and beyond. The ion TOF also shows twin and triple peak distribution, as shown in figure 3.3 (b). This type of structure was also supported by the observation of emission spectroscopy of laser ablated plasma [**183**]. On increasing the distance from 10 mm to 80 mm, the peak current was found to decrease for both the fast and slow components. The reduction in probe current at larger distance from the target could be due to several reasons. Firstly, due to expansion of plasma, electron and ion density falls down and hence the corresponding probe current decreases with the increase in distance from the target. The recombination and scattering of electrons and ions further reduces the number of charged species in the plasma at larger distances from the target.

From TOF signal, electron and ion velocity can be calculated using equation (2.3) (section 2.3, chapter 2). Figure 3.4 (a) shows the electron velocity for first (fast) and second (slow) peak as a function of distance from the target. The figure 3.4 (b) shows the ion velocity for the slow peak. The first peak is due to the fast component of the plasma originating from the photoelectrons and accelerated via laser absorption by inverse bremsstrahlung process [**190**]. The second peak in the electron TOF signal begins after the termination of Nd:YAG pulse. Also, the second peak is considerably delayed with the increase in distance. The slow electrons represented by the second peak in the Langmuir probe signal travels with lower velocity (~ 10^5 cm/s) compared to that of fast electrons (~10^6 cm/s), as shown in figure 3.4 (a). Due to these fast photoelectrons, a

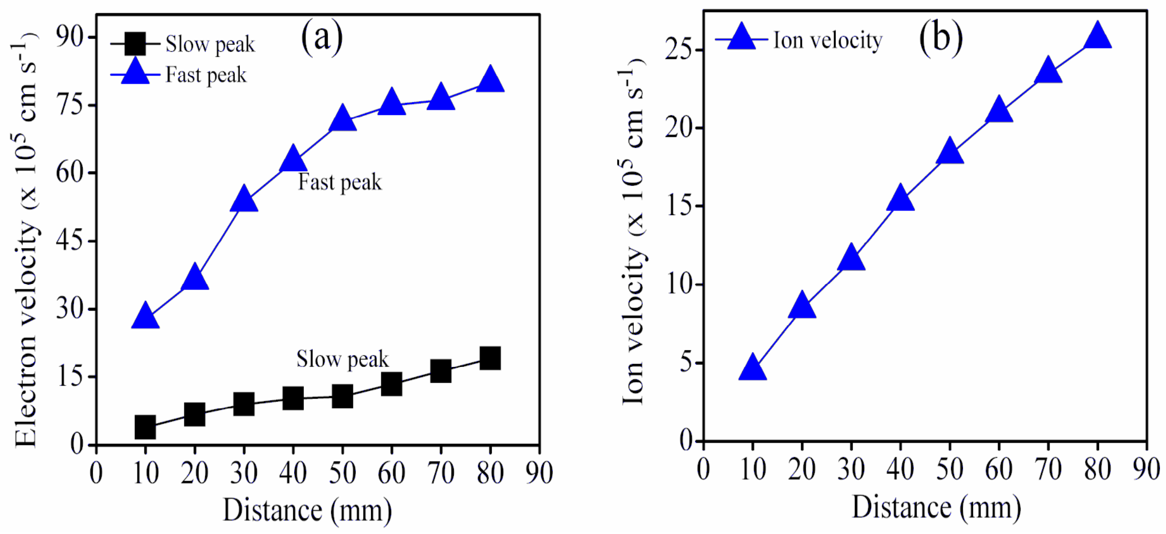

Figure 3.4 *(a) Electron and (b) Ion flow velocities as a function of distance from the target.*

double layer (DL) is formed. This DL creates ambipolar electric field. The ions entering into the field get accelerated and move faster [**191**]. The ion signal can be considered to be composed of various constituent components of ruby target. The major contribution could be from Al and O ions. The Cr ions are considered to be negligible in the ruby plasma due to low concentration. The ion density was calculated from the ion TOF signal at –66 volt (bias voltage), corresponding to the saturation regime of ion current using equation (2.2) (section 2.3, chapter 2).

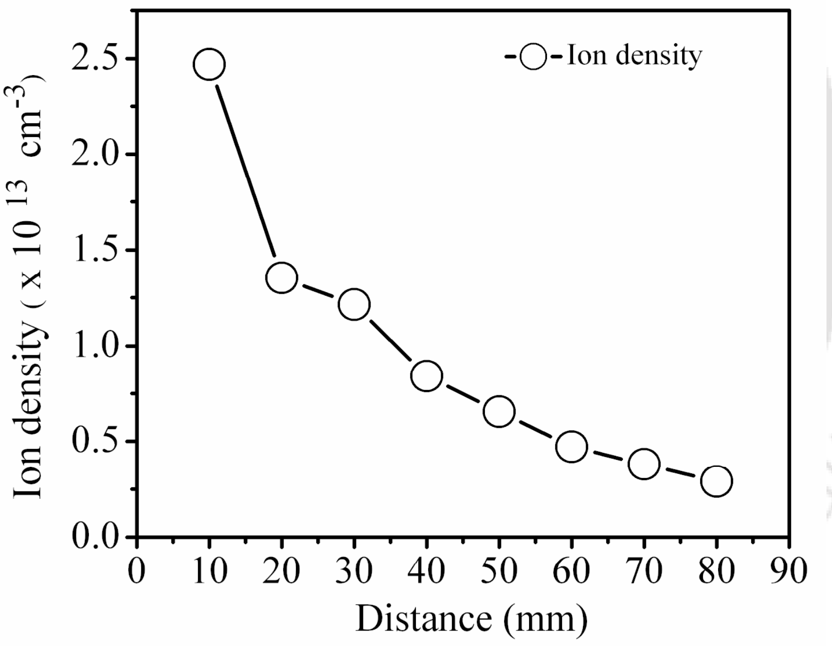

***Figure 3.5** Ion density as a function of distance from the target.*

Figure 3.5 shows the variation of ion density as a function of distance. The ion density was found to reduce from 2.4 x 10^{13} cm^{-3} to 2.9 x 10^{12} cm^{-3} on increasing the distance from 10 mm to 80 mm. The decrease in ion density is very fast upto 40 mm and then it falls down slowly. This is primarily due to the plasma expansion followed by recombination and scattering, which dominates at larger distances. Therefore, it results in the formation of neutrals and hence further reduction in the ion density. This suggests that a minimum distance of 40-50 mm from the target could be suitable to place the substrate for thin film deposition via PLD due to formation of neutral at these distances.

The spatial profile of plasma temperature is obtained from I-V characteristics of figure 3.2. Figure 3.6 shows the electron temperature as a function of distance from target. The inset of figure 3.6 (a) shows a semi-logarithmic plot of the I-V curve at a probe distance of 40 mm. The data points for bias voltage of 0 volt to 10 volt (as shown in inset), taken at a step of 1 volt is fitted linearly. From the slope of the curve ln (I) vs V,

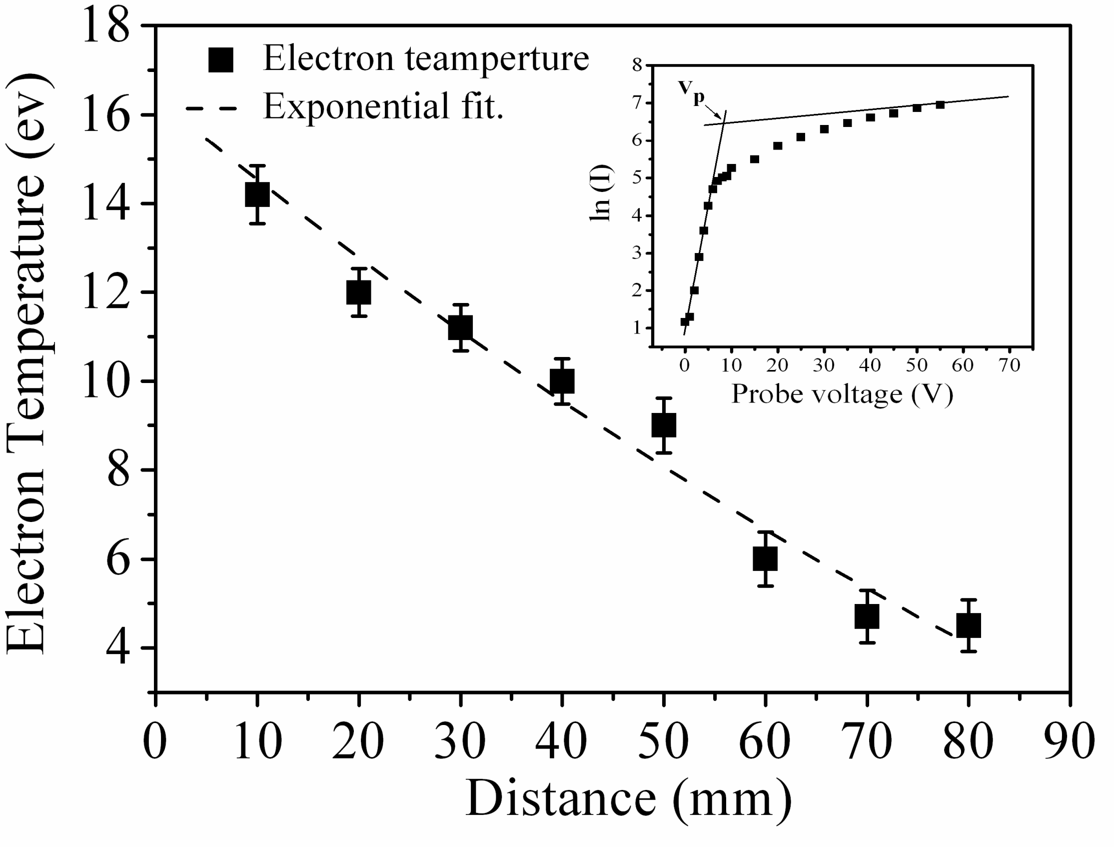

Figure 3.6 *Variation of Plasma temperature as a function of distance estimated using I-V characteristics (Inset shows ln (I) vs V at 40 mm).*

given by equation (2.1) (section 2.3, chapter 2), the electron temperature in eV can be obtained [**185-192**]. On increasing the distance from 10 mm to 80 mm, T_e was observed to decrease from 16 eV to 4.5 eV. The error bar was in the range of 0.5 eV to 0.9 eV. The spatial distribution of electron temperature was fitted to first order exponential decay curve as shown by broken line in figure 3.6. The probe to target distance of 40 mm is found to be suitable for thin film deposition due to the effective formation of large number of neutrals as is evident with the drastic decrease in ion density; figure 3.5.

3.2 Estimation of electron and ion velocities, electron temperature and ion density as a function of laser fluence

The effect of laser fluence on plasma parameters was studied by keeping the probe at a distance of 40 mm from the target along the plasma expansion and maintaining the oxygen gas pressure ~ 0.05 mbar. The laser fluence was varied from ~ 6.2 J/cm^2 to ~ 30 J/cm^2. The electron and ion TOF signals as a function of laser fluence at a bias voltage of +60 volt and -60 volt are shown in figure 3.7 (a) & (b) respectively. The multiple peak structure signal documented in the previous section under vacuum, is clearly observable. The TOF signals were found to increase on increasing the laser fluence from ~ 6.2 J/cm^2 to ~ 30 J/cm^2. The peak of the signal, corresponding to the arrival time of species, was found to decrease from 5.3 μs to 3.7 μs in case of electrons on increasing the laser fluence from ~ 6.2 J/cm^2 to ~ 30 J/cm^2. In case of ion signal the arrival time was decreased from 5.7 μs to 2.2 μs. The electron current is observed to be larger than that of ion current at every laser fluence as observed from figure 3.7. The electron and ion velo-

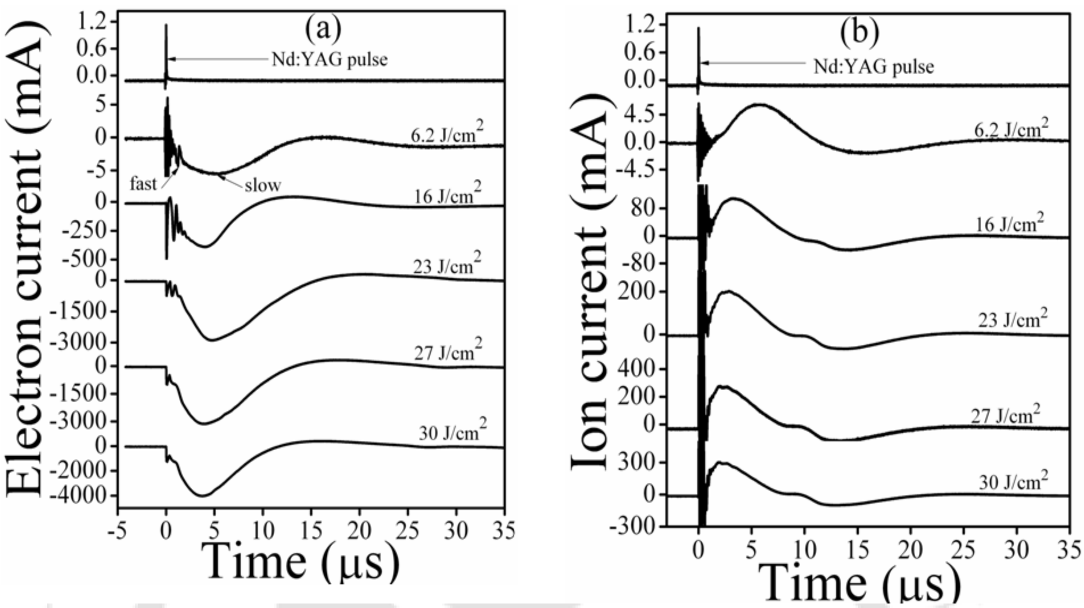

Figure 3.7 *(a) Electron TOF signal as a function of laser fluence (b) corresponding ion TOF signals.*

-cities estimated using equation (2.3) (section 2.3, chapter 2), is shown in figure 3.8.

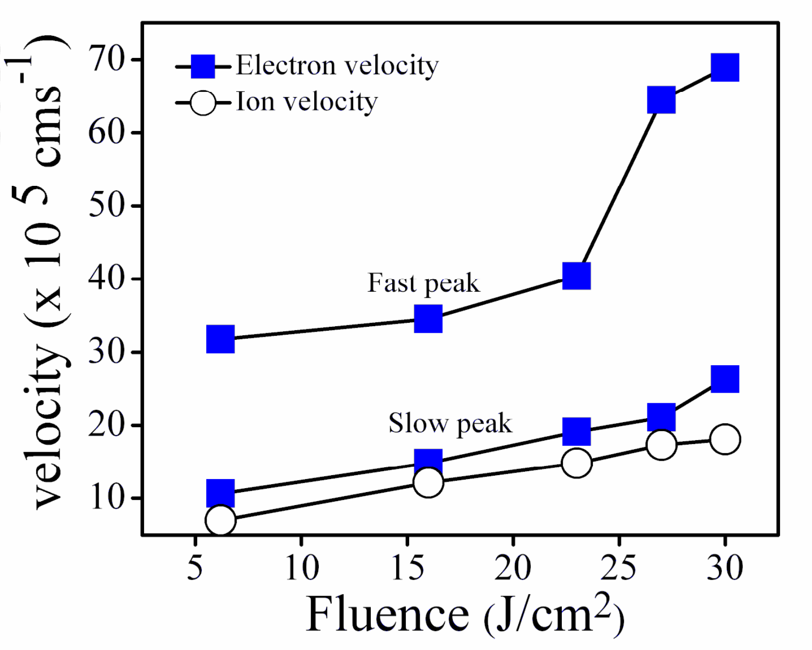

Figure 3.8 *Electron and ion velocities at various fluences.*

The electron velocity was found to increase from 3.1 × 10^6 cms^{-1} to 6.8 ×10^6 cms^{-1} in case of fast peak, on increasing the fluence, from ~ 6.2 J/cm^2 to ~ 30 J/cm^2. In case of slow peak also similar behavior was observed. The electron velocity was found to vary from 10.0 × 10^5 cms^{-1} to 2.6 × 10^6 cms^{-1}. The ion velocity was found to increase from 7.0 × 10^5 cms^{-1} to 1.8 × 10^6 cms^{-1} on increasing the laser fluence from ~ 6.2 J/cm^2 to ~ 30 J/cm^2. Figure 3.9 shows the I-V plot of the probe at various laser fluences. The inset of figure 3.9 shows a semi-logarithmic plot of the I–V curve for the laser fluence of ~ 30 J/cm^2. The temperature was found to increase from 0.5 eV to 3.2 eV on increasing the laser fluence as shown in figure 3.10 (a). The error in the estimation of electron temperature was in the range 0.15 eV to 0.18 eV. The ion density was also found to

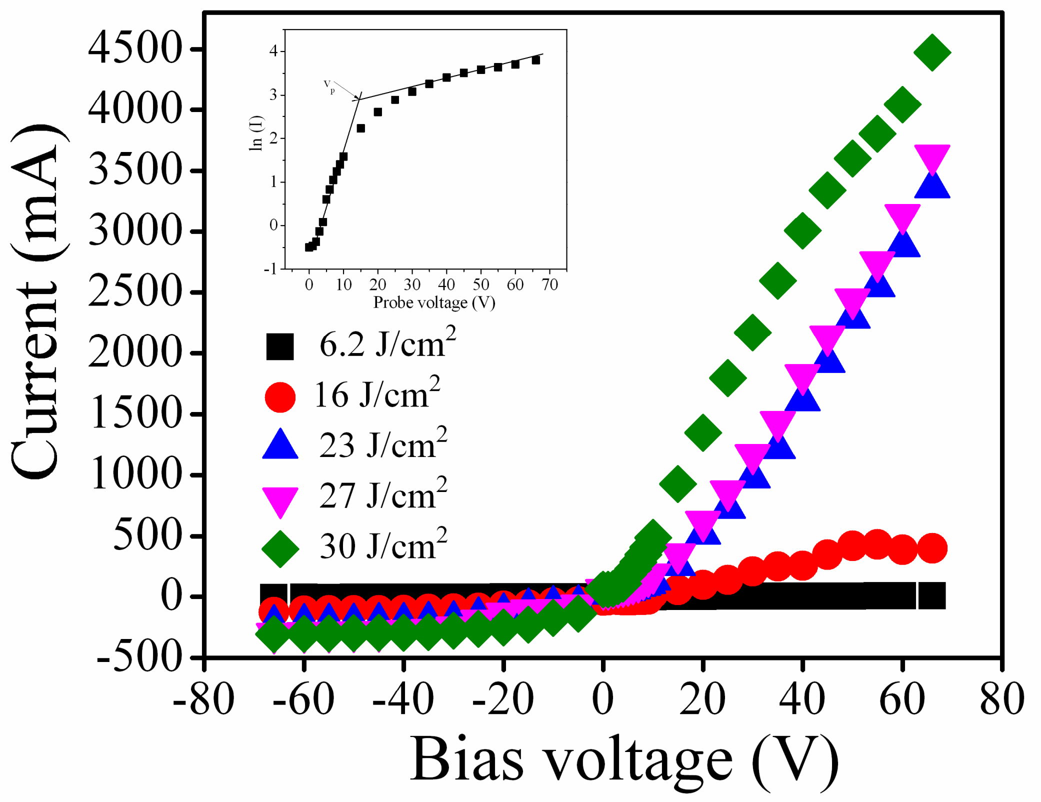

Figure 3.9 *I-V characteristics at various laser fluences.*

increase from 3.6 × 10^{11} cm^{-3} to 6.8 × 10^{12} cm^{-3} with increase in laser fluence from ~ 6.2 J/cm^2 to ~ 30 J/cm^2. The increase in plasma temperature and density was fast upto a laser fluence of ~ 23 J/cm^2. Beyond ~ 23 J/cm^2, the plasma temperature and density shows the trend towards saturation. This could be due to formation of self regulating regime near the target surface at high laser fluence [**184**]. The absorption of the laser photons by the plasma becomes higher due to high plasma density and thus increases the plasma temperature. This in turn curtails the ablation of the charged species from the target, which in turn hampers the growth of density of the charged species.

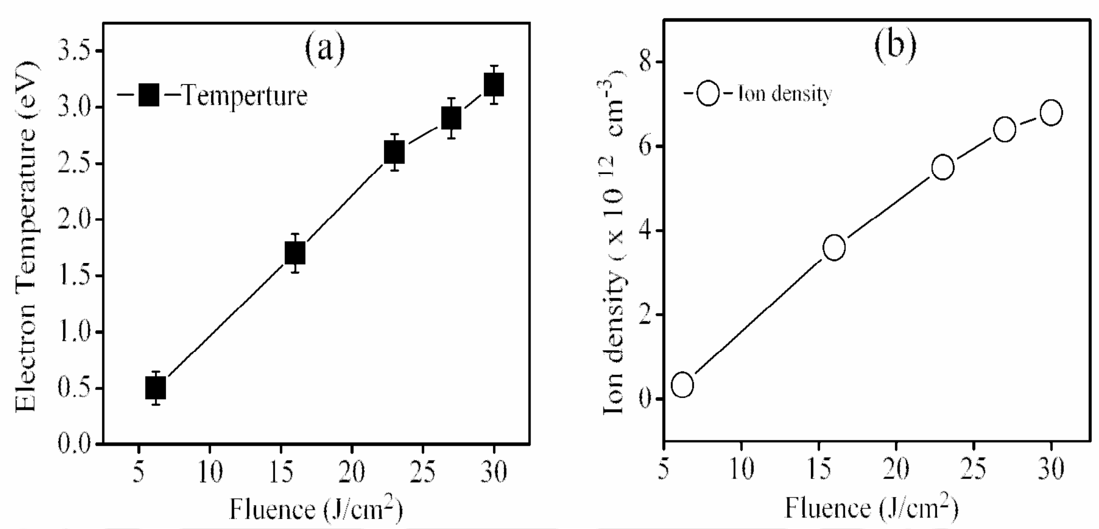

Figure 3.10 *Variation of (a) plasma temperature and (b) ion density as a function of laser fluence.*

Therefore, a laser fluence of ~ 23 J/cm^2 can be considered as optimum laser fluence for deposition of ruby thin film.

3.3. Estimation of electron and ion velocities, electron temperature and ion density as a function of gas pressure

The dependence of LPP parameters on the background oxygen pressure was recorded by placing the probes at a distance of 40 mm away from the target and at a laser fluence of ~ 23 J/cm^2. The oxygen gas pressure was varied from ~ 10^{-5} mbar to ~ 10 mbar. Figure 3.11 shows the electron and ion TOF signals as a function of background gas pressure.

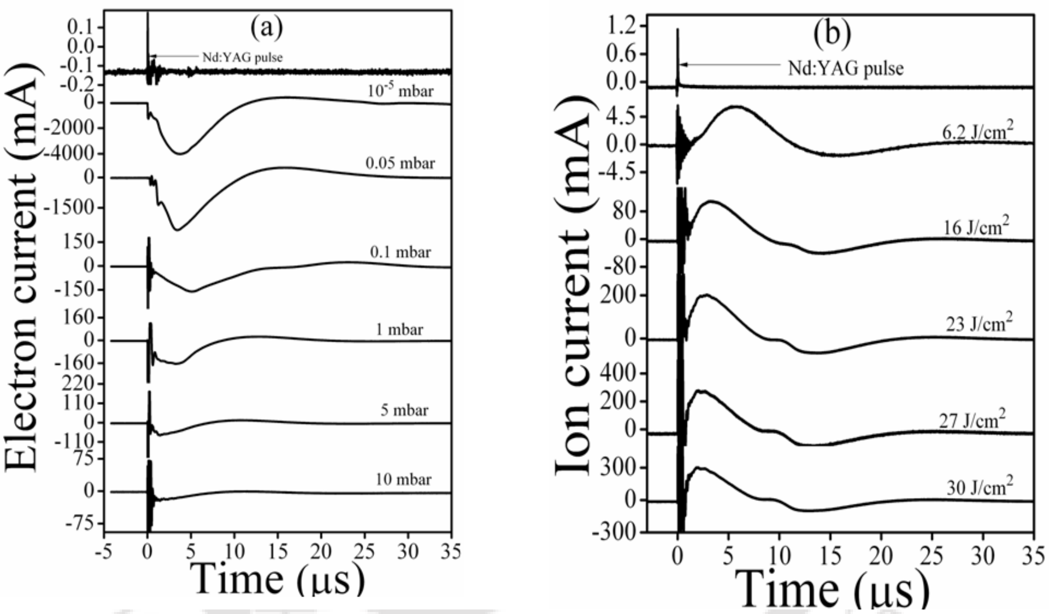

Figure 3.11 *(a) Electron TOF signal as a function of gas pressure (b) corresponding ion TOF signals.*

The collection of electron and ion by the probe was very large in vacuum but with increase in gas pressure it reduced drastically. The reduction in electron/ion current with increase in background gas pressure is primarily due to loss of charged species on collision with background gas molecules. Moreover, the collision rate will further increase due to confinement of plasma with increase in gas pressure. This will further lead to reduction in electron/ion current.

The electron and ion velocities estimated from the electron and ion TOF signals of figure 3.11 using equation (2.3) (section 2.3, chapter 2), is shown in figure 3.12. The electron velocity for fast peak was found to decrease marginally around a value of 64 × 10^5 cms^{-1}, with increase in pressure from ~ 10^{-5} mbar to ~ 10^{-1} mbar. Beyond ~ 10^{-1} mbar it falls down gradually to 25 × 10^5 cms^{-1} at a gas pressure of ~ 10 mbar.

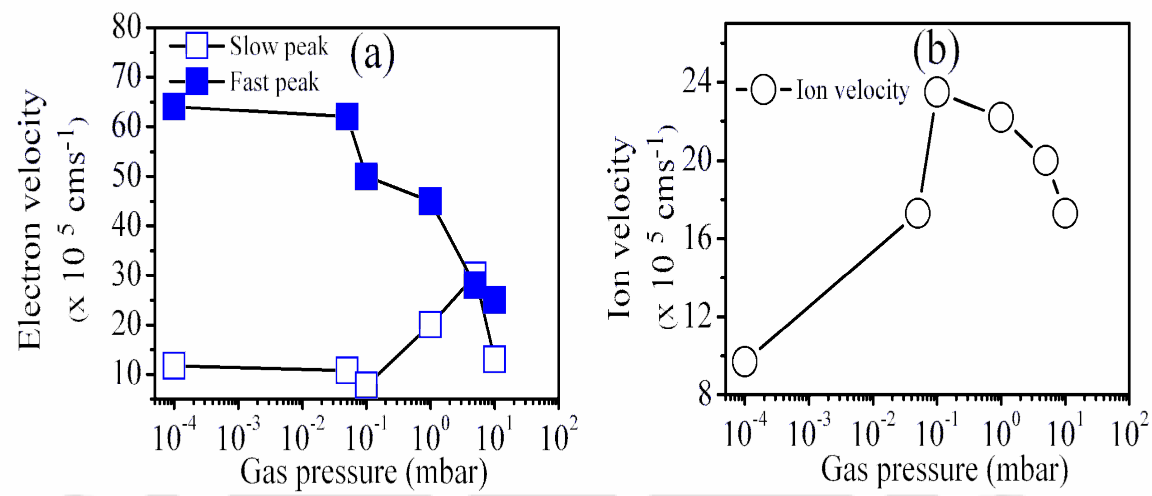

Figure 3.12 *Electron and ion velocities as a function of gas pressure.*

In case of slow peak, it is nearly constant upto 10^{-1} mbar of O_2 pressure and then it increased from 11.7× 10^5 cms^{-1} to 30.3 × 10^5 cms^{-1} upto ~ 5 mbar & then reduced to 13.2 × 10^5 cms^{-1} at ~ 10 mbar, figure 3.12 (a). The ion velocity was increased from 9.7 × 10^5 cms^{-1} to 22.2 × 10^5 cms^{-1}, with increase in oxygen pressure from ~ 10^{-5} mbar to ~ 10^{-1} mbar, and then decreased to 17.3 × 10^5 cms^{-1} on further increasing the pressure to 10 mbar, figure 3.12 (b). The I-V characteristics as a function of gas pressure is shown in figure 3.13. With increase in gas pressure, the slope of I-V curve was found to reduce, due to reduction in electron/ion signals. The electron temperature and ion density as a function of oxygen gas pressure is estimated using equation (2.1) & (2.2) (section 2.3, chapter 2) respectively and is shown in figure 3.14. The electron temperature initially increases from 0.8 eV to 3.8 eV, on increasing the pressure from ~ 10^{-5} mbar to ~ 5 × 10^{-2} mbar. On further increasing the pressure from ~ 0.1 mbar to ~ 10 mbar the electron temperature was found to reduce from 2.5 eV to 0.5 eV as shown in figure 3.14 (a). The error in the estimation of electron temperature is in the range of 0.11 to 0.15 eV.

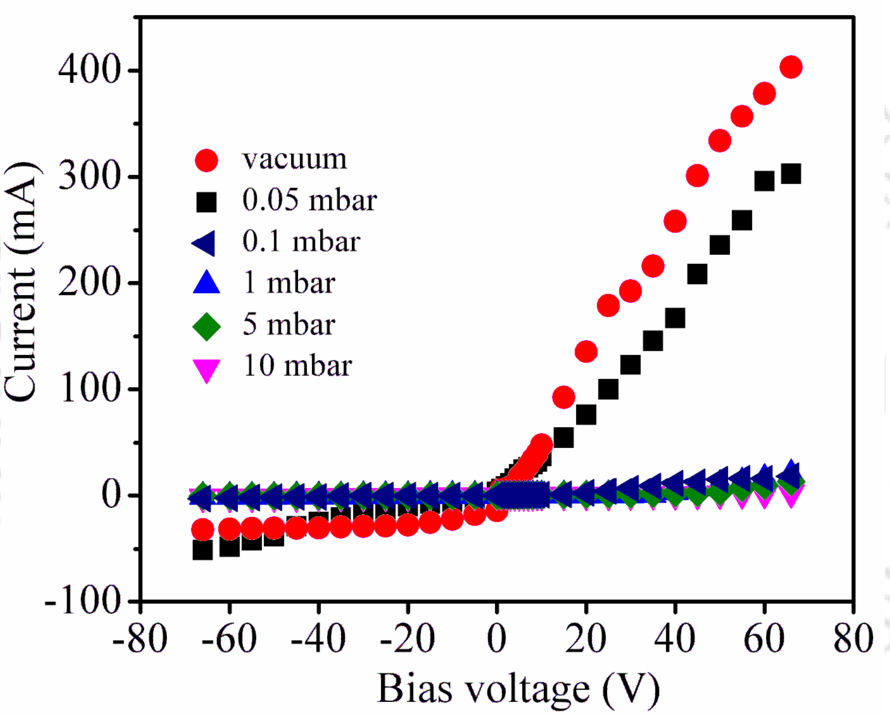

Figure 3.13 *I-V characteristics as a function of gas pressure.*

The ion density was observed to reduce from 2.1 ×10^{12} cm^{-3} to 6.2 × 10^{10} cm^{-3}, on increasing the gas pressure from ~ 10^{-5} mbar to ~ 10 mbar. The fall in ion density was drastic from ~ 10^{-5} to ~ 10^{-1} mbar and beyond that it is almost constant. As the pressure increases, the confinement of the plasma takes place near the target surface [**198**] this results in the increase in the electron collision rate with the background gas atoms.

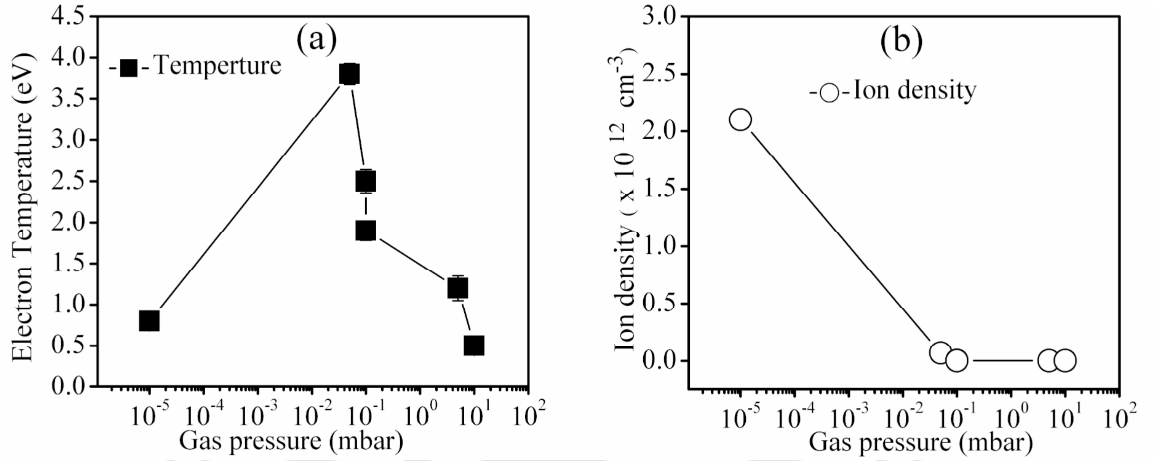

***Figure 3.14** Variation of (a) plasma temperature and (b) ion density as a function of gas pressure.*

Beyond ~ 10^{-1} mbar, the recombination process dominates. This could result in deposition of thicker film via PLD. The effect of gas pressure on deposition of thin film via PLD is detailed in chapter 4 supporting the above observation.

Conclusion

Laser produced plasma (LPP) of ruby was studied by using planar Langmuir probe. Effect of target-substrate distance, laser fluence and background gas pressure on the plasma parameters is worked out. The plasma temperature and density was found initially to increase with increase in laser fluence and then shows slow growth at higher laser fluences. On increasing the background gas pressure, due to plasma confinement collision of charged species and recombination processes leads to decrease in plasma density. Beyond ~ 10^{-1} mbar the neutral formation in the LPP plume dominates. These investigations are helpful in obtaining the optimized deposition parameters via PLD.

Chapter 4

Pulsed laser deposition and characterization of Ruby thin film

Ruby consists of sapphire (α-Al_2O_3) in which a small percentage of Al^{3+} ions are replaced by Cr^{3+} ions. The Cr^{3+} ion has three d-electron in its unfilled shell [**2**]. Transition among the levels of Cr^{3+} ion in the host lattice gives photoluminescence in visible region of the electromagnetic spectrum. The characteristic photoluminescence occurs at 694.2 nm and 692.8 nm, termed as R_1 and R_2 lines respectively [**3-6**]. Ruby possesses favorable combination of relatively narrow line-width, a long fluorescence lifetime, high quantum efficiency, broad and well-located pump absorption bands and very high nonlinear optical coefficients [**5-7, 30, 31**]. In order to exploit these properties of ruby in the form of miniaturized sensor for photonics and electro-optic devices, it is required to be grown in the form of thin film.

Pulsed laser deposition (PLD) technique can be easily employed to grow crystalline thin film of ruby. Polycrystalline ruby thin film on silicon substrate is reported via PLD technique [**199**]. The effect of various growth parameters on quality of ruby thin films via PLD is not documented in literature. In this chapter, the effect of substrate temperature, laser fluence, background gas pressure, deposition time and nature of substrate, on quality of deposited film of ruby is presented.

4.1 Experimental details

Preparation of ruby target and details of the PLD setups have already been detailed in chapter 2, section 2.2. The pellets of ruby having 0.05 wt%, 0.5 wt% and 1 wt% of Cr_2O_3 in Al_2O_3 were prepared. Small quantity of the pellet (0.5 wt% doped) in the form of powder was subjected to HRTEM for confirmation of the ruby phase. The emission and excitation spectra of all the three pellets were recorded by Edinburg instrument, FS-920P (Commercial fluorimeter with double monochromator) by exciting with 532 nm radiation from a Xenon lamp. Confocal image of target pellet (0.5 wt%), was recorded by confocal laser scanning microscope (Carl Zeiss, LSM 510 Meta) using 543 nm laser as the excitation source. The first set of PLD depositions was performed at RT, 650 ˚C and 750 ˚C on the quartz substrate, at target to substrate distance of 5 cm and gas pressure ~ 2 × 10^{-3} mbar of oxygen. The details of these samples are listed in table 4.I (sample 1-sample 5). Further, ruby thin films were deposited on sapphire substrate for 30 min, 1 hr and 2 hrs (sample 6- sample 8; table 4.I). The effect of substrate on quality of ruby thin film is studied by comparing sample 4 and sample 7, deposited under similar experimental conditions. The ruby film deposited on sapphire substrate (sample 6-sample 8) were annealed at 1000˚C for 2 hrs (sample 9 –sample 11). At the optimized substrate temperature, 750˚C, second set of depositions, samples 12-17, were performed by varying the laser fluence from ~ 2 J/cm^2 to ~ 30 J/cm^2 on quartz substrate, by keeping the background gas pressure ~ 0.05 mbar, deposition time 1 hr and substrate to target distance 4 cm fixed, table 4.III. From above, at the optimized fluence of ~ 23 J/cm^2, substrate temperature 750˚C, substrate to target distance of 4 cm and deposition time 1 hr, oxygen gas pressure was varied from ~ 0.05 mbar to ~ 10 mbar, the details of these samples, 18-22, are listed in table 4.IV. Further, deposition time was varied from 30 min to 6 hrs at optimized laser fluence ~ 23 J/cm^2 to obtain the higher thickness of the film on quartz substrate. The other parameters; substrate to target distance 4 cm, substrate temperature 750 ˚C, gas pressure ~ 0.05 mbar were kept constant. Details are listed in table 4.V. Finally, at optimized laser fluence ~ 23 J/cm^2 and oxygen pressure ~ 5 mbar, epitaxial ruby thin film was deposited on polished (both sides) sapphire substrate for 6 hrs as enlisted in table 4.VI.

4.2 Characterization of ruby target pellet

The intense red confocal image of one of the pellet (0.5 wt% of Cr_2O_3), on excitation with 543 nm green He-Ne laser, is shown in figure 4.1 (a), confirming the ruby phase. HRTEM image from the pellet is shown in the figure 4.1 (b), the measured d-spacing of 0.261 nm is in agreement for the ruby phase reported in literature [**200**]. Raman spectra of alumina and chromium oxide powder and the sintered pellet (0.5 wt% of Cr_2O_3) prepared from the powder are shown in the figure 4.2. Absence of any well-defined band in the Raman

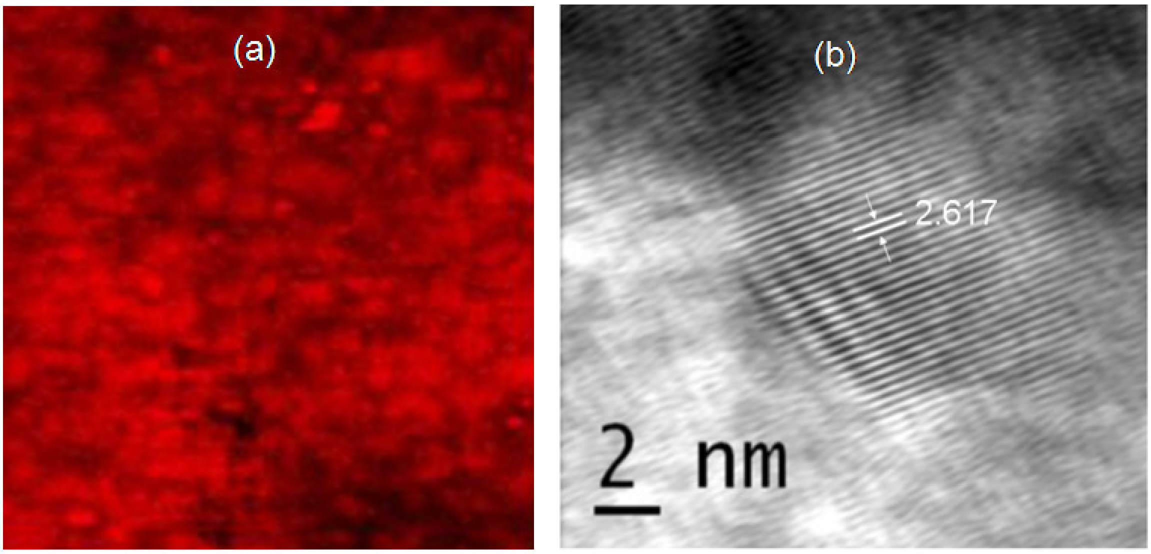

Figure 4.1*(a) Confocal image and (b) HRTEM of pellet.*

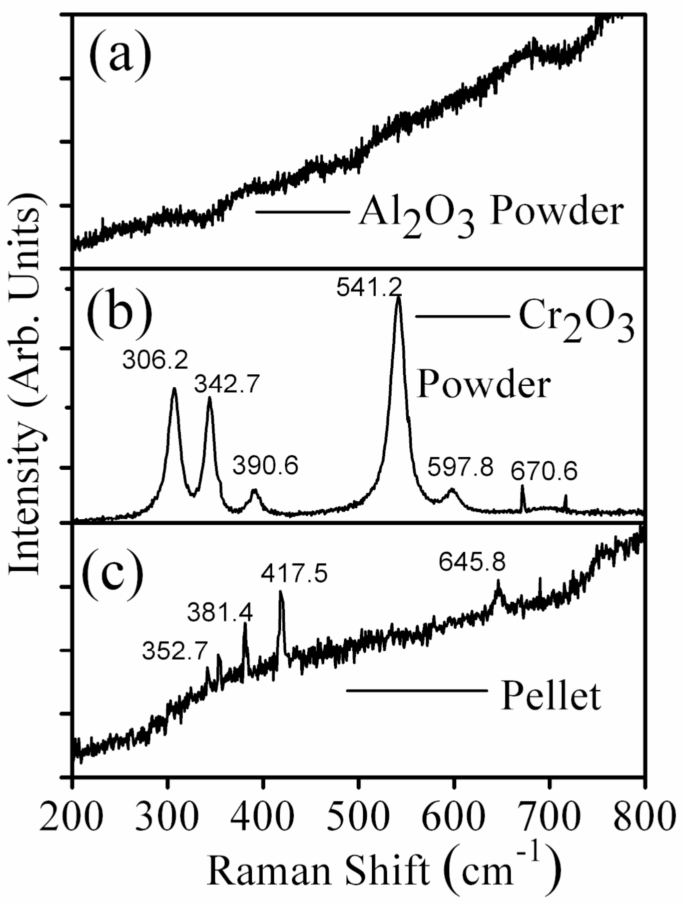

Figure 4.2 *Raman spectra of (a) γ phase alumina powder (b) Cr_2O_3 powder (c) Sintered Pellet (0.5 wt %).*

spectrum of alumina as shown in figure 4.2 (a) indicated the γ- Al_2O_3, which is Raman inactive [**201**]. Figure 4.2 (b) shows the Raman bands of commercial chromium oxide powder (Cr_2O_3) used for the pellet. The observed bands at 306.2, 342.7, 390.6, 541.2, 597.8 and 670.6 cm^{-1} are in agreement with the Raman bands of Cr_2O_3, as reported in literature [**202**]. The Raman bands of sintered pellet (0.5 wt% of Cr_2O_3) are shown in figure 4.2 (c). The observed Raman bands are located at 352.7, 381.4, 417.5 and 645.8 cm^{-1}. The Raman bands at 381.4, 417.5 and 645.8 cm^{-1} corresponds to the corundum phase [**203, 204**]. The LO band at 417.5 cm^{-1} in the pellet is signature of ruby phase [**203**]. Figure 4.3 (a) & (b) shows respectively the excitation and emission spectra of ruby pellets for three different chromium concentrations 0.05 wt%, 0.5 wt%, and 1.0 wt% in alumina. Two broad absorption bands centered at 402 nm and 554 nm in figure 4.3 (a) correspond to the blue and green absorption bands of ruby. These bands centered at 402 nm and 554 nm are associated with the spin-allowed transitions from the $^4A_2$ ground state to the $^4F_1$ excited state (Y-band) and to the $^4F_2$ excited state (U-band) respectively as shown in figure 4.4. The weak B lines in absorption states, figure 4.3 (a)

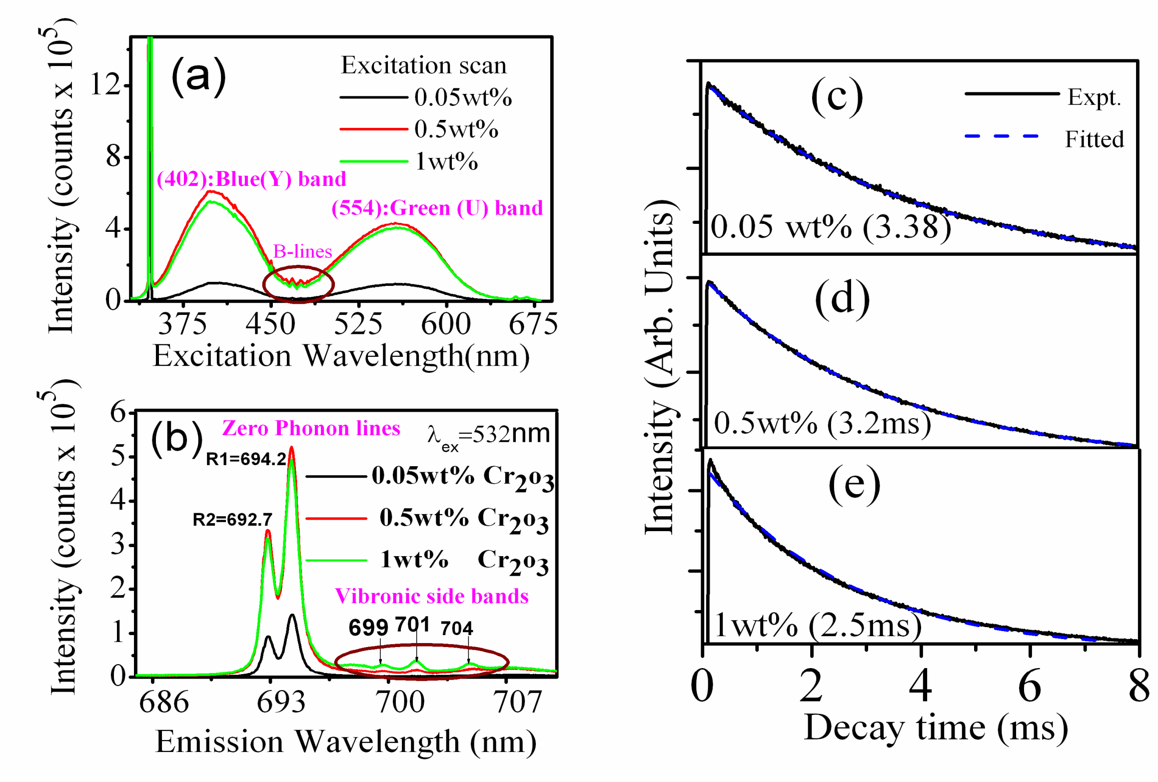

__Figure 4.3__ (a) Excitation & (b) emission (PL) spectra of ruby pellets. Corresponding decay time of R_1 line for (c) 0.05 wt%, (d)0.5 wt% and (e) 1wt%, solid line experimental curve, and broken line (blue) exponential fit.

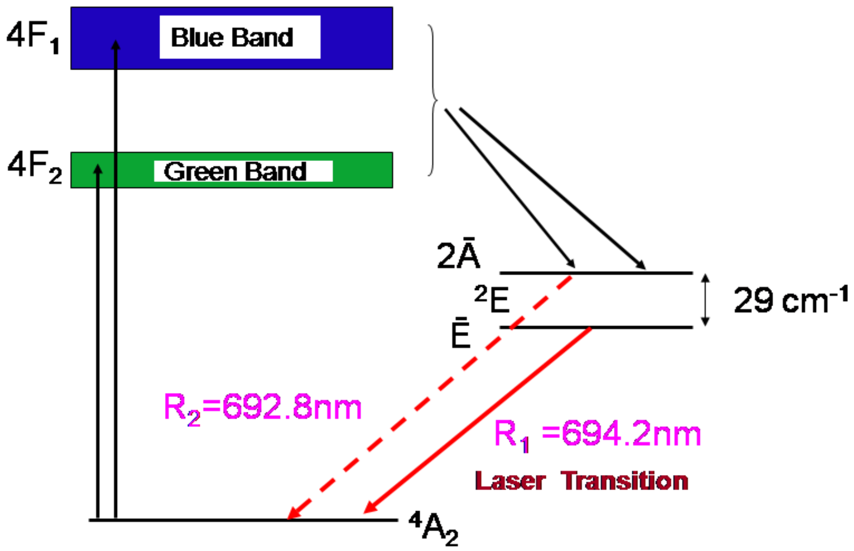

Figure 4.4 *Energy level diagram of ruby.*

are associated with the spin-forbidden transition to the doublet levels [**2**]. Figure 4.3 (b) shows the Photoluminescence spectra of ruby pellets consisting of well resolved R_1 & R_2 lines at 694.2 nm and 692.7 nm respectively. In ruby, this bright red light emission results from electronic transitions that take place exclusively at the Cr^{3+} ions across ^2E and $^4A_2$ states. The ^2E states are excited via fast transition from absorption bands (pump bands). The lifetime of the pump bands, are extremely short, with the ions transferred to a metastable 2Ā and Ē states immediately. The two transitions, Ē $\rightarrow {}^4A_2$ and 2Ā $\rightarrow {}^4A_2$, emitting in red end of the visible spectrum at 694.2 nm and 692.8 nm are referred as the R_1 and R_2 lines respectively. These lines are zero phonon lines. The separations of these two lines are about 29 cm^{-1} at room temperature. The sharp R-line fluorescence from the pellet provides the direct evidence that a substantial proportion of Cr^{3+} ions behave as substitutional solute on the Al^{3+} sites in the corundum structure. The spectra, of figure 4.3 (b) clearly shows that there is a multifold increase in emission of R-line by increasing the concentration of chromium from 0.05 wt% to 0.5 wt%, but on increasing the concentration further to 1.0 wt%, there is slight decrease in PL intensity due to quenching, because of excessive concentration of Cr^{3+} ions in ruby pellet [**20**]. Along with the sharp zero phonon lines, broad vibronic side bands at 699, 701, 704 nm and few more weak bands with very low intensity were observed in the emission spectrum of ruby pellet. These broad bands are associated with multiphonon vibronic transitions originating from the ^2E level from the electrostatic interaction of the electronic states of the ions with vibrations of the host lattice and contains information not only on the phonon normal modes of the crystal lattice but also on the strength and symmetry properties of the electron–phonon coupling. It can be seen from Figure 4.3 (b) that the vibronic side bands are becoming more pronounced by increasing the chromium concentration due to increase in Cr^{3+} pairs [**7-9**]. Figure 4.3 (c), (d) and (e) shows the decay of R_1-line after excitation with microsecond flash lamp. The decay time is observed to be 3.38 ms for 0.05 wt% doped pellet, which reduces to 3.20 ms for 0.5 wt% doping and then finally it drops down to 2.51 ms for 1.0 wt% doped pellet and is in excellent agreement with literature [**20**]. Since the pellet with 0.5 wt% showed maximum PL emission, as evident from figure 4.3 (b), hence it was used as target for Pulsed laser deposition of thin films of ruby on quartz and sapphire substrate, under various experimental conditions.

4.3 Effect of various deposition parameters on quality of PLD deposited ruby thin films

The ruby thin films were deposited by varying substrate temperature, substrate, laser fluence, gas pressure and deposition time.

4.3.1 Effect of substrate temperature, substrate & post annealing on PLD Ruby thin films

Table 4.I lists the details of sample grown at RT, 650 ˚C and 750 ˚C at a laser fluence of ~ 23 J/cm^2, substrate to target distance of 5 cm and oxygen gas pressure ~ 2 × 10^{-3} mbar on quartz as well as sapphire substrate. Sample 3 and sample 9 to sample 11were obtained by annealing sample 2 and sample 6 to sample 8 respectively. The thickness and the corresponding deposition rates for all the PLD deposited thin films of ruby on quartz and sapphire substrate are also listed in table 4.I. Sample 1 and sample 2,

Table 4.I: *List of PLD grown ruby thin films under various deposition conditions.*

Sample name	**Deposition parameters**					
	Substrate	**Deposition time**	**Substrate temperature**	**Post-annealing**	**Thickness (nm)**	**Deposition Rate (nm/min)**
Sample 1	Quartz	2 hrs	RT	——	190	1.5
Sample 2	Quartz	4 hrs	RT	——	400	1.5
Sample 3 (annealed sample2)	Quartz	4 hrs	RT	1000°C for 2 hrs	400	1.5
Sample 4	Quartz	1 hr	650°C	——	100	1.7
Sample 5	Quartz	1 hr	750°C	——	110	1.8
Sample 6	Sapphire	30 min	650°C	——	55	1.8
Sample 7	Sapphire	1hr	650°C	——	120	2.0
Sample 8	Sapphire	2 hrs	650°C	——	260	2.16
Sample 9 (annealed sample 6)	Sapphire	30 min	650°C	1000°C for 2 hrs	55	1.8
Sample 10 (annealed sample 7)	Sapphire	1hr	650°C	1000°C for 2 hrs	120	2.0
Sample 11 (annealed sample 8)	Sapphire	2 hrs	650°C	1000°C for 2 hrs	260	2.16

deposited on quartz substrate at RT, were found to have a thickness of 190 nm and 400 nm respectively. No observable changes in thickness were observed after annealing of sample 2. The deposition rate was found to be ~ 1.5 nm/min. Sample 4 and sample 5 deposited at elevated temperature of 650˚C and 750˚C each deposited for 1 hr , was found to have a thickness of 100 nm and 110 nm and the corresponding deposition rate was found to be 1.7 nm/min and 1.8 nm/min respectively. Thus, the deposition rate was found to increase marginally on increasing the substrate temperature from RT to 750˚C. The thin films deposited on sapphire substrate; sample 6, sample 7 and sample 8 deposited for 30 min, 1 hr & 2 hrs respectively, were found to have a thickness of 55 nm, 120 nm and 260 nm respectively. The deposition rate was found to increase from 1.8 nm/min to 2.16 nm/min, on increasing the deposition time from 30 min to 2 hrs, from sample 6 to sample 8, respectively. The effect of substrate on deposition rate can be observed from sample 4 (quartz) and sample 7 (sapphire), which are deposited under similar deposition conditions. It clearly shows the 10% increase in the deposition rate on the sapphire substrate as compared to that of quartz. This could be due to lattice matching on sapphire substrate and thus efficient growth as compared to quartz substrate.

The XRD spectra of ruby thin films grown on sapphire and quartz substrate, along with the pellet are shown in figure 4.5. The XRD spectrum of pellet is showing peaks at 25.5˚ (012), 35.14˚ (104), 37.7˚ (110), 43.3˚ (113), 52.5˚ (024), 57.4˚ (116), 61.2˚ (211), 66.4˚ (214) and 68.2˚ (214) [ICSD Collection code: 089665] confirming its polycrystalline nature. The thin films grown on quartz substrate (sample 1 to sample 5; table 4.I) are of amorphous nature as these peaks in the XRD spectra are missing. As an example, XRD of sample 4 on quartz is shown in figure 4.5. The as deposited PLD thin films on

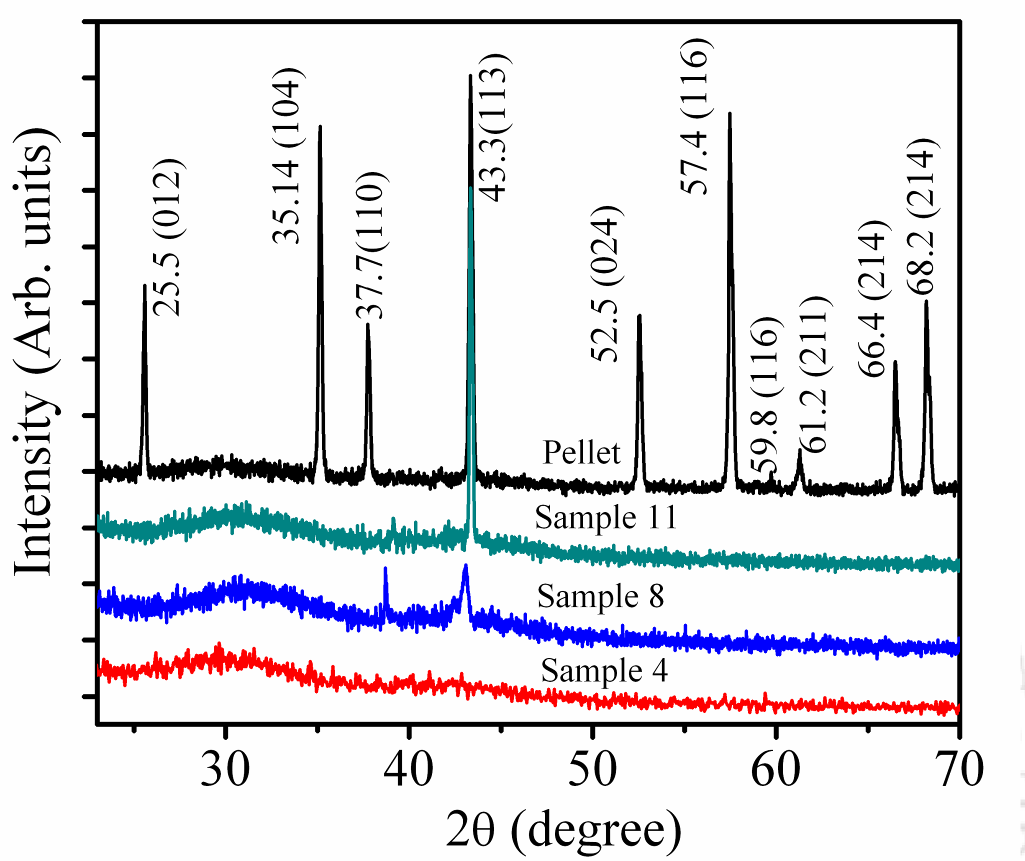

Figure 4.5 *XRD of target pellet and ruby films grown on quartz and sapphire substrate.*

sapphire substrate, for example sample 8, showed diffraction peak at 43.3° corresponding to the C-axis growth. Post annealed spectrum of sample 8 at 1000°C for 2 hrs (referred as sample 11) shows enhanced signal at 43.3° confirming the highly C-axis oriented ruby film.

Figure 4.6 shows the Raman spectra of post annealed PLD thin films of ruby deposited on sapphire substrate, corresponding to sample 9, 10 and 11 (table 4.I), along with bare sapphire substrate. Inset shows the Raman spectra of sample 4. The spectra of bare substrate shows 6 Raman bands located at 379 (TO), 418 (LO), 431 (TO), 450 (LO), 577 (LO) and 750 (LO) cm^{-1}. All these observed Raman modes of substrate are in agreement with the spectrum of C-plane of (α-Al_2O_3) sapphire [**203-205**]. The as deposited thin films of ruby on quartz at RT do not show any prominent peak in Raman spectra (sample 1 & sample 2). Even post annealed films on quartz (sample 3) does not show any Raman peak indicating the amorphous nature in agreement with XRD observation. The film grown on quartz substrate at a substrate temperature of 650°C (sample 4) shows Raman bands at 370.70 cm^{-1}, 415.85 cm^{-1}, 443.40 cm^{-1}, 512.00 cm^{-1} & 746.30 cm^{-1} as shown in inset of figure 4.6. The Raman bands at 379 cm^{-1} corresponds to the transverse optical (TO) modes of E_g vibrations. The other bands at 415.85 cm^{-1},

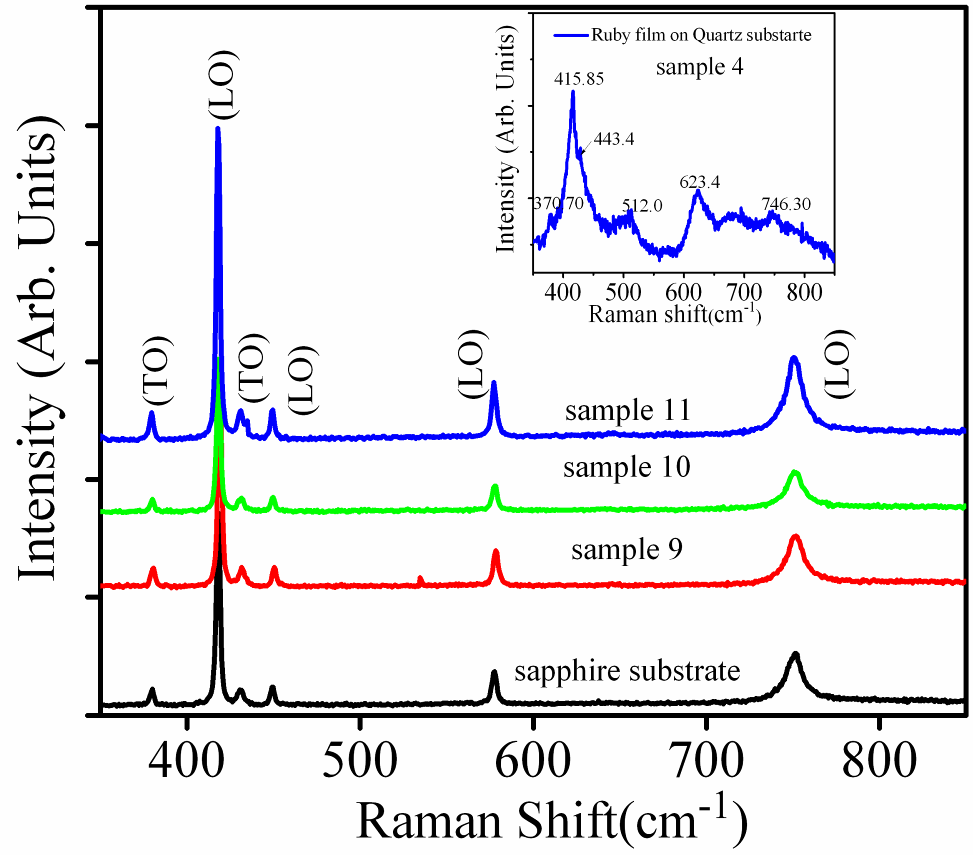

Figure 4.6 *Raman spectra of bare sapphire substrate and PLD ruby thin films corresponding to sample 9, sample 10 and sample 11. Inset shows the Raman spectra of film grown on quartz substrate; sample 4.*

512.00 cm^{-1} and 746.30 cm^{-1} corresponds to longitudinal optical (LO) modes of E$_g$ vibrations. The LO band observed at 415.85 cm^{-1}, downshifted to 2.15 cm^{-1} compared to bulk, in the Raman mode is attributed to the stress present in the film due to lattice mismatch between the substrate (quartz) and the deposited film. Broadening in the peak as observed from the FWHM of sample 4 as compared to sapphire substrate from table 4.II, can be attributed to the amorphous nature of the grown film on quartz substrate.

Table 4.II: *Peak position and FWHM of various Raman bands of PLD ruby film.*

Sample no:	**Peak 1** (FWHM) in cm^{-1}	**Peak 2** (FWHM) in cm^{-1}	**Peak 3** (FWHM) in cm^{-1}	**Peak 4** (FWHM) in cm^{-1}	**Peak 5** (FWHM) in cm^{-1}	**Peak 6** (FWHM) in cm^{-1}
Sapphire substrate	379.06 (2.28)	418.04 (2.23)	430.07 (3.23)	450.00 (2.71)	575.02 (3.02)	750.00 (12.50)
Sample 4 (Quartz)	370.70 (20.03)	415.86 (35.42)	443.40 (96.36)	——	512.00 (40.50)	746.30 (18.04)
Sample 9	380.42 (2.65)	418.97 (2.59)	431.81 (3.70)	450.00 (2.75)	578.38 (3.48)	751.40 (12.90)
Sample 10	379.94 (2.42)	418.58 (2.32)	431.30 (3.22)	449.55 (2.73)	577.72 (3.32)	751.12 (12.69)
Sample 11	379.46 (2.61)	418.27 (2.28)	431.08 (4.13)	449.31 (2.64)	577.42 (3.07)	750.83 (12.45)

The Raman bands of annealed ruby films grown on sapphire substrate showed enhancement in intensity from sample 9 to sample 11. The 418 cm^{-1} (LO) A$_{1g}$ band corresponds to the C-axis orientation is the most intense Raman active band. The Raman band positions and FWHM as enlisted in table 4.II suggests that the PLD deposited films on sapphire substrate are highly C-axis oriented. Thickness of the film increases with the deposition time, sample 9 to 11, and improves the crystallinity of the film as is confirmed by slight reduction in FWHM. No appreciable changes in the peak position and line-width in the Raman spectra of film deposited on sapphire substrate w.r.t. bare substrate confirmed that these PLD ruby thin films are highly crystalline in nature and stress free.

Figure 4.7 shows the Photoluminescence spectra of ruby films deposited on quartz (sample no. 1, 2, 3, 4 & 5) and sapphire substrate, sample 7 (table 4.I). The sharp and distinct peaks at 694.2 nm and 692.8 nm corresponding to R_1 and R_2 lines along with vibronic side bands of ruby were observed in PL of all the samples. The PL intensity of R-line was found to increase on increasing the deposition time from 2 hrs (sample 1) to 4

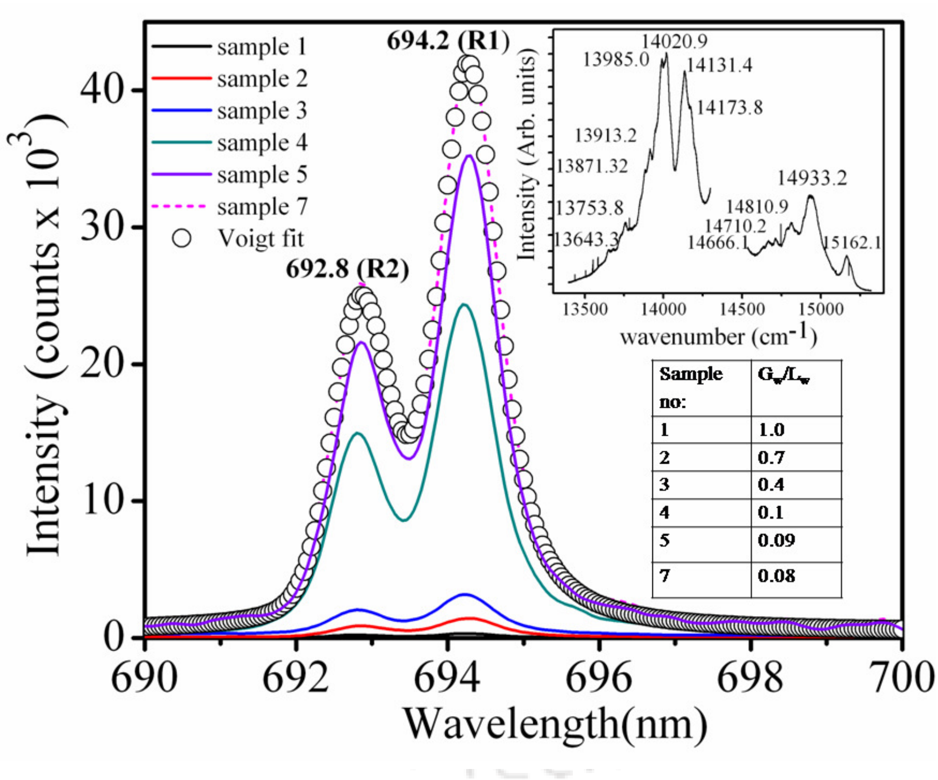

Sample no:	G_w/L_w
1	1.0
2	0.7
3	0.4
4	0.1
5	0.09
7	0.08

Figure 4.7 *Photoluminescence spectra of PLD thin film of ruby sample 1, 2, 3, 4, 5 & 7. Inset shows the vibronic side bands.*

hrs (sample 2) as observed from figure 4.7. This is due to increase in thickness of the film resulting from longer deposition time. The PL intensity of post annealed film, sample 3, was found to improve drastically as compared to that of as deposited sample 2. Annealing improves the crystallinity of the film which results in enhancement of PL intensity. There was no appreciable change in relative intensities of R_1 and R_2 lines and FWHM for sample 2 and corresponding post annealed sample 3. Emission spectra of film grown on quartz substrate for 1 hr at 650 °C substrate temperature, sample 4, shows drastic enhancement in PL emission as compared to that of 4 hrs grown film at room temperature, sample 2, and post annealed at 1000°C, sample 3. The relative intensities of R_1 and R_2 lines increased from 1.75 to 1.79, but no appreciable change in FWHM of the peaks was observed for sample 3 & sample 4. The film grown at 750°C, sample 5, shows further enhancement in PL signal. Deposition at elevated temperature helps in C-axis growth. Thus, substrate heating is more effective than growing the films at RT for longer duration and then post-annealing at higher temperature for PL efficiency. PL spectra of all the PLD ruby films were fitted to voigt line shape and the Gaussian and Lorentzian width were compared. The ratio of Gaussian width (G_w) to Lorentzian width (L_W), listed in inset of Figure 4.7, was found to decrease from 1.02 to 0.08 from sample 1 to sample 7, accordingly the PL intensity was also observed to increase as shown in figure 4.7. Since the Gaussian component accounts for the inhomogeneous broadening of the spectral line profile, it can be concluded that the stress in the film is reduced from sample 1 to sample 7 and the quality of film has been improved, which is also supported by the increase in PL intensity. The vibronic side bands of sample 4 are shown in the inset of figure 4.7. As compared to the target pellet as shown in figure 4.3(b) these bands are more pronounced in the thin film geometry. PL signal from the film grown on sapphire substrate, sample 7, is much higher than that of on quartz (sample 4), due to the lattice matching with sapphire substrate of former, enhancing the crystalline nature of the film as observed from figure 4.7. Figure 4.8 (a) clearly shows the enhancement of PL signal with the increase in deposition time, sample 6 to 8. The PL spectrum of post annealed

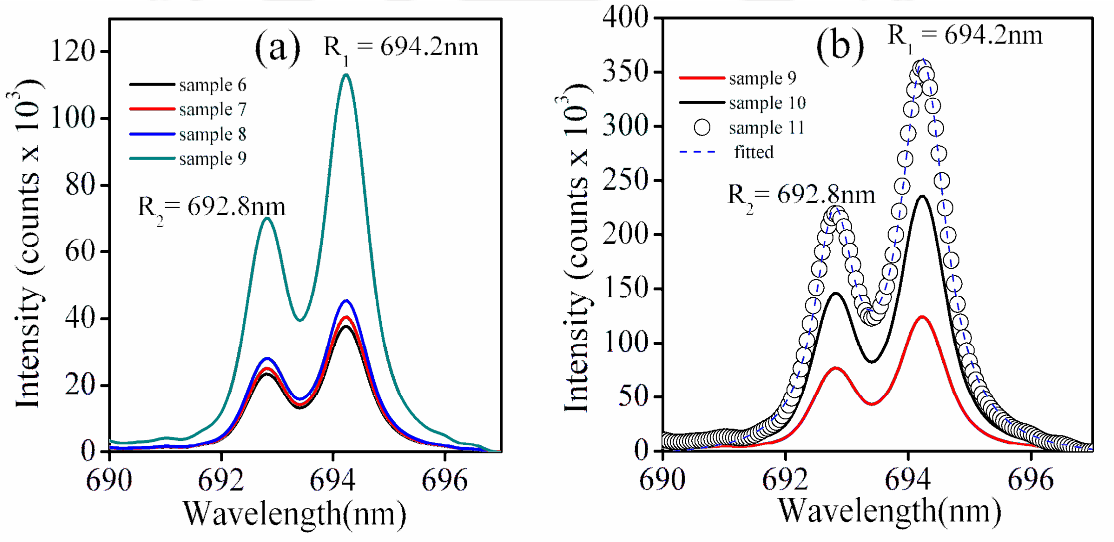

Figure 4.8 *PL spectra of film deposited on sapphire substrate for (a) sample 6, 7, 8 & 9 (b) sample 9, 10, 11and Lorentzian fit of sample 11.*

film, sample 9 (annealed sample 6), shows multifold increase in the intensity of R_1 and R_2 lines as compared to corresponding as deposited sample, sample 6, because post-annealing improves the crystallinity of the film and makes it free from stress. Figure 4.8 (b) compares the PL spectra of post annealed samples 9, 10 & 11. The Lorentzian fitting for sample 11 is also shown in the figure 4.8 (b). It was found to fit very well with double Lorentzian line shape with coefficient of determination, r^2 ~ 0.999, confirming highly crystalline and nearly stress free nature of the PLD deposited ruby film.

4.3.2 Effect of laser fluence on PLD Ruby thin films

To monitor the effect of laser fluence onto the quality of PLD deposited ruby thin films the deposition was performed at six laser fluences; ~ 2 J/cm^2, ~ 6.2 J/cm^2, ~ 16 J/cm^2, ~ 23 J/cm^2 and ~ 30 J/cm^2 at substrate temperature of 750˚C. All these films were annealed at 1000˚C for 2hrs. The details of these samples are enlisted in table 4.III.

Table 4.III: *List of PLD ruby thin films deposited at various laser fluences.*

Sample no	Deposition time (hr)	Gas pressure (mbar)	Laser fluence (J/cm^2)	Thickness (nm)	Deposition Rate (nm/min)	Grain size (nm)	Roughness (nm)
Sample 12	1	0.05	2.0	15	0.25	40.5	6.0
Sample 13	1	0.05	6.2	39	0.65	45.0	6.2
Sample 14	1	0.05	16.0	90	1.50	55.2	4.5
Sample 15	1	0.05	23.0	185	3.08	50.4	2.6
Sample 16	1	0.05	27.0	150	2.50	52.6	3.2
Sample 17	1	0.05	30.0	120	2.00	54.6	4.6

The thickness of the film was found to increase from 15 nm to 185 nm on increasing the laser fluence from ~ 2 J/cm^2 to ~ 23 J/cm^2 as shown in figure 4.9 (a). On further increasing the laser fluence to ~ 27 J/cm^2 and ~ 30 J/cm^2, the thickness drops down to 150 nm and 120 nm respectively. The photoluminescence (PL) intensity of films scales with the increase in laser fluences as shown in figure 4.9 (b). At low laser energy ~ 2 J/cm^2 and ~ 6.2 J/cm^2, the PL spectra does not show any signature of ruby phase in the deposited film as shown in inset of figure 4.9 (b). On increasing the laser fluence to ~ 16 J/cm^2, distinct R_1 and R_2 lines at 694.2 nm and 692.8 nm is observed in the PL spectra, confirming the appearance of ruby phase in the film. On further increasing the laser

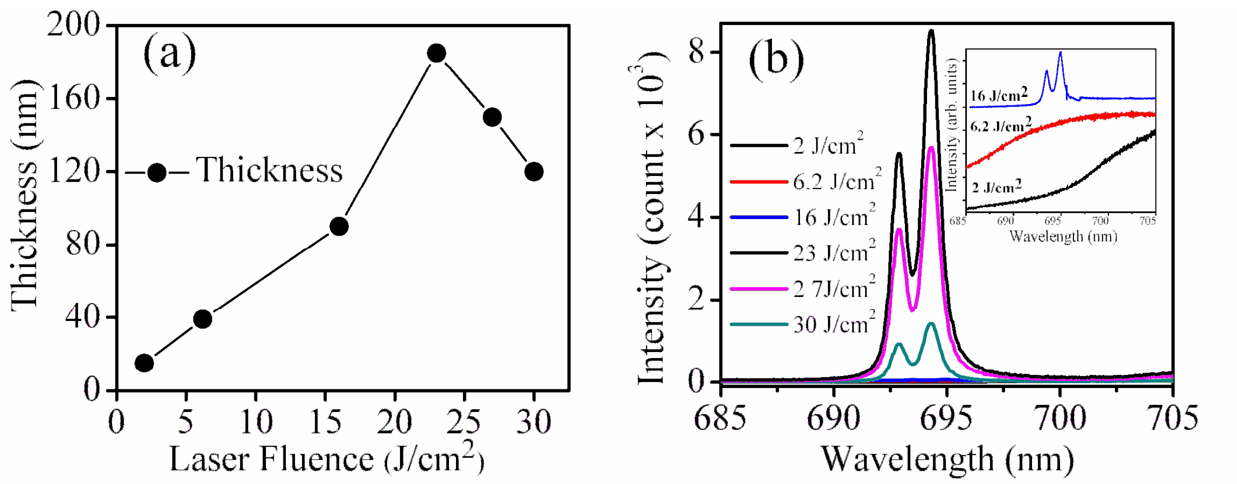

***Figure 4.9** Effect of laser fluence on (a) thickness and (b) photoluminescence of PLD ruby thin film*

energy to ~ 23 J/cm^2, drastic enhancement in PL intensity is observed. The AFM images of PLD ruby thin films are shown in figure 4.10. It shows decrease in surface roughness from 6.0 nm to 2.6 nm on increasing the laser fluence from ~ 2 J/cm^2 to ~ 23 J/cm^2 (table 4.III). The grain size is increased from 40.5 nm to 50.4 nm (table 4.III). At higher laser fluence more particles are ejected from the target surface. Thus the kinetic energy as well as amount of target species arriving onto the substrate surface increases with increases in laser fluence. On arriving the surface of the substrate these particles accumulates to form a larger grain in order to minimize their surface energy [**206, 207**]. Thus higher laser fluence gives rise to a thicker film as shown in figure 4.9(a). Also at high laser fluence, the kinetic energy of ablated material is high which results in good adhesion of the film onto the substrate as well as the formation of crystalline structure. As the laser fluence was further increased to ~ 27 J/cm^2 and ~ 30 J/cm^2, the PL intensity was found to decrease and the surface roughness was increased to 3.2 nm and 4.6 nm respectively. This could be due to sputtering from the film surface on impingement of highly energetic particle on substrate surface. Thus, the optimum laser fluence for deposition of good quality ruby thin film is ~ 23 J/cm^2. Above this laser fluence, the electron velocity increased drastically, as observed from figure 3.8 (chapter 3). Due to rapid increase in

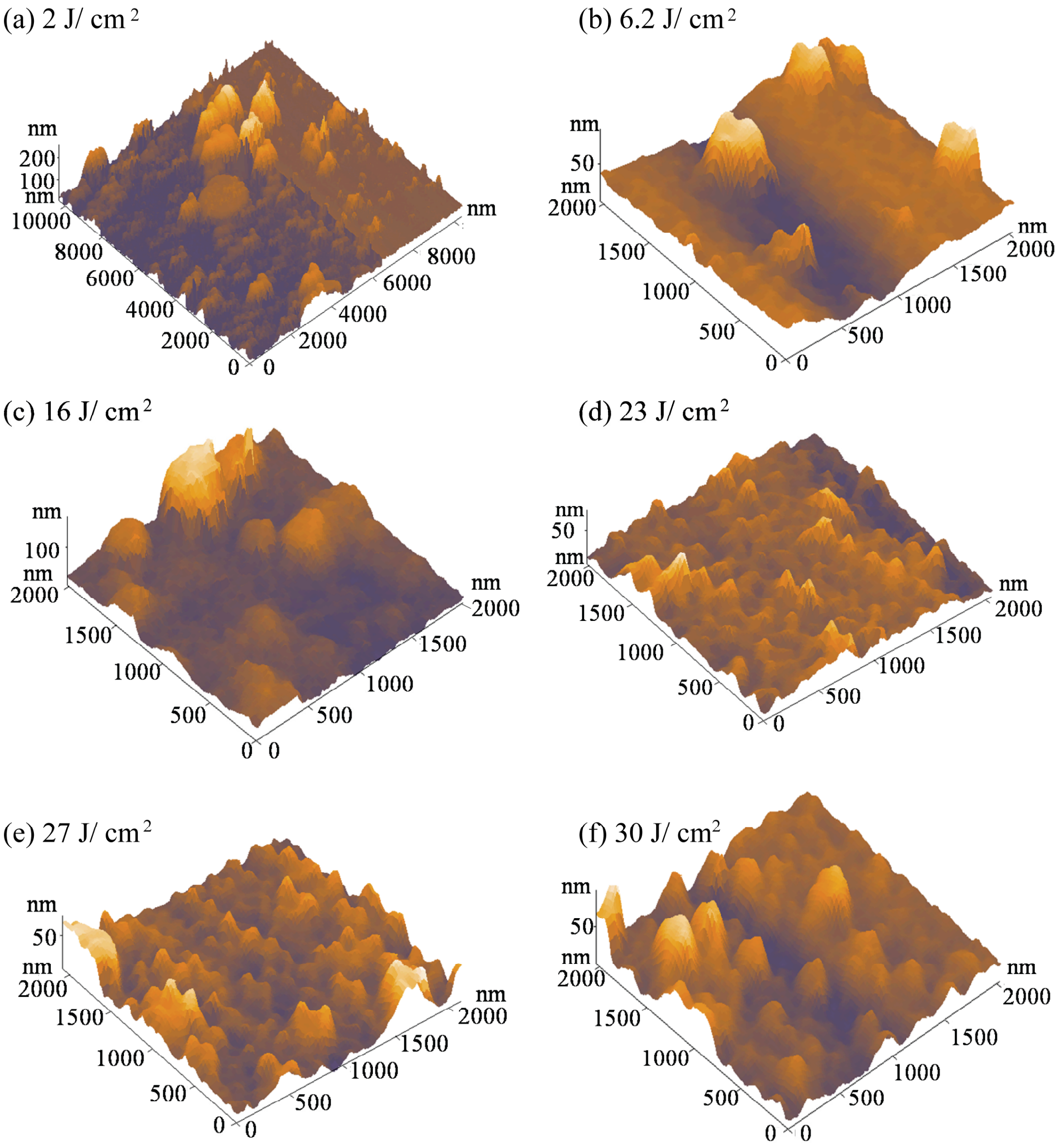

Figure 4.10 *AFM images of PLD ruby thin films deposited at various laser fluences.*

the velocity of plasma species, sputtering from the film surface takes place on impingement of highly energetic particles. Thus the quality of film is deteriorated as reflected from increase in the surface roughness and decrease in PL intensity of ruby thin films deposited at laser fluence of ~ 27 J/cm^2 and ~ 30 J/cm^2.

4.3.3 Effect of background gas pressure on PLD Ruby thin films

To study the effect of background oxygen pressure, ruby thin films were deposited at five different oxygen gas pressures ~ 0.05 mbar, ~ 0.1 mbar, ~ 1 mbar, ~ 5 mbar and ~ 10 mbar at optimum laser fluence of ~ 23 J/cm^2 and at a substrate temperature of 750°C on quartz substrate. The details of these films are given in table 4.IV. Figure 4.11 (a) shows the thickness of PLD ruby thin film as a function of background gas pressure. The thickness of the film was found to increase from 180 nm to 450 nm on increasing the gas pressure from ~ 0.05 mbar to ~ 5 mbar, on further increasing the gas pressure to ~ 10 mbar the thickness was found to decrease to a value of 300 nm.

Table 4.IV: *List of PLD ruby thin films deposited at various gas pressures.*

Sample no	**Deposition time (hr)**	**Gas pressure (mbar)**	**Laser fluence (J/cm^2)**	**Thickness (nm)**	**Deposition Rate (nm/min)**	**Grain size (nm)**	**Roughness (nm)**
Sample 18	1	0.05	23.0	180	3.00	55.50	2.05
Sample 19	1	0.1	23.0	210	3.50	62.90	2.97
Sample 20	1	1	23.0	340	5.67	95.21	3.80
Sample 21	1	5	23.0	450	7.50	105.00	5.48
Sample 22	1	10	23.0	300	5.00	120.00	5.92

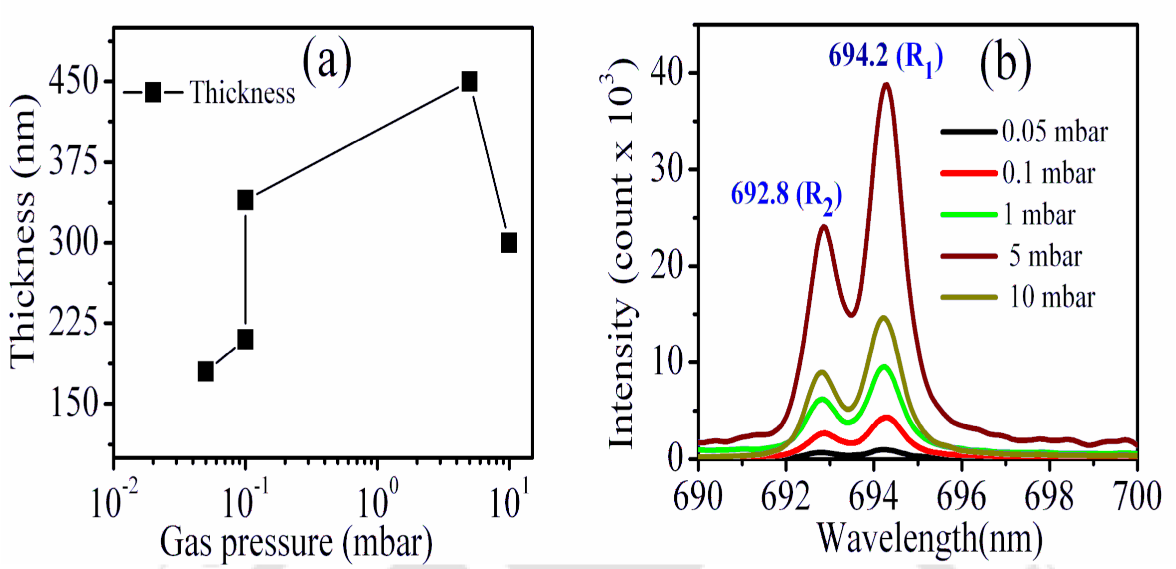

Figure 4.11 *Effect of background gas pressure on (a) thickness and (b) photoluminescence.*

The PL spectra as shown in figure 4.11 (b), shows increase in PL intensity upto ~ 5 mbar and then drastic fall at ~ 10 mbar. Figure 4.12 shows the AFM micrographs of ruby films grown under various oxygen pressures. With increase in oxygen pressure from ~ 0.05 mbar to ~ 10 mbar, the surface roughness was found to increase from 2.00 nm to 5.90 nm. Whereas, the grain size was found to increase from 55.50 nm to 120.00 nm, with increase in gas pressure as observed from table 4.IV. Initially with the increase in gas pressure from ~ 0.05 mbar to ~ 5 mbar, expansion of plasma plume is confined. The loss of plasma species due to scattering is reduced. The accumulated effect is increase in plasma density and hence the thickness of the film increases as observed from figure 4.11 (a). The increase in PL intensity is also in accordance with the thickness. With further increase in the pressure to ~ 10 mbar the plasma is over confined in a very small region as well as due to increase in collisions [**198**], forward movement of the plasma towards the substrate is curtailed leading to the decrease in deposition rate, table 4.IV. Thus, the thickness as well as PL intensity was reduced at ~ 10 mbar, as observed from figure 4.11. Therefore, it can be concluded that the optimum oxygen pressure was ~ 5 mbar for deposition of ruby thin film via PLD technique.

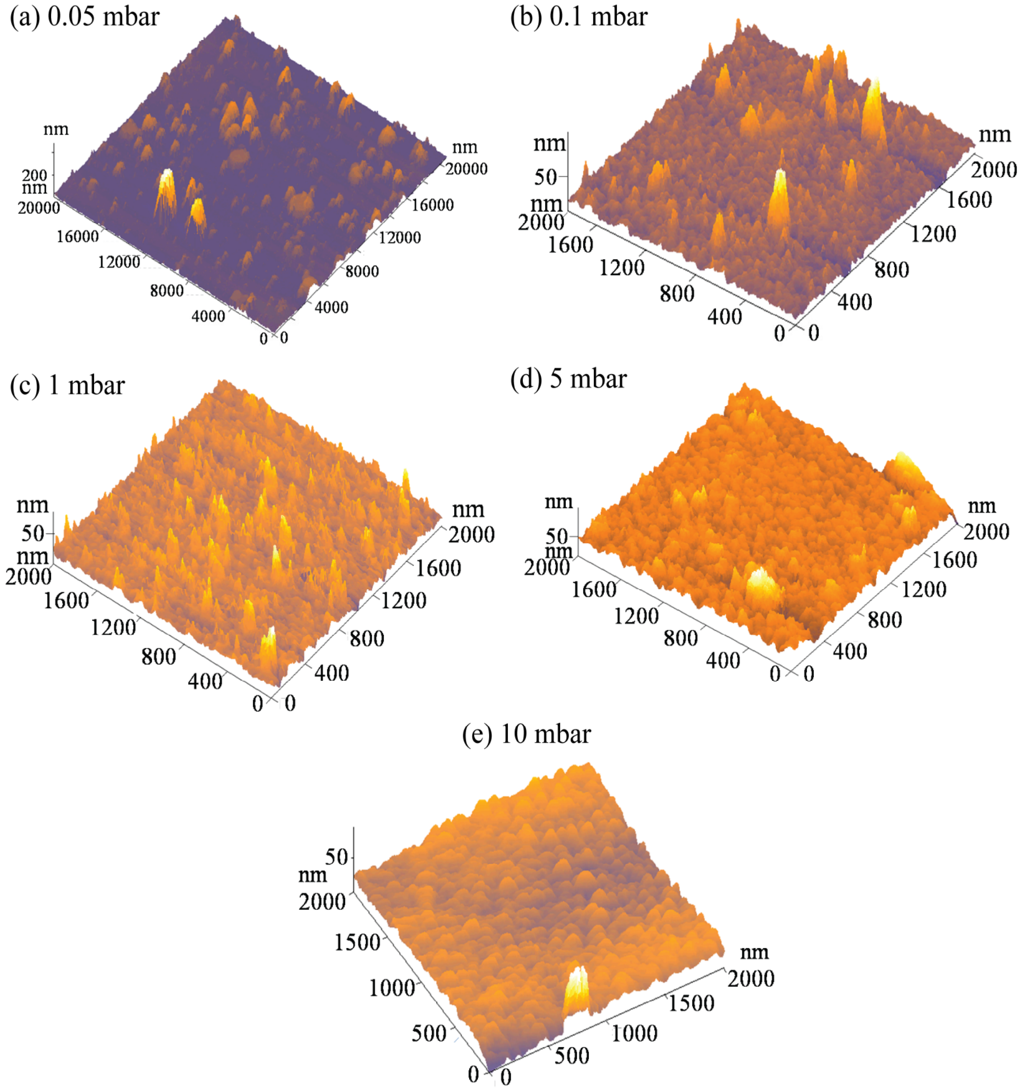

Figure 4.12 *AFM images of PLD ruby thin film at various gas pressures.*

4.3.4 Effect of deposition time on PLD Ruby thin films

Table 4.V lists the details of PLD deposited thin films of ruby as a function of deposition time at optimum laser fluence of ~ 23 J/cm^2 and at a pressure of ~ 0.05 mbar, keeping the substrate temperature at 750°C fixed on quartz substrate. The thickness of the film was

Table 4.V: *List of PLD ruby thin films deposited at various deposition time.*

Sample no	**Deposition time (hrs)**	**Gas pressure (mbar)**	**Laser fluence (J/cm^2)**	**Thickness (nm)**	**Deposition Rate (nm/min)**
Sample 23	0.5	0.05	23.0	70	2.30
Sample 24	1	0.05	23.0	178	2.90
Sample 25	2	0.05	23.0	360	3.0 0
Sample 26	3	0.05	23.0	550	3.05
Sample 27	4	0.05	23.0	1030	4.29
Sample 28	6	0.05	23.0	1830	5.08

found to increase from 70 nm to 1830 nm on increasing the deposition time from 30 min to 6 hrs as shown in figure 4.13 (a). The corresponding deposition rate was found to improve from 2.30 nm/min to 5.08 nm/min as observed from table 4.V. The photoluminescence spectra of films are shown in figure 4.13 (b). The PL intensity was found to increase with increase in deposition time. The observed behavior can be attributed to improvement in the uniformity and crystallinity of the deposited film with increase in deposition time. With

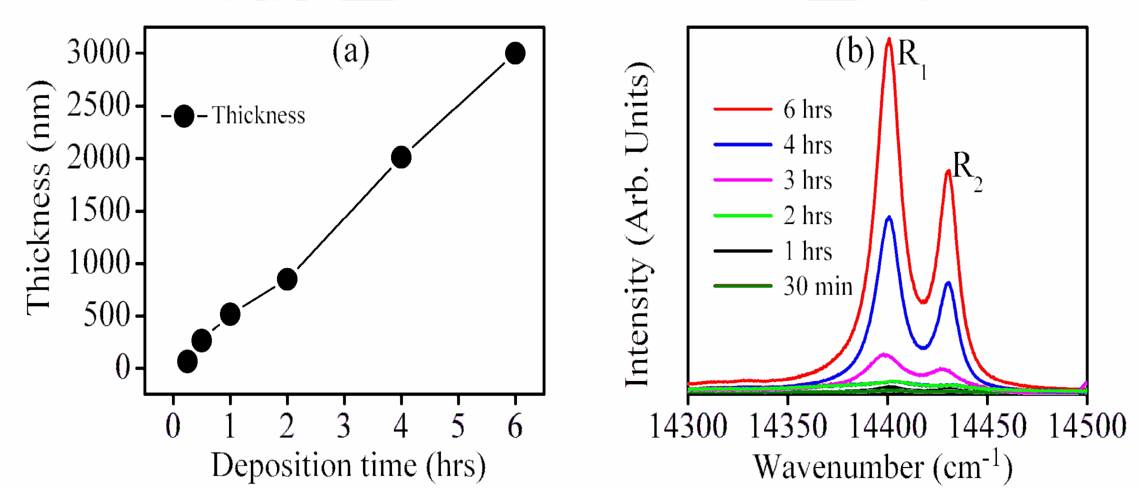

Figure 4.13 *Effect of deposition time on (a) thickness and (b) PL of PLD ruby thin film.*

increase in deposition time the number of layers and the nucleation sites increases, leading to better growth of film on substrate.

4.4 Deposition of epitaxial Ruby thin film using optimized deposition conditions

Finally, epitaxial ruby thin film was deposited on double sided polished sapphire substrate using the optimized parameters of PLD. The details of experimental conditions are listed in table 4.VI. The thickness of the deposited film estimated using stylus profilometer was ~ 3500 nm. The Raman spectrum of this film is shown in figure 4.14.

Table 4.VI: *List of deposition parameters at which epitaxial ruby thin film was deposited.*

Sample no:	**Substrate**	**Deposition time (hrs)**	**Gas pressure (mbar)**	**Laser fluence (J/cm^2)**	**Post Annealing**	**Thickness (nm)**	**Deposition Rate (nm/min)**
Sample 29	Both sided polished sapphire	6	5	23	1000˚C for 2 hrs.	3500	9.72

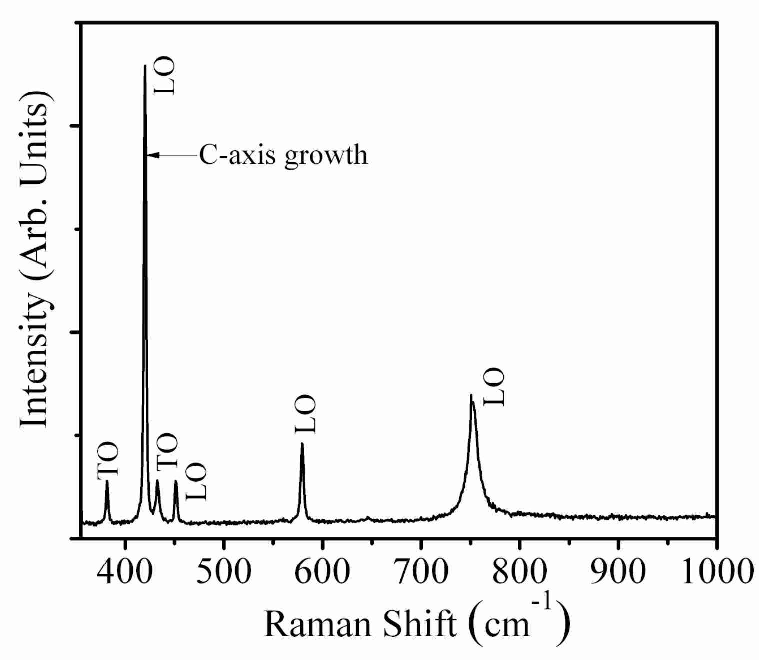

Figure 4.14 *Raman spectra of epitaxial ruby thin film.*

All the vibrational bands, as shown in figure 4.14, correspond to the C-plane of sapphire [**203- 205**]. The Raman bands were fitted to Lorentzian fit and peak positions & FWHM are enlisted in table 4.VII. The sharp bands confirm very high quality of deposited ruby thin film. There is no appreciable shift in the peak position of Raman bands as compared to the C-plane of sapphire [**203- 205**]. The FWHM of all the bands are found to be narrow than that of sample 11 deposited on sapphire substrate, table 4.II. The PL spectrum of this film is shown in figure 4.15.

Table 4.VII: *List of peak position and FWHM of various Raman bands of epitaxial ruby thin film, sample 29.*

Raman band	**TO**	**LO**	**TO**	**LO**	**LO**	**LO**
Peak position (cm^{-1})	379.04	418.08	430.17	450.03	575.17	750.02
FWHM (cm^{-1})	2.26	2.24	3.35	2.44	3.02	11.55

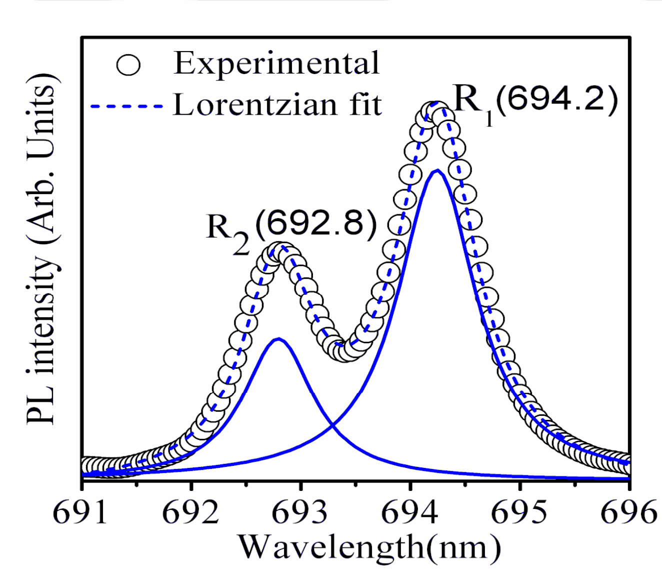

Figure 4.15 *PL spectra of epitaxial ruby thin film on sapphire substrate (sample 29).*

The sharp R-line fluorescence confirms ruby phase in the film. The spectra was very well fitted to double Lorentzian line shape with coefficient of determination r^2 ~ 0.999. The R-line width was found to be ~ 11.7 cm^{-1} which was comparable to 11.6 cm^{-1} line width in case of ruby crystal [**2**]. The ruby film grown via solid phase epitaxy was observed to have a line width of 15.8 cm^{-1} [**128**], higher than that of PLD deposited thin film of present experiment. Also, the ratio of Gaussian to Lorentzian width was ~ 0.04 which is smaller than the samples shown in figure 4.7. Thus, the deposited film is highly crystalline & stress free in nature.

4.5 Optical nonlinearity in epitaxial Ruby thin film via Z-scan technique

The nonlinear absorption coefficient (β) and nonlinear refractive index (n_2) of the deposited film was measured using Z–scan technique described in section 2.5 and figure 2.7 & 2.8. Best quality thin film, sample 29, having thickness ~ 3500 nm was subjected to open and closed aperture Z-scan studies. For reference, initially Z-scan of sapphire substrate was

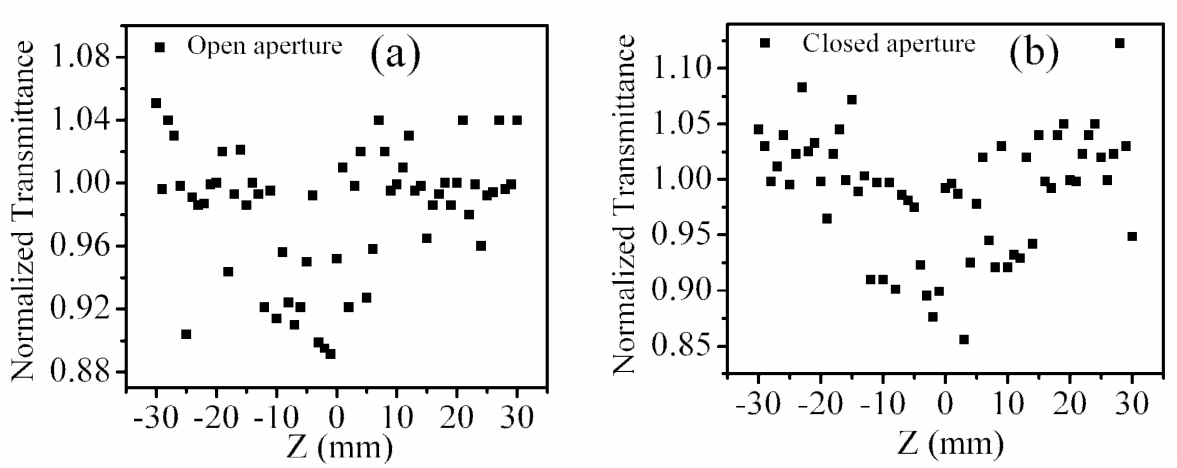

Figure 4.16 *Z-scan plot of the sapphire substrate (a) open aperture and (b) close aperture.*

performed as shown in figure 4.16 (a) & (b). The open and closed aperture Z-scan signal from the ruby thin film was recorded and the signal from substrate was subtracted from it and then normalized as described in section 2.5, chapter 2. The normalized open and closed Z-scan spectra of epitaxial ruby film is shown in figure. 4.17 (a) & (b), respectively. The open and closed spectra were fitted by using equation 2.4 and 2.8 (chapter 2) respectively.

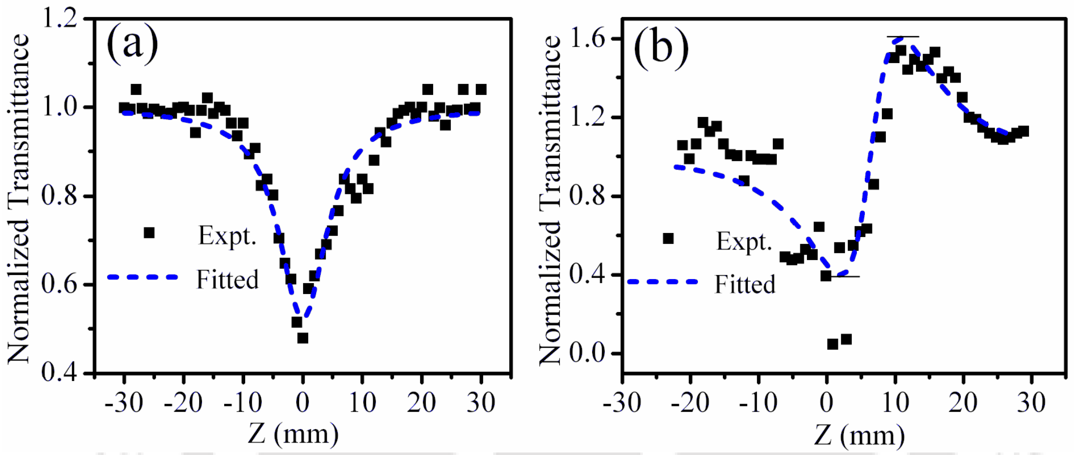

Figure 4.17 *Z-scan plot of the ruby film (a) open aperture and (b) close aperture.*

The nonlinear absorption coefficient estimated from the fitting of open aperture Z–scan signal of figure 4.17 (a) was found to be β ~ 5.2 $\times 10^{-5}$ m/W. The shape of the closed aperture Z–scan signal as shown in figure 4.17 (b) shows valley, followed by peak confirming positive value for the nonlinear refractive index. This suggests that the sample acts as a self focusing medium. The focusing of laser beam takes place before focus (z = 0) inside the film and consequently the beam divergence increases and the corresponding transmitted intensity reduces, resulting in a valley. Later, the peak comes when the sample passes through the diverging region of Gaussian beam and focuses the beam due to its self focusing action and thus increasing the transmission from the sample. The fitting of closed aperture Z–scan data to theoretical fit using equation (2.8) yields the value of $n_2 \sim 3.1 \times 10^{-5}$ m^2/W. The obtained value is three orders of magnitude larger than that of ruby crystal [**31**]. It has been observed earlier also that the NLO coefficients enhances in the thin film geometry as compared to their bulk counterpart [**209 - 210**].

Conclusion

A large number of ruby thin film samples were deposited on quartz & sapphire substrates using PLD technique to obtain the optimized parameters. The effect of substrate heating, laser fluence, gas pressure and deposition time, on quality of PLD thin films was studied. Films grown at higher substrate temperature were found to be thick and the PL intensity was also higher as compared to that of the film grown at lower substrate temperature. On increasing the laser fluence, the quality of film was found to initially improve due to formation of highly energetic particles. On further increasing the laser fluence, the film quality was deteriorated due to sputtering from the film surface on impingement of highly energetic species from the laser produced plasma of ruby. The thickness of the ruby films was found to increase with the increase in background oxygen pressure due to increase in plasma density upto ~ 5 mbar. Beyond ~ 5 mbar oxygen pressure, the thickness was found to decrease due to plasma confinement. The thickness was found to increase with increase in deposition time. The deposited films under various experimental conditions were annealed at 1000°C for 2 hrs. The PL intensity of all the annealed samples shows multifold enhancement, as compared to that of as deposited samples. The optimized growth conditions; laser fluence ~ 23 J/cm^2, background gas pressure ~ 5 mbar and substrate temperature of 750°C, were used to deposit epitaxial ruby thin films on both side polished sapphire substrate. This film was deposited for 6 hrs to obtain a thickness of ~ 3500 nm. The deposited film was found to be highly C-axis oriented and stress free as confirmed by FWHM of R_1, R_2 line of 11.7 cm^{-1}. The Z-scan data confirms the 3 orders of magnitude enhanced optical nonlinearity in epitaxial ruby thin film compared to that of reported bulk crystal [**31**].

Chapter 5

Pulsed laser deposition and characterization of Barium titanate thin films

High quality barium titanate (BTO) crystal/thin films are finding various applications in the field of photonics due to its remarkable nonlinear optics (NLO) properties [**43-47, 50-52**]. It has very high value of electro-optic coefficients, fast response time and excellent phase conjugate reflectivity [**47-50**]. It exhibits slow and fast light, two-wave mixing, four-wave mixing, second harmonic generation, at room temperature [**45, 46, 48, 211-213**]. Also, BTO shows temperature dependent phase transition from low temperature rhombohedral to high temperature cubic phase along with room temperature tetragonal phase from 280 K to 395 K. The effect of temperature is clearly evident from the Raman bands of BTO [**53-55**], making it suitable for Raman temperature sensor. For the device applications, high quality tetragonal BTO thin film is desirable. In the present work, PLD technique has been used for the deposition of barium titanate thin film using sintered BTO pellet as a target, for optical delay studies and temperature sensing applications. The optical delay of light depends upon the effective length of the medium, hence in the present work, 3300 nm thick BTO film was fabricated via PLD technique for a deposition time of 6 hrs at optimized deposition parameters as reported in the literature [**132-141**].

5.1 Experimental Details

Barium titanate thin films were prepared via PLD technique using barium titanate pellet as target. The pellet used as target for deposition was obtained by sintering the pressed powder of barium titanate at 1400˚C for 2 hrs. The experimental setup for film growth via PLD is described in section 2.2, figure 2.2, in chapter 2. The PLD film of BTO was deposited at a laser fluence of ~ 10 J/cm^2, substrate to target distance 4 cm, oxygen pressure at ~ 0.1 mbar and substrate temperature 750°C. All the films were deposited on quartz substrate. The six samples of BTO thin films were prepared by varying the deposition time; 30 min, 1 hr, 2 hrs, 3 hrs, 4 hrs and 6 hrs as enlisted in Table 5.I. These films were post annealed at 1000°C for 2 hrs. The as deposited as well as post annealed BTO films were subjected to XRD, Raman & UV-Visible studies for structural and optical characterizations.

Table 5.I: *List of PLD BTO thin films deposited as a function of deposition time.*

Sample no:	**BTO 1**	**BTO 2**	**BTO 3**	**BTO 4**	**BTO 5**	**BTO 6**
Deposition time	30 min	1 hr	2 hrs	3 hrs	4 hrs	6 hrs
Thickness	62 nm	275 nm	510 nm	820 nm	1980 nm	3300 nm
Band gap	3.41 eV	3.40 eV	3.38 eV	3.42 eV	3.43 eV	3.42 eV

5.2 UV –Visible Spectra of post annealed PLD BTO thin films

The UV-Visible spectra of all the post annealed samples, as shown in figure 5.1 shows clear interference fringes. The presence of fringes confirms the uniformity of the deposited BTO film. On increasing the deposition time the fringes has been found to be more closely spaced confirming the increase in thickness with the increase in deposition time. The thickness of the PLD deposited BTO film was estimated from UV-Visible spectra using envelope approximation [**193**]. The typical envelope approximation for the sample BTO 5 is shown in figure 5.1(b). The estimated thickness of all the samples is listed in Table-5.I.

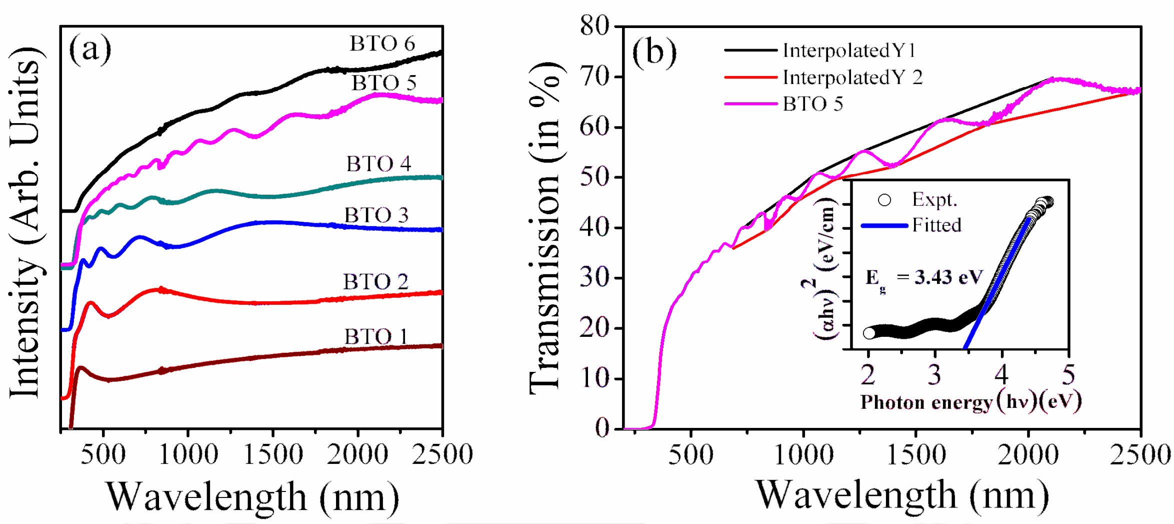

Figure 5.1 *(a) UV-Visible spectra of post annealed films. (b) Envelope approximation of sample BTO 5 for finding band gap and thickness inset shows the estimation of band gap from hυ vs* $(\alpha h\upsilon)^2$ *curve.*

The film thickness increases from 62 nm for 30 minutes deposition time to 3300 nm for 6 hrs deposition, as shown in figure 5.2. The increase in film thickness with increase in

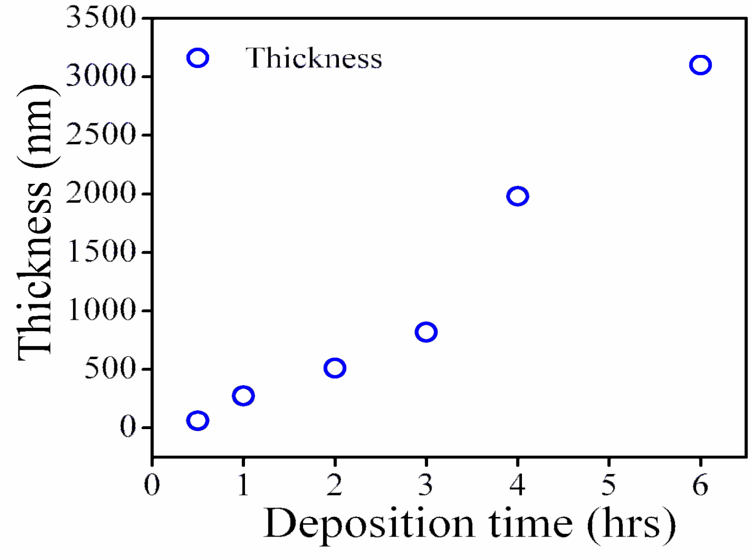

Figure 5.2 *Thickness of PLD BTO thin film as a function of deposition time.*

the deposition time is due to the impingement of more and more ablated target material on substrate surface. The inset of figure 5.1(b) shows the plot of $(\alpha h\upsilon)^2$ vs $h\upsilon$ for BTO 5, where α is the absorption coefficient of the BTO film. The refractive index of BTO film obtained from UV-Visible spectra was in the range of 2.488 to 2.410 over a wavelength range of 200 to 700 nm. These values are in agreement with the refractive index of barium titanate crystal. The band gap, estimated from linear fit of the curve as shown in Figure 5.1(b), was found to be ~ 3.4 eV, which is again in agreement with that of bulk BTO [**50**].

5.3 XRD measurement of PLD BTO thin films

Figure 5.3 (a) & (b) shows the XRD patterns of as deposited and post annealed PLD thin film samples of BTO respectively.

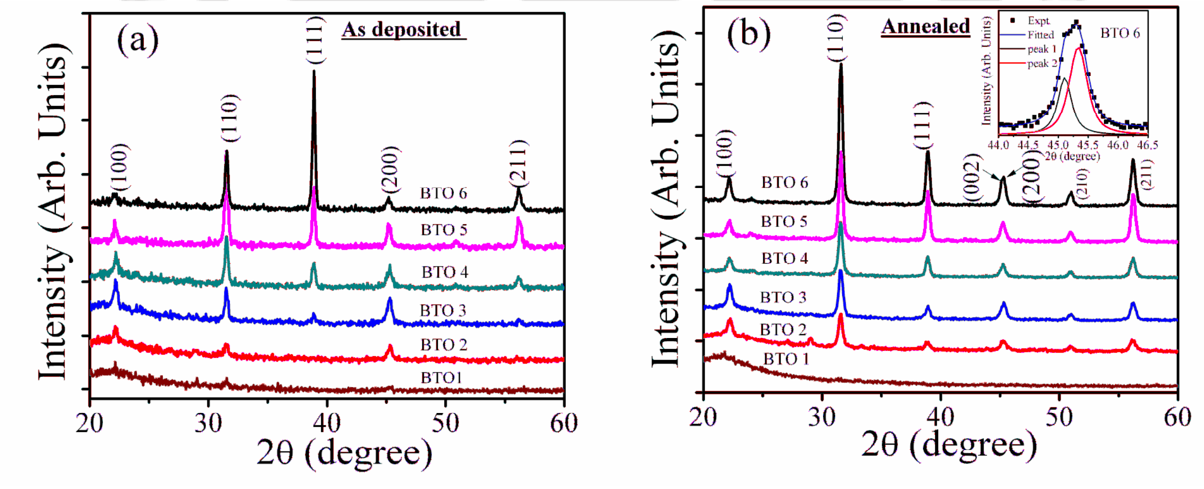

***Figure 5.3** XRD spectra of PLD $BaTiO_3$ films (a) as deposited and (b) post annealed at $1000^{\circ}C$ for 2 hrs.*

Five distinct peaks in XRD corresponding to (100), (110), (111), (200) and (211) planes of BTO were identified [**214-216**]. The intensity of all the XRD peaks increases with the deposition time. The thickness of the films increases with the deposition time therefore, the XRD peaks are enhanced with increase in deposition time as shown in figure 5.3 (a). The XRD spectra of post annealed films are shown in figure 5.3 (b).

The inset in figure 5.3 (b) for sample BTO 6 shows the twin peaks corresponding to (002) and (200) plane, confirms formation of tetragonal phase of BTO [**217**] in the post annealed samples. The variation of peak intensity of (110) plane and corresponding FWHM as a function of deposition time is shown in figure 5.4 (a) & (b) respectively for as deposited as well as post annealed film. With increase in deposition time from 1 hr to 6 hrs, the intensity of XRD peak of (110) plane in post annealed film scaled drastically as observed from figure 5.4 (a). The corresponding FWHM was found to reduce with increase in deposition time for both the as deposited as well as post annealed samples as observed from figure 5.4 (b). This confirms the improvement in crystallinity upon annealing and with the increase in thickness.

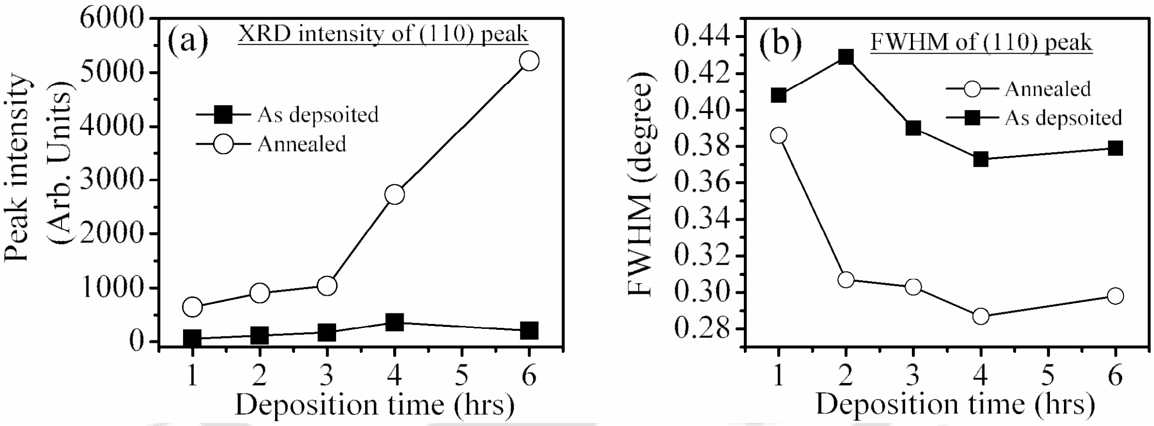

Figure 5.4 *(a) Peak intensity and (b) FWHM of (110) peak for as deposited as well as post annealed BTO film.*

5.4 Raman spectra of PLD BTO thin film

Due to the poor resolution of the XRD the observation on the tetragonal phase of BTO was not very convincing. Therefore, Raman spectra of all the films were recorded. Figure 5.5 (a) shows the Raman bands of as deposited BTO thin films for various deposition times. It can be seen from the figure 5.5 (a) that with the increase in deposition time the peak intensity for all the bands undergoes enhancement. The 308 cm^{-1} E (TO+LO) band called the B1 band, corresponding to the tetragonal phase [**54, 55**], is observed at 300 cm^{-1} in case of as deposited BTO 4 and it becomes prominent in BTO 5 and BTO 6. A lower Raman shift of B1 peak indicates presence of elongation strain in the lattice and its large FWHM indicates poor crystallinity for as grown films in agreement with XRD results. The other Raman bands observed were at 128, 148, 183, 519 and 675 cm^{-1}. The 185 cm^{-1} band corresponds to E (TO)/ E (LO)/ A1 (LO) mode of

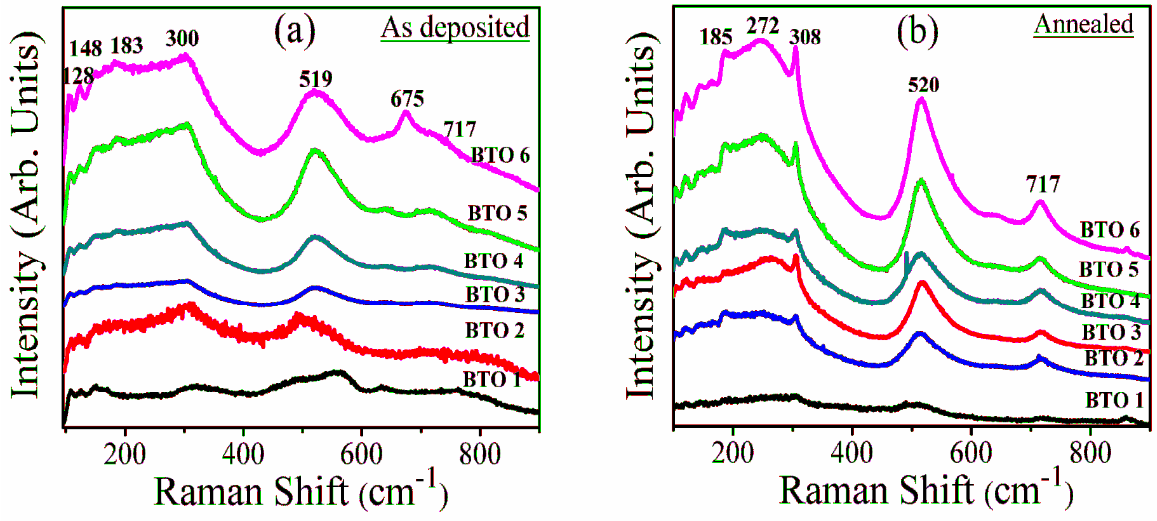

Figure 5.5 *(a) Raman spectra of as deposited $BaTiO_3$ films and (b) post annealed at 1000° C for 2 hrs.*

BTO. The 519 cm^{-1} corresponds to the onset of asymmetry in the E (TO), A1 (TO) mode [**54**, **218, 219**]. A hump at 717 cm^{-1} is also observed, which becomes obvious for films grown for higher deposition times, a characteristic signature of tetragonal phase of BTO [**54**]. The 675 cm^{-1} peak is the signature of hexagonal phase. This weak broad Raman feature corresponds to the A1 (LO) and E (LO) mode. The broad Raman spectral feature may also arise from disorders in the film. The BTO crystals are naturally found to be in tetragonal phase at room temperature [**218**] but due to presence of internal stress in the deposited film which may be developed due to lattice mismatch of the BTO film and quartz substrate, the deposited film was found to be in mixed phase of hexagonal and tetragonal. On increasing the deposition time, lattice strain present at the interface slowly decreases with increasing BTO layers and shows signature of tetragonal phase. The effect of post annealing on Raman bands can be observed from figure 5.5 (b). Upon annealing, the up-shift of 300 cm^{-1} peak to expected 308 cm^{-1} and comparatively sharper peak features can be attributed to release of stress from the deposited film. The 675 cm^{-1} band corresponding to the hexagonal phase was suppressed and the 717 cm^{-1} corresponding to the tetragonal phase distinctly emerged out in the post annealed samples.

5.5 Z-scan studies of PLD BTO film

The post annealed BTO film deposited for 6 hrs, sample BTO 6 of thickness ~ 3300 nm was subjected to Z-scan to measure the nonlinear optical parameters. The experimental setup of figure 2.9 and 2.10, (chapter 2) was used for open and closed aperture Z-scan measurement respectively. Figure 5.6 (a) and (b) shows the open and closed aperture Z-scan signal for quartz substrate respectively. Absence of systematic trend in the spectra confirms that there were no nonlinear processes occurring inside the bare quartz substrate.

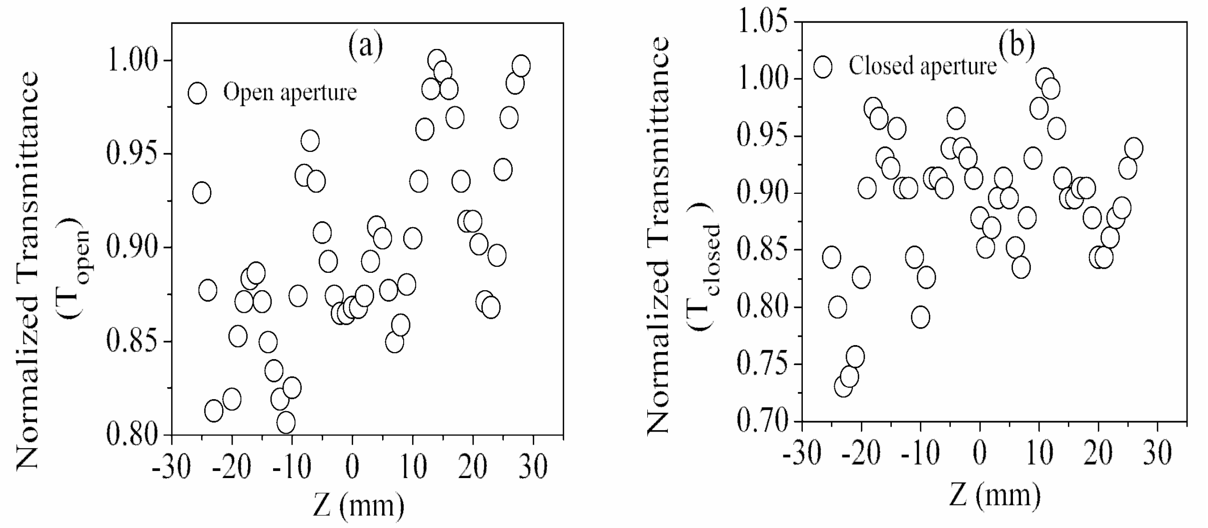

Figure 5.6: *(a) Open and (b) closed aperture Z-scan signal from quartz substrate.*

The Z-scan of quartz substrate was subtracted from the Z-scan of BTO 6 and then normalized. The normalized open aperture and closed aperture signals are shown in figure 5.7 (a) & (b.)

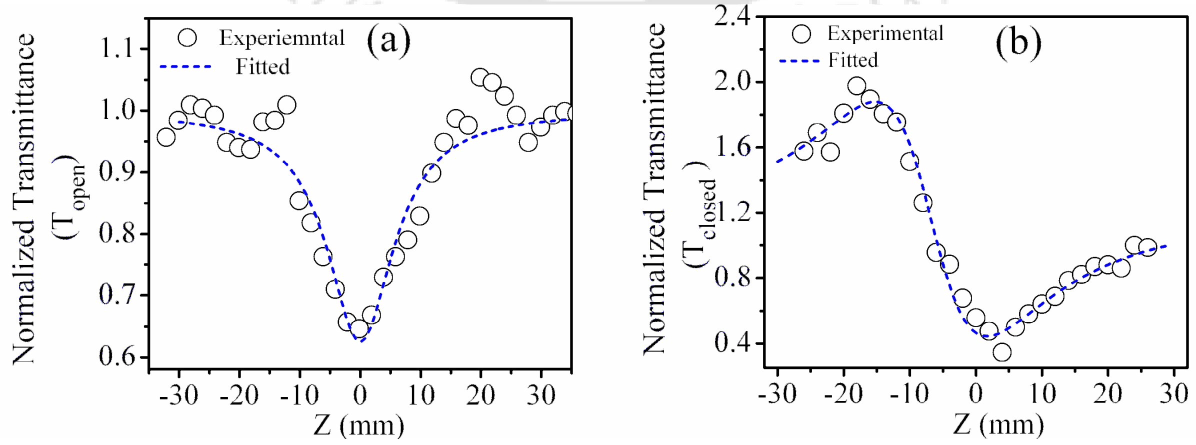

Figure 5.7 *(a) Open and (b) closed aperture Z-scan signal from PLD BTO thin film.*

The open and closed Z- scan spectra were fitted using equation 2.4 and 2.8 (Chapter 2). The nonlinear absorption coefficient estimated using the open aperture was found to be β ~ 8.6 × 10^{-7} m/W. The real and imaginary part of susceptibility was found to be $\chi^{(3}$(Re) ~ 7.5 × 10^{-7} esu and $\chi^{(3}$(Im) ~ 9.8 × 10^{-8} esu, from the closed Z-scan data. The estimated values are in agreement with the reported results [**50, 52**].

Conclusion

Barium titanate thin films have been deposited via pulsed laser deposition technique. The thickness of the films was found to increase with increase in deposition time. The post annealed films were found to possess tetragonal phase as confirmed from the XRD as well as Raman studies. The maximum thickness of 3300 nm of BTO thin films via PLD was obtained at optimized parameters and for a deposition time of 6 hrs. The band gap of the PLD BTO films ~ 3.4 eV was found to be comparable to that of bulk. The nonlinear absorption coefficient and susceptibility were measured using Z-scan technique.

Chapter 6

Optical delay of light in photorefractive Barium titanate crystal and PLD thin film

Optical delay of light at room temperature in solid state material has potential application in the field of communication and quantum computing [**40-42**]. Photorefractive (PR) barium titanate (BTO) has emerged as one of the most promising material for optical delay application at room temperature [**43-46**]. Recently, slow and fast light has been experimentally demonstrated in BTO crystal at room temperature via degenerate and non-degenerate two-wave mixing (pump-probe techniques). The optical delay in PR medium can be easily tuned by varying various experimental parameters [**45, 46, 48, 84, 85**]. Therefore, it can be used to make tunable all optical delay line. For coupling the technology of optical delay line in device, the medium should be miniaturized in the form of thin film.

In the present chapter, slowing down of light is demonstrated initially in barium titanate crystal. The effect of various input parameters; pulse width of signal beam, pump intensity, pump-probe polarization and crystal orientation is systematically studied. Later, the pulse propagation of light is investigated in PLD deposited tetragonal thin film of BTO.

6.1 Pulse propagation inside Ce:BaTiO$_3$ crystal

The experimental setup, figure 2.16, used to study the pulse propagation inside Ce:BaTiO$_3$ crystal of dimension 5 mm × 5 mm × 7 mm, via degenerate two-wave mixing using millisecond chopped pulses of a CW He:Ne laser (632.8 nm) is discussed in section 2.6.2.1, chapter 2. The effect of various experimental parameters onto the delay in transmitted signal pulse is reported in the following sub sections.

6.1.1 Effect of pulse width on optical delay

The effect of signal pulse width onto optical delay has been studied by varying the pulse width from 2 ms to 20 ms. The DSO traces of the reference beam and the signal beam of pulse width of 8 ms is shown in the figure 6.1 (a), for pump intensity (I_p) of ~ 1.2 W/cm^2 & signal intensity (I_s) ~ 0.45 W/cm^2. In the presence of pump beam, a time delay (Δt) of 0.9 ms was observed, corresponding to an ultraslow light of Group velocity υ_g ~ 5.5 m/s. The observed delay can be accounted for the photorefractive (PR) two-wave mixing [**86-88**]. The variation of delay as a function of signal pulse width is shown in figure 6.1 (b). The time delay (Δt) initially increases with increase in the pulse width and this is because the photorefractive phase coupling is more effective with longer pulse duration, especially when the pulse duration is much less than the response time of the coupling process, but it finally saturates when the pulse duration is comparable or much longer than the response time of the medium [**43**]. When the pump and signal beams were coupled inside a crystal, the intensity modulation results in the redistribution of charge carriers via diffusion. The spatially varying charge distribution density ρ(x) gives rise to the linear electro-optic effect resulting in the formation of refractive index grating [**197**]. The time required to write a refractive index grating depends on the efficiency of charge generation and transport mechanism [**48**]. This charge migration time, also known as response time of the crystal, is proportional to the light intensity. The refractive index grating, thus formed, diffracts the energy from the pump beam to the signal beam.

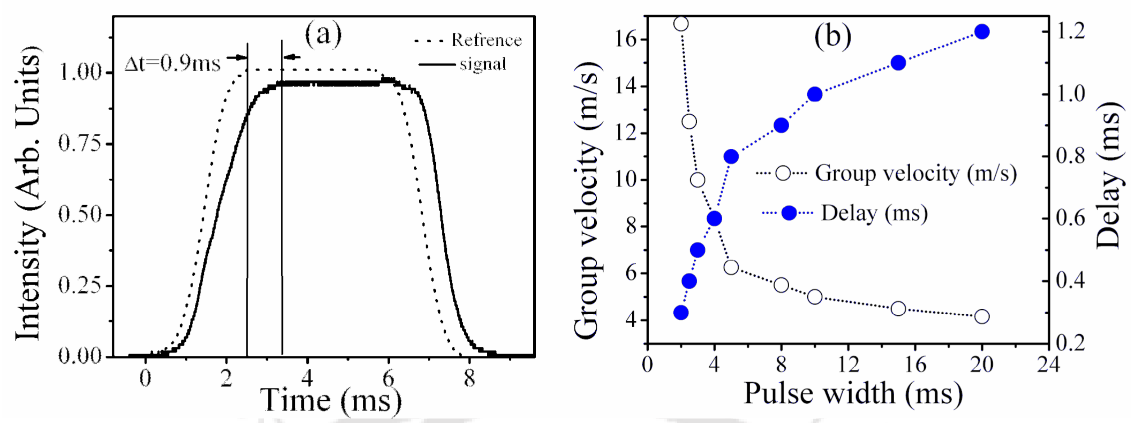

Figure 6.1 *(a) oscilloscope traces of the reference pulses (dashed curve) and the transmitted signal pulses (solid curve) at pump intensity,* I_p*=1.2 W/cm*^{2}*. Signal intensity,* I_s*= 0.45 W/cm*^{2}*. (b) Variation of time delay and group velocity onto the pulse width for* I_p*= 1.2 W/cm*^{2}*,* I_s*= 0.45 W/cm*^{2}*.*

The transmitted signal pulse was observed to amplify with time and then it was stabilized and finally reshaped. This amplification and reshaping is coming due to unidirectional transfer of energy from pump to the signal beam via Bragg diffraction from the index grating. The grating building up time as a function of pump intensity was recorded by setting the chopper frequency at 10 Hz and then recording the transmitted signal for longer time at various pump intensities. The corresponding grating decay time was measured by blocking the pump beam after stabilization of PR grating and then recording the transmitted signal again for a very large duration. Figure 6.2 (a) and 6.2 (b) shows the development and decay of grating respectively for pump intensity of ~ 1.2 W/cm^2. The grating formation and decay in the present study is via transient two-wave mixing and corresponding building up and decay times are calculated in the real time [**220**].

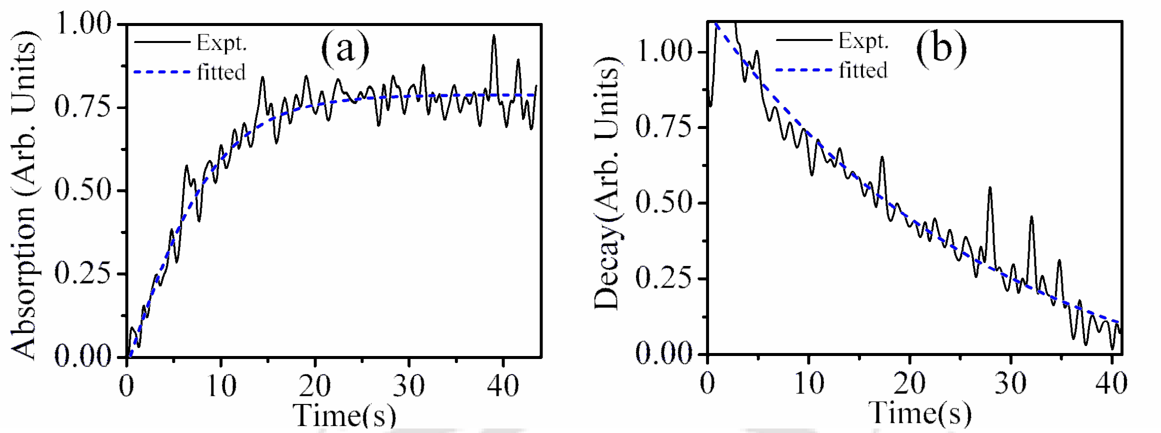

***Figure 6.2** (a) Growth of grating at maximum pump intensity (b) corresponding decay.*

The grating building up and decay time was attended by fitting the temporal traces with equation 6.1 and 6.2, as shown in the figure 6.2 (a) and 6.2 (b) respectively by broken line.

$$\sqrt{I_b} = \sqrt{I_b^{\,O}}\ [1 - \exp(-t/\tau_1)] \tag{6.1}$$

$$\sqrt{I_d} = \sqrt{I_d^{\,O}}\ [\exp(-t/\tau_2)] \tag{6.2}$$

Where, I_b is the transmitted signal intensity, at any time t, during grating building up, $I_b^{\,O}$ is that of maximum intensity obtained after completion of the grating build-up process, under steady state [$I_b^{\,O} = I_b$(t >> τ_1)]. I_d is the intensity at any time t during grating decay. I_d^O is the maximum intensity obtained under the steady state condition after completion of the grating build-up process (or just before switching the pump off, $I_d^{\,O} \approx I_b^{\,O}$). τ_1 and τ_2 are the grating building up and decay time respectively. For maximum pump intensity, the building up time (τ_1) is found to be approximately 9.6 seconds and corresponding decay time (τ_2) is 29.8 seconds. The time required for building up of grating in the present experiment is much larger than the time period of chopped pulse (16 ms). The grating was allowed to build-up in the crystal with a large number of pulses till the grating was stabilized. The transmitted signal pulse shown in figure 6.1 (a) was recorded after stabilization of the grating. The grating erasure rate depends on the intensity and dielectric relaxation time. At higher intensity ~ MW/cm^2, the grating erasure is fast but for smaller intensity ~ W/cm^2 range, it is slow [**221**]. In the dark region of signal pulses, the erasing process for the grating is negligible in the present case as the dark region (8 ms) is much less than the grating's decay time of 29.8 second as shown in figure 6.2 (b). Hence, during the grating build-up, the grating will continue to persist in the dark part of the signal. Moreover, the dielectric relaxation of 0.2 second for $BaTiO_3$ [**222**] crystal is also large compared to the dark region of the present experiment, further ensuring that grating will persist in the dark region of the square pulses having time period of 16 ms. The grating building up time as a function of pump intensity is plotted in figure 6.3 and is fitted to $1/(I_p+I_s)$ [**43**].

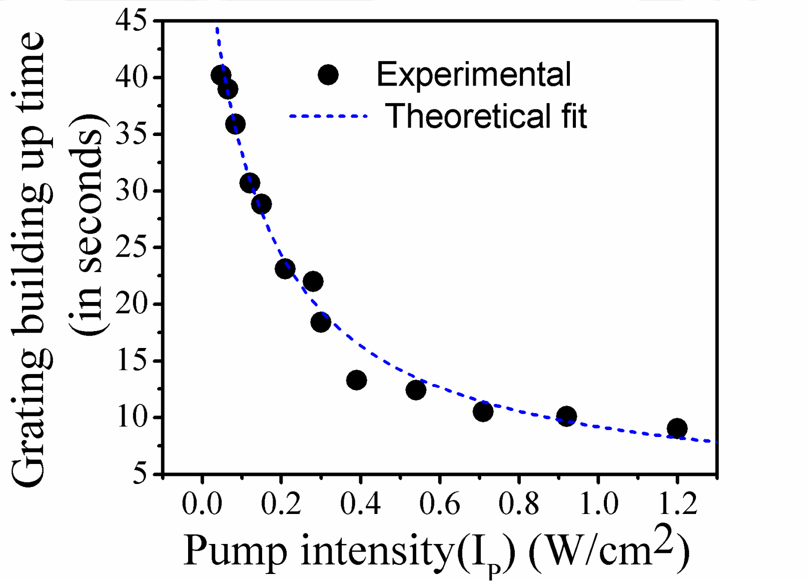

Figure 6.3 *Grating building up time as a function of pump intensity.*

The reciprocal dependence of build-up time with the pump intensity I_p, particularly at higher pump intensities ($I_p >> I_s$) is because at higher pump intensities the charge generation and transport via diffusion is fast. As a result, grating formation is fast and hence pump and signal beam are coupled via Bragg diffraction from the index grating in a very small time. At low intensities, the grating building up process is slow due to poor efficiency of diffusion of charge carriers.

6.1.2 Effect of pump intensity on optical delay

The effect of pump intensity onto the transmitted signal pulse was observed experimentally by varying the pump intensity from ~ 0.92 W/cm^2 to ~ 0.048 W/cm^2. The signal intensity was maintained at I_s ~ 0.45 kW/cm^2 throughout the experiment. Figure 6.4 shows the DSO traces of transmitted signal pulses for various pump intensities.

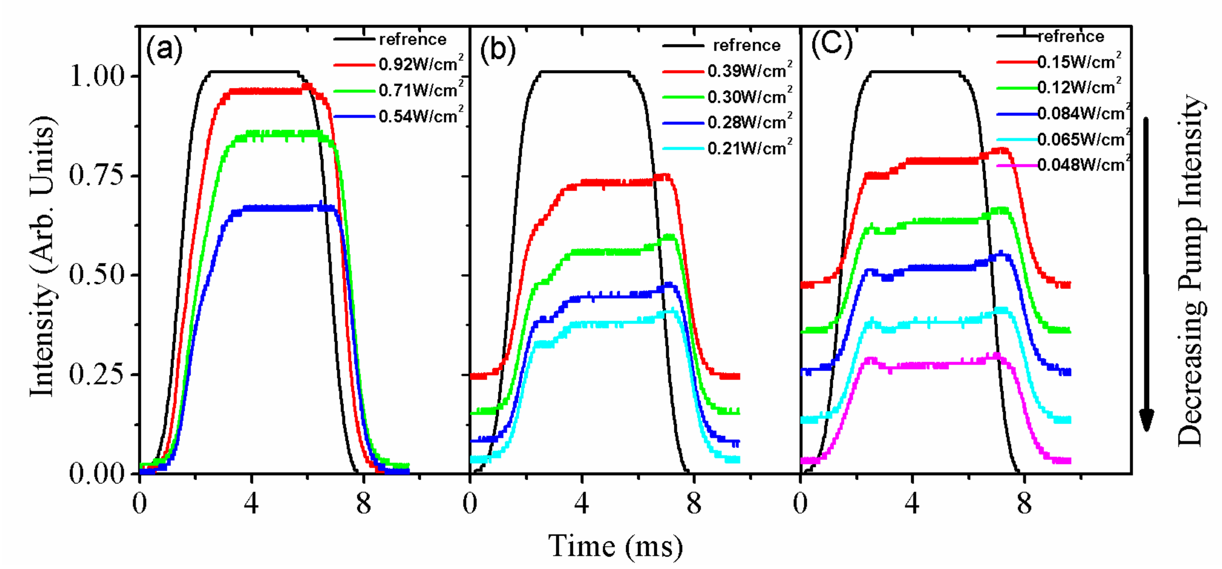

***Figure 6.4** Effect of pump intensity on pulse profile of transmitted pulse. (a) Pump intensity >signal. (b) shows the condition when pump and signal intensities are comparable. (c) Pump intensity < signal.*

It can be seen from figure 6.1 (a) & 6.4 (a) that when pump intensity, I_p = 1.2, 0.92, 0.71 and 0.54 W/cm^2 is more than the signal, the signal pulses are almost free from any distortion, due to unidirectional flow of energy from pump to the signal. The self-absorption inside the crystal is compensated by the PR two-wave mixing gain. Thus, there is a gain in the signal. Figure 6.5 (a) shows the plot of gain as a function of pump beam intensity. Gain was calculated from equation 1.1 (section 1.1.1.1, chapter 1), by

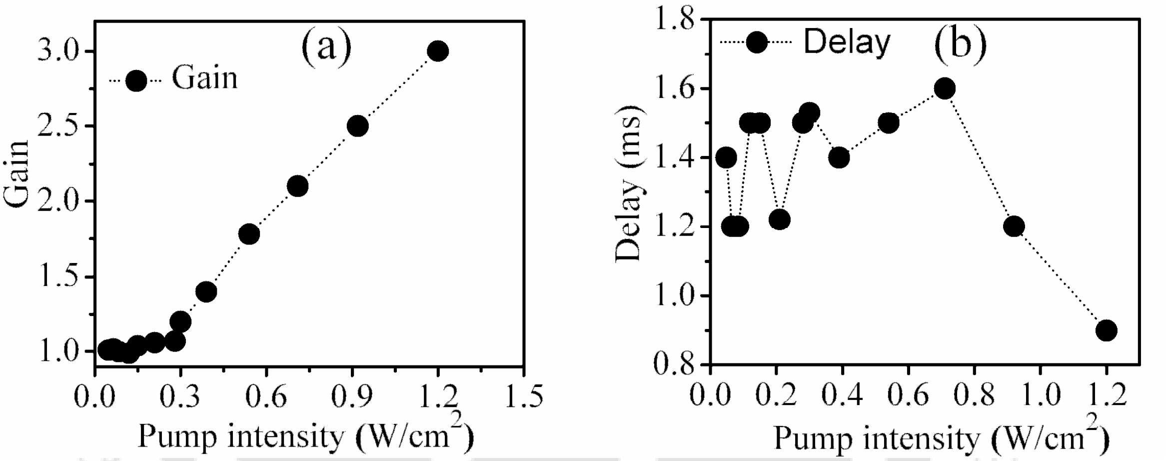

Figure 6.5 *(a) Variation of gain w.r.t. pump intensity (b) Variation of delay w.r.t. pump intensity.*

recording the transmitted signal beam intensity in pump on and pumps off conditions. At maximum pump intensity (~ 1.2 W/cm^2), measured value of the gain is ~ 3.0. In this case, the transmitted signal pulse is significantly delayed without undergoing any significant pulse distortion, figure 6.1 (a). With the decrease in pump intensity, the gain reduces almost linearly and the signal starts getting broadened and develops the distortion as shown in figure 6.4 (b) & (c). The pulse broadening and distortion effects are due to higher-order dispersion effects resulting from phase-coupling process. The slope of the phase coupling dispersion coefficient increases with decrease in intensity

[**87**]. It can be seen from figure 6.4 (b) & (c) that at low intensities, the distortion effects are more pronounced. The observed distortion in pulse shape at low pump intensities $I_p < I_s$, figure 6.4 (c), can be explained on the basis of transient energy transfer between pump and signal pulses back and forth during rising and trailing edges of the signal pulse. When pump intensity is reduced to a value almost comparable to the signal beam intensity, distortion in the form of dip can be seen in the rising edge of the transmitted signal pulse which is becoming pronounced as the pump intensity is further reduced as shown in figure 6.4 (b) and 6.4 (c). This is due to transfer of energy from the signal to the pump in the rising part of the pulse. The system tries to stabilize in the flat top region. In the falling edge, the transfer of energy takes place from the pump (as the pump intensity becomes higher compared to signal) and hence a hump at the beginning of the trailing edge is observed. Thus, there is a competition between the pump and the signal beam as the pump intensities are comparable and smaller than the signal. The effect of pump intensity onto the optical delay of light is plotted in figure 6.5 (b). It can be seen from the figure 6.5 (b) that in the range of ~ 0.7 W/cm^2 to ~ 1.2 W/cm^2, delay is inversely proportional to the pump intensity as reported earlier [**43**]. On reducing the intensity to much lower values than the signal, the observed delay is fluctuating with decreasing intensity. The observed fluctuations at low pump intensities can be explained on the basis of PR two-wave mixing gain. The gain is negligible at these pump intensities as shown in figure 6.5 (a) and hence the grating produced is of low index modulation and two-beam coupling is taking long time to stabilize and hence affecting the observed delay.

6.1.3 Effect of pump-signal polarization on transmitted signal

Ce:BaTiO$_3$ is a birefringent crystal. Therefore, its electro-optic coefficient and refractive index depends upon the direction of polarization of optical radiation and crystal orientation. The polarization of pump & signal beam is systematically varied by using a λ/2 plate in the path of both the beams as shown in figure 2.18 (chapter 2), for studying the effect of polarization on transmitted signal beam. The DSO traces of transmitted signal beam with respect to the reference beam for all four combinations of polarization states of pump and signal beam (S-S, P-P, S-P, P-S) are shown in figure 6.6 (the DSO traces are vertically translated for the sake of clarity).

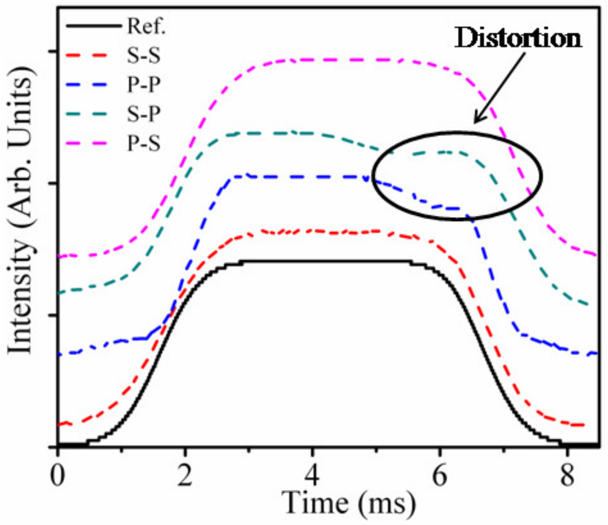

Polarization Sates Pump-signal	Pump polarization	Signal polarization
S-S	S	S
P-P	P	P
S-P	S	P
P-S	P	S

Figure 6.6 *Temporal traces of reference and transmitted signal pulse for various pump-probe combinations.*

The solid line indicates the reference pulse and broken line shows the output signal pulses. It can be seen from figure 6.6 that in case of S-S and P-S polarization states of pump and signal beam respectively that the transmitted signal beam is free from distortion. The gain from steady state two-wave mixing experiment using equation 1.1 (section 1.1.1.1, chapter 1) is ~ 3.0 and ~ 3.7 for S-S and P-S polarizations combinations of pump-signal respectively. The transmitted beam for S-P and P-P polarization states shows distortion and the corresponding gain is ~ 1.8 and ~ 1.6 respectively. Thus, maximum energy transfer is observed in P-S polarization case. The gain coefficients depend upon the effective electro-optic coefficients. The values of the electro-optic coefficients for $BaTiO_3$ crystal are r_{13} = 19.5 m/V, r_{33} = 97 m/V and r_{42} = 1640 m/V [**197**].

in case of S-polarized (ordinary) beam [**197**]

$$r_{eff} = r_{13}\, sin\frac{(\alpha_s + \alpha_p)}{2} \tag{6.3}$$

and that for P-polarized (extraordinary) beam [**197**]

$$r_{eff} = n^{-4}[n_o^4 r_{13}\cos\alpha_s \cos\alpha_p + 2n_e^2 n_o^2 r_{42}\cos\frac{1}{2}(\alpha_s+\alpha_p) + n_e^4 r_{33}\sin\alpha_s \sin\alpha_p]\ \sin\frac{1}{2}(\alpha_s+\alpha_p) \tag{6.4}$$

where, α_s & α_p denote the angle between the propagation vectors of the signal & pump beam & the positive direction of the crystalline C-axis respectively and n is the refractive index experienced by the beam that scatters off the grating. n_e & n_o, is the extraordinary and ordinary refractive index. In equation 6.4, the second term is dominating due to much larger value of r_{42} as compared to that of r_{13} or r_{33}. Thus, the effective electro-optic coefficient for S-polarized light is much smaller than that of P-polarized light. Hence, the grating is enhanced for P-polarized pump beam. Therefore, the observed gain in this case was maximum, as compared to all other combinations of pump-signal beam polarizations. However, in case of P-P polarization, although the electro-optic coefficient is large as compared to all other combination but due to beam fanning [**223**] the coupling is very poor and hence gain is minimal and the output transmitted beam is distorted, as shown in figure 6.6.

Thus, out of all four combinations of pump-signal, the transmitted signal beam in case of S-S & P-S polarization is free from distortion.

6.1.4 Effect of crystal orientation on optical delay

The effect of crystal orientation on optical delay is studied only in case of S-S and P-S polarizations as these combinations possess the large value of gain. The transmitted pulse at the two extreme ends of the crystal marked as +30° and -30° for S-S and P-S polarization is shown in figure 6.7.

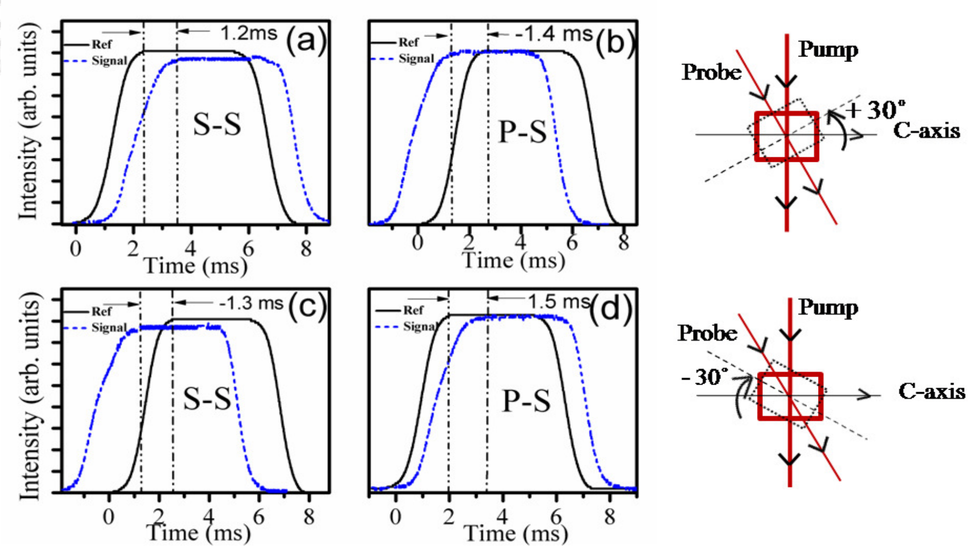

Figure 6.7 *Temporal traces of reference and transmitted signal (a) for +30° S-S polarization showing a delay of 1.2 ms (b) for +30° P-S polarization showing a pulse advancement of -1.4 ms (c) for -30° in case S-S polarization pulse advancement of -1.3 ms is observed. (d) For -30° P-S Polarization pulse delay of 1.5 ms observed.*

Figure 6.7 (a) and (b) shows the DSO traces of reference beam and signal beam at +30° orientation of crystal for S-S & P-S polarization states of pump-signal beam respectively. At +30°, for S-S polarization, a group delay of 1.2 ms is observed corresponding to slow light propagation with group velocity 4.1 m/s. For same crystal orientation for P-S polarization, pulse advancement of 1.4 ms is observed corresponding to a fast light of 3.5 m/s. Figure 6.7 (c) & (d) shows the reference and transmitted signal beam for -30° orientation of crystal. Pulse advancement of 1.3 ms is observed corresponding to a fast light propagation with velocity 3.8 m/s in case of S-S polarization. For P-S polarization, delay of 1.5 ms is observed corresponding to slow light propagation with group velocity 3.3 m/s. The effect of crystal orientation on temporal delay and group velocity is shown in figure 6.8.

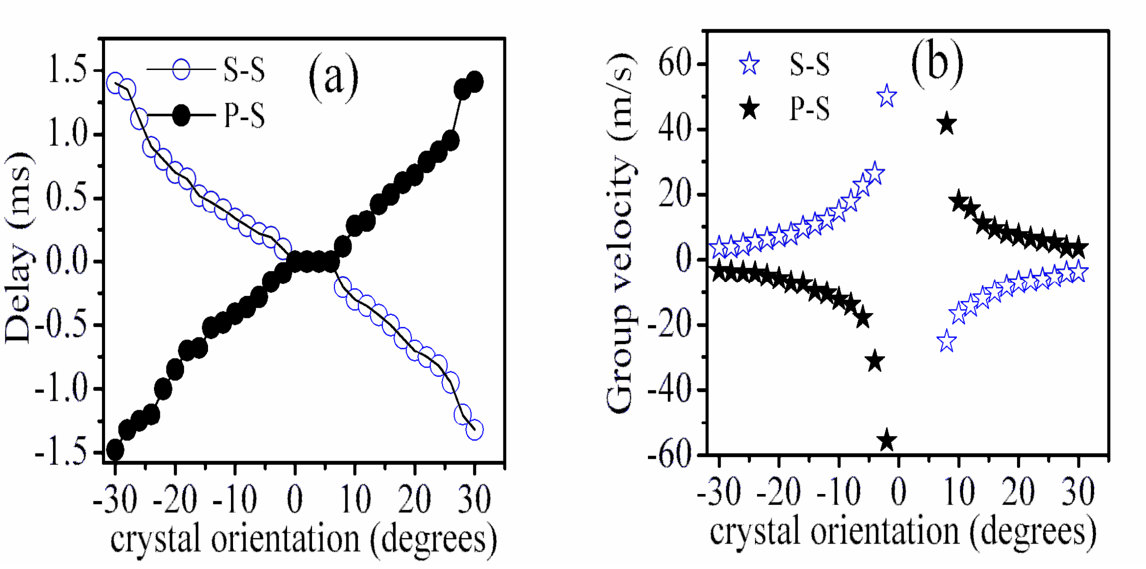

Figure 6.8 *(a) Delay and (b) group velocity as a function of crystal orientation.*

It can be observed from figure 6.8 (a) that when the crystal was orientated such that the pump beam is normal to the C-axis, no delay was observed. On rotating the crystal from

+30° to -30° the delay was switched from positive to negative value through zero. For any crystal orientation, if positive delay was observed in case of P-S polarization state then for S-S polarization negative delay was observed and vice-versa. This behaviour can be attributed to the dependence of phase shift on polarization states of pump and signal beaminside the photorefractive crystal. The observed delay in case of P-S polarization is slightly more as compared to S-S case because of larger gain in the former case. The calculated group velocity is shown figure 6.8 (b) as a function of crystal orientation. The slow and fast light observed can be explained on the basis of effective path length travelled by the beam inside the crystal and PR properties of medium. The effective group velocity inside PR crystal is given by equation 6.5 [**224, 225**].

$$v_g = v\frac{(\Delta k/2)^2 - \kappa^2 \cosh^2 sL}{(\Delta k/2)^2 - \kappa^2 \dfrac{\sinh sL}{sL}\cosh sL} \tag{6.5}$$

where, v is the group velocity of electromagnetic waves in the photorefractive medium in the absence of the refractive index grating, L is the length of grating, Δk is the phase mismatch factor which depends upon the angle of incidence and the photorefractive properties of the crystal and s is given by

$$s = [\kappa^2 - (\Delta k/2)^2]^{1/2} \tag{6.6}$$

and κ is the coupling constant given by

$$\kappa = \pi n_1/\lambda \tag{6.7}$$

where, n_1 is the index modulation of the volume-index grating. Thus, group velocity depends upon the phase mismatch and the coupling coefficient which in turn depend upon the orientation of the crystal along with the photorefractive indices. The phase mismatch depends upon the effective distance traversed by the signal beam inside the crystal. At the initial position of the crystal when pump beam was normal to the C-axis of crystal the effective path length was small and the coupling was also very poor, so no delay was observed as shown in figure 6.8 (a). On rotating the crystal from 0° to $\pm 30^{\circ}$, the delay/advancement was increasing due to increase in effective path length as well as better coupling of pump and signal beam.

6.2 Pulse propagation inside PLD Barium titanate thin film

The optical delay of light in PLD thin film of BTO was studied via degenerate two wave mixing using the setup of figure 2.19 (chapter 2, section 2.6.2.1). Pump and signal beams were derived from a 200 ns broad Nd:YAG laser pulse. The transmitted signal beam for films of various thicknesses (in pump off condition) is shown in figure 6.9. It can be observed from the figure 6.9 that the transmitted signal intensity decreases with increase in film thickness from 65 nm to 3300 nm (BTO 1- BTO 6). The maximum absorption is taking place in film of thickness ~ 3300 nm due to larger interaction length. Thus, this film was only subjected for the optical delay studies. This thin film of BTO was mounted on a rotating stage. Initially, the sample was placed normal to the pump beam, angle of incidence being 0°. This was the zero position of the film. The sample was rotated from 0° to $\pm 45^{\circ}$ and the transmitted signal was recorded in pump off and pump on conditions for all orientations in a step of 5°. The DSO traces for the reference and signal beam at an

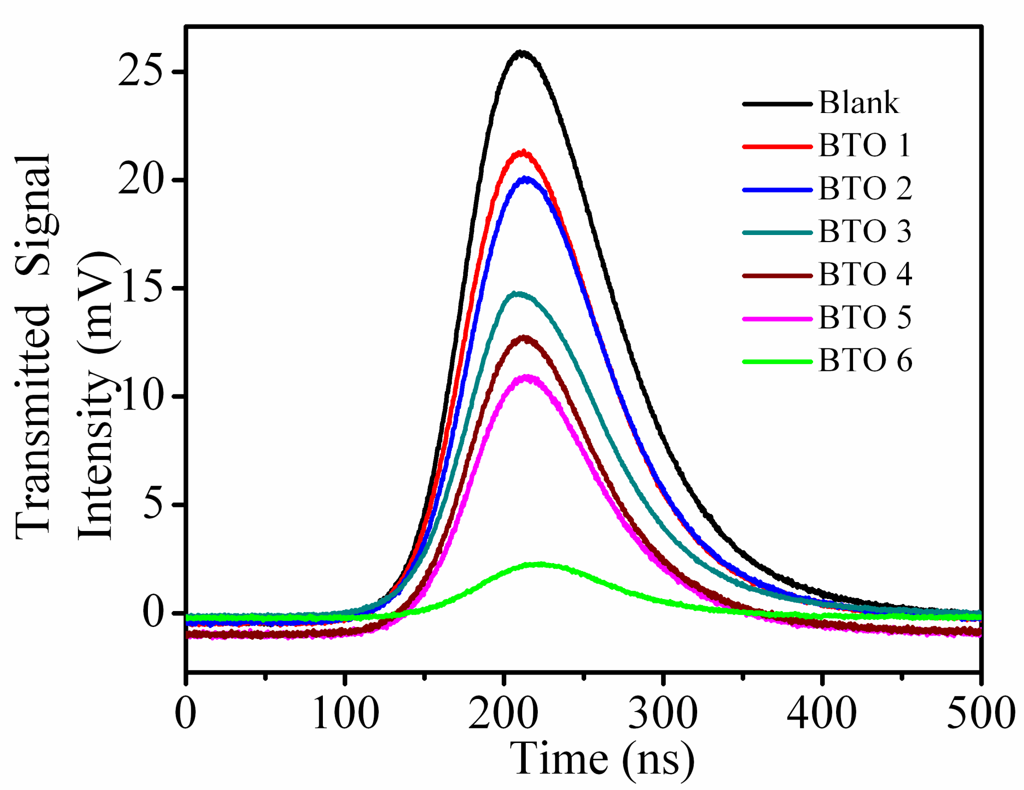

Figure 6.9 *Transmitted intensity of signal beam as a function of film thickness.*

angle of ±45˚ in the pump off and pump on conditions are shown in figure 6.10 (a) & (b) respectively. These signals were fitted to Gaussian distribution and then shifts in position of the peaks were measured to calculate the delay & advancement of pulse. A pulse delay of 13 ns was observed for +45˚ film orientation, shown in inset of figure 6.10 (a) whereas, pulse advancement of 14 ns was observed for -45˚, as shown in inset of figure 6.10 (b). This pulse delay/advancement observed in figure 6.10 can be explained on the basis of change in the effective refractive index due to the grating formation. Initially, the film was illuminated by an optical interference pattern created due to pump and signal beam. This interference leads to the photoionization and a charge carrier grating is formed in the film. Due to this charge grating a space–charge field and refractive index

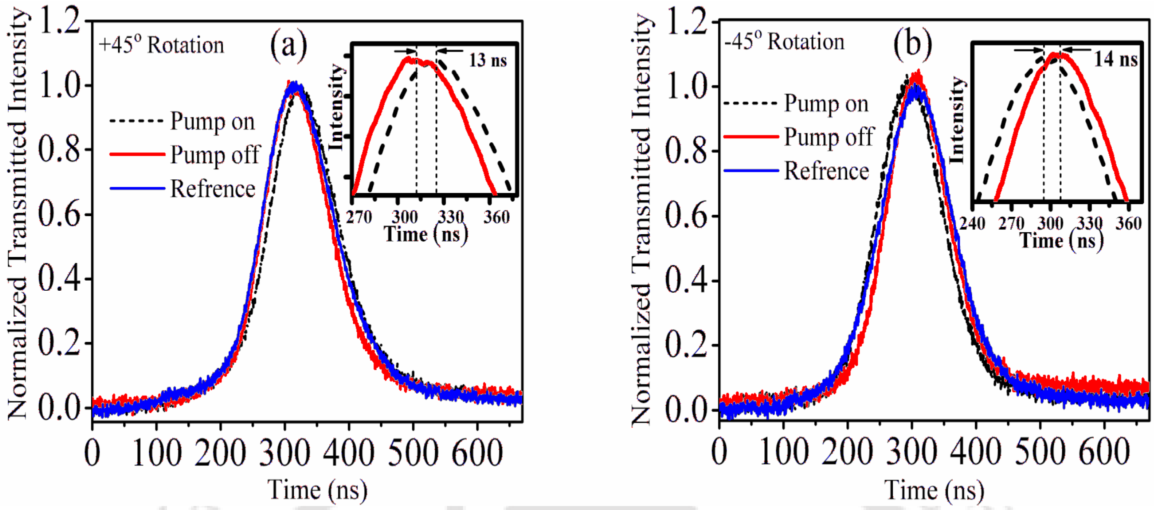

Figure 6.10 *Oscilloscope traces of the reference pulses (dashed curve) and the transmitted signal pulses in pump off and pump on conditions (a) at a angle of +45°, inset shows delay of 13 ns (b) shows at an angle of - 45° , inset shows pulse advancement of 14 ns.*

grating is formed via electro-optic effect. The grating formation with ns pulse is reported in $BaTiO_3$ crystal [**221, 222**]. Figure 6.11 shows the gain in two-wave mixing as a function of film orientation. The gain was found to increase from 1.02 to 1.53 on increasing the film orientation from 0° to 45°. The observed gain is smaller as compared to the bulk as shown in figure 6.5 (a). This could be due to several reasons. Firstly, the path length was much larger in case of crystal (5 mm) as compared to the thin film (3300 nm). It could be due to the comparatively poor crystallinity of the film as compared to crystal. The crystal used in section 6.1 is highly C-axis oriented whereas the thin film is polycrystalline as observed from XRD as well as Raman spectra (figure 5.3 (b) & 5.5 (b)). The optical delay/advancement in the pulse and corresponding group velocity as a function of film orientations is shown in figure 6.12. It can be observed from the figure 6.12 that on increasing the film orientation on the either side of normal incidence, the

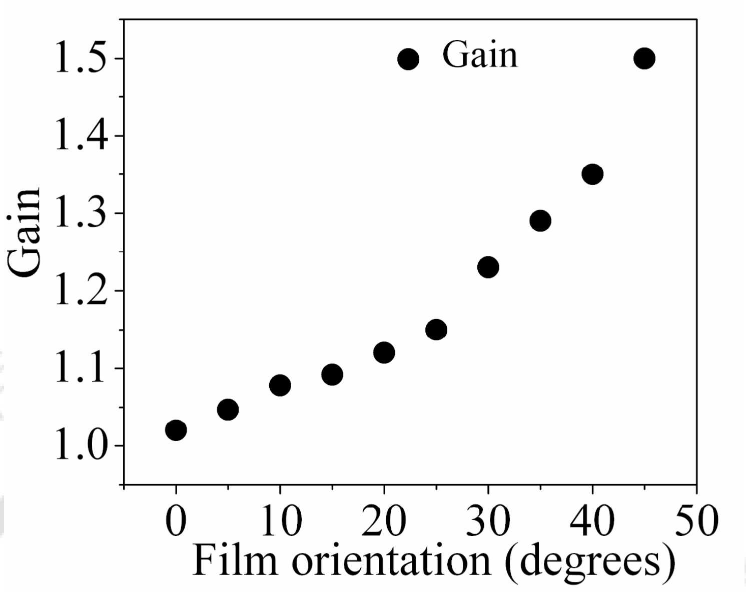

Figure 6.11 *Two-wave mixing gain as a function of film orientation.*

optical delay/advancement increases and the corresponding group velocity decreases. Such dependence of pulse delay onto the angular rotation was also observed in bulk crystal, figure 6.8, section 6.1.4 using the flat top pulses.

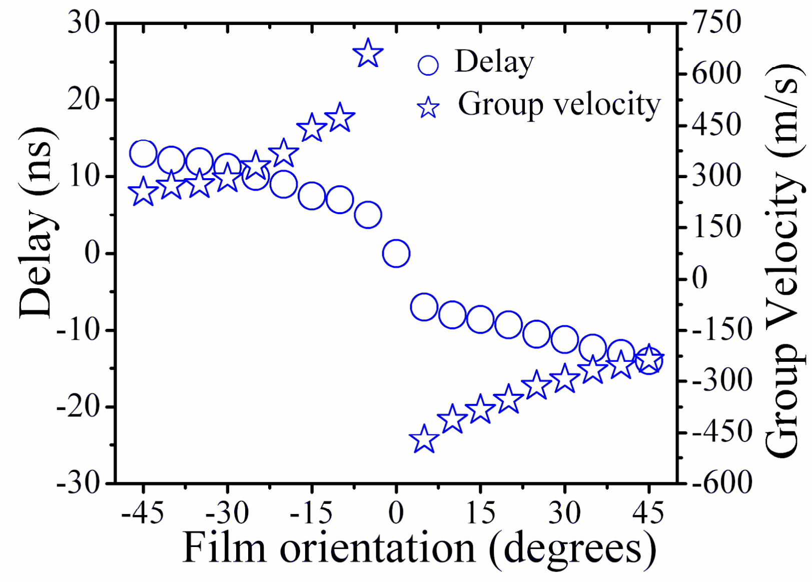

Figure 6.12 *Variation of time delay and group velocity w.r.t. the film orientation.*

The phase mismatch condition changes with the angular orientation [**225**]. As the film was rotated from 0° to $\pm 45^{\circ}$, the effective path length changes and hence the interaction of pump and signal beam undergoes modification. As a result, the energy transfer from pump to the signal beam changes on increasing the angle. Also, the fringe modulation depth and fringe displacement depends on the effective path length travelled by the input beams inside the medium [**227-230**]. All these factors will lead to the dependence of delay/advancement in transmitted signal beams on film rotation. The observed delay/advancement are found to be very small as compared to that of the bulk, because both the pump and signal beams were of ns duration and the travel length within the thin film is very small compared to that of bulk crystal. Therefore, the efficiency of the two-wave mixing process is lower than that of bulk crystal.

Conclusion

The slowing down of light is experimentally investigated via photorefractive volume grating in the Ce:$BaTiO_3$ crystal and PLD thin film of BTO via degenerate two-wave mixing configuration. The effect of pulse width onto the slowing down of light in BTO using flat top pulses of He:Ne laser is reported. The grating building up and decay time is measured at various pump intensities. The effect of pump-signal polarization, crystal orientation on delay/advancement of signal pulse is recorded. The fine tuning of delay could be achieved in S-S and P-S polarization by rotating the crystal. Further, pulse propagation of light was studied in PLD BTO thin films of thickness 3300 nm for S-S polarization using Nd:YAG laser of pulse duration of 200 ns. Transition from sub to superluminal light is observed on tuning the film orientation. For $+45^{\circ}$ film orientation, delay of 13 ns is observed whereas, pulse advancement of 14 ns is observed for -45°.

Chapter 7

Optical delay of light in epitaxial Ruby thin film

Optical delay of light at room temperature has been experimentally observed in ruby crystal [**36-39**]. The reduction in group velocity in ruby crystal of length 7.25 cm to 57.5±0.5 m/s has been explained on the basis of coherent population oscillation (CPO) [**37**]. Later on, fast light has been also observed experimentally in ruby crystal. The observations of both sub as well as superluminal pulse propagation has been explained via non-degenerate two-wave coupling (NDTWC) mechanism. On launching a TEM_{00} Gaussian beam inside a ruby crystal, mixing of different spatial frequency component of the beam leads to NDTWC [**38**]. Another mechanism for explaining optical delay of light in ruby is via Fraunhofer diffraction from the back surface of the sample **[38]**. Fraunhofer diffraction effect arises due to intensity modulation of Gaussian beam. All these phenomenon; coherent population oscillations, non-degenerate two-wave coupling mechanism, Fraunhofer diffractions, and self-phase modulation competes with each other and brings a new phenomenon of self-superluminal group velocity propagation in ruby [**38**]. The slow and fast light in ruby is also explained on the basis of saturation absorption [**91-93**]. It has been observed that when a modulated laser beam passes through a ruby crystal, it increases the modulation depth and introduces a phase delay [**35**]. The slow light based on CPO can be observed when the pulse width is larger than the population relaxation time [**37, 39**]. However, in case of short pulses, saturation can be obtained when the peak power of laser pulse is larger than the saturation intensity of the media. In such cases, the transmitted laser pulse shows delay/advancement on propagating through the medium. The modulated probe beam undergoes a phase shift after travelling through this media. Therefore, optical delay can be observed based on saturation absorption [**95-97**] even in case of laser pulses of duration smaller than the relaxation time of the level. In the present chapter, sub and superluminal pulse propagation has been experimentally demonstrated in the epitaxial ruby thin film via pulsed laser deposition technique.

7.1 Experimental Details

The best quality epitaxial ruby thin film of thickness ~ 3500 nm (sample 29, table 4.VI of chapter 4) was used to study the optical delay of light via degenerate two-wave mixing using a Gaussian laser beam of pulse width 200 ns, derived from second harmonic (532 nm) of Nd:YAG laser. The experimental setup is described in figure 2.19 of chapter 2. The peak pump intensity was ~ 820 MW/cm^2 and that of peak signal intensity was ~ 252 MW/cm^2.

7.2 Optical delay in laser pulses in epitaxial PLD Ruby thin film

Figure 7.1 (a) & (b) shows DSO traces of the reference beam and signal beam in pump off and pump on conditions at +45° sample orientations for ruby thin film and bare sapphire substrate respectively. Delay of 17 ns is observed in case of ruby film at an orientation of +45° which corresponds to a group velocity of 205.9 m/s. Figure 7.1 (b) shows the absence of any delay in case of the bare substrate. Figure 7.2 (a) shows the DSO traces for reference beam, signal beam in pump off as well as in pump on conditions for ruby thin film and 7.2 (b) shows that of bare sapphire substrate, at -45° film orientation. Pulse advancement of 12 ns is observed corresponding to fast light with group velocity of 291.7 m/s at -45° film orientation. No appreciable change is observed in case of bare sapphire substrate as shown in figure 7.2 (b).

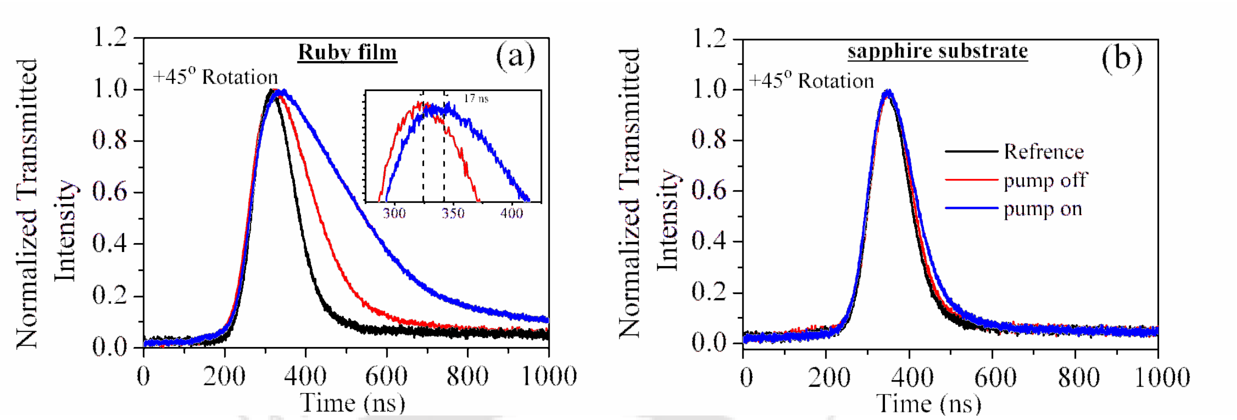

***Figure 7.1** DSO traces for transmitted signal beam in pump on and pump off conditions at film orientation of +45° for (a) ruby film and (b) sapphire substrate.*

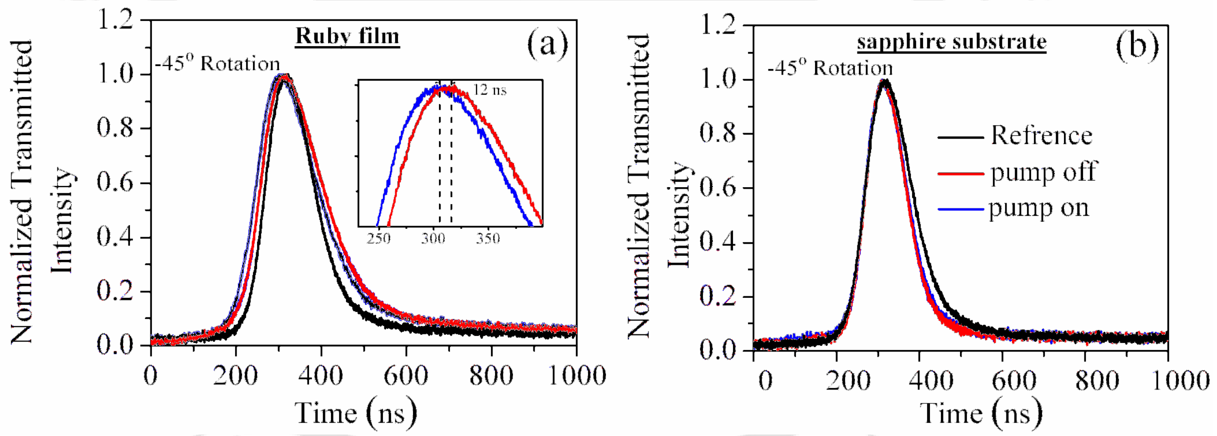

***Figure 7.2** DSO traces for transmitted signal beam in pump on and pump off conditions at film orientation of -45° for (a) ruby film and (b) sapphire substrate (black line indicates reference beam, red shows transmitted beam in pump off condition and blue line; in pump on condition).*

The effect of film orientations on the delay/advancement and corresponding group velocity of transmitted signal beam is shown in figure 7.3 (a). Figure 7.3 (b) shows the effect of film orientation

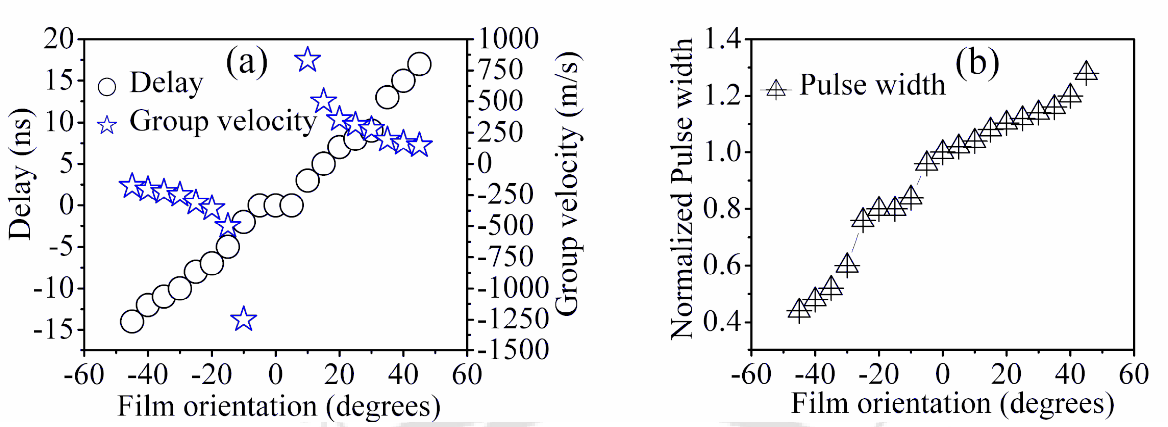

Figure 7.3 *Effect of film orientation on (a) delay and corresponding group velocity and on (b) normalized pulse width.*

on the normalized pulse width of transmitted signal beam w.r.t. the 200 ns input pulse in pump on conditions. It can be observed from figure 7.3 (b), that on rotating the film from 0° to -45° the transmitted signal beam is compressed. On the other hand when the film was rotated from 0° to +45° the transmitted signal beam shows broadening. Since the pulse duration in the present case (200 ns) is much smaller than 3 ms, the population relaxation time of ruby therefore, mechanism for the group delay via CPO is ruled out [**231**]. However, due to very high peak intensities used in the present experiment, the observed behavior can be attributed to the saturation absorption. It has been earlier reported that saturation can be obtained with a pulsed high-power laser in a time short compared to the lifetime of a particular excited state [**98**]. The saturation intensity of ruby is I_s ~ 1.5 kW/cm^2, is much smaller than the peak intensities of pump (~ 820 MW/cm^2) and signal beam (~ 252 MW/cm^2) in the present case. Therefore, in the presence of very intense pump beam the saturation absorption will take place in the ruby film and the signal beam transmitted through the film will show change in group velocity. Both sub as well as superluminal pulse will be generated depending upon the phase shift of signal pulse inside the medium. The phase shift inside the medium depends upon the film orientation w.r.t. the pump beam. On changing the orientation of medium the effective path length traversed by the beam inside it will change. This in turn will lead to change in group velocity [**224, 225**]. Therefore, the variable optical delay shown in figure 7.3 (a), is due to change in effective length. The observed broadening and compression as shown in figure 7.3 (b) could be attributed to nonlinear dispersion effects [**232**]. The nonlinear dispersion produces frequency chirp in the medium and the pulse width of transmitted signal beam gets modified accordingly.

Conclusion

Sub and superluminal propagation of 200 ns gaussian beam from 2nd harmonic of Nd:YAG laser is demonstarted in the epitaxial ruby thin film grown via PLD. The group delay can be tuned by the orientation of the film.

Chapter 8

Ruby and Barium titanate thin films as a photonic temperature sensor

Photonic based sensors have numerous advantages over conventional sensors [**233, 234**]. These are immune to environmental electromagnetic interference, robust, small in size and flexible. In recent years, various types of photonic based sensors are proposed for temperature measurement. Among them, optical fibre based temperature sensors are very popular due to their light weight and flexibility [**234**]. But these are fragile and can`t withstand high temperature. This put serious limitation in its applicability at high temperature and in harsh environment [**115-124**]. One of the robust materials with very high melting point (2044˚C), [**2**] in which temperature sensing has been proposed over a wide temperature range, is ruby crystal. The characteristic R-line of ruby, shows temperature dependence [**11**]. Another solid state material, for temperature sensing in broad temperature range, is barium titanate crystal. It shows phase change from low temperature rhombohedral to high temperature cubic phase [**53**]. In the room temperature, it is predominantly tetragonal in phase. The 308 cm^{-1} Raman band of BTO, signature of tetragonal phase, shows systematic change in its FWHM and intensity with temperature [**54**]. Therefore, ruby and BTO can be seen as potential candidate for temperature sensing applications. For compact photonic circuits, the thin film geometry is preferred for the photonic based temperature sensors.

8.1 Temperature dependent PL spectra of Ruby thin film

For an ideal thin film temperature sensor of ruby, R-line fluorescence should be very strong, line-width should be narrow and sensitivity of the sensor should be linear. The quantum efficiency of R-line is very high therefore, it possess high signal to noise ratio.

In case of ruby the fluorescence line-width of R-lines is a function of crystal perfection, stress, strain and temperature in the crystal/thin film [**10**]. Therefore, the grown film for temperature sensing application should be highly crystalline, uniform and free from stress and strain. Inhomogeneity and stress in the deposited film will cause additional line broadening apart from the temperature dependent contribution and hence will reduce the accuracy of measurement [**127**].

The best quality epitaxial thin film of ruby of thickness ~ 260 nm (sample 11, table 4.I, chapter 4) was taken for temperature sensing application. The details of the temperature sensing setup is described in section 2.7, figure 2.20. Figure 8.1 shows the temperature dependent photoluminescence in the temperature range of 138 K - 473 K for R-line of epitaxial film of ruby. It can be seen from the figure 8.1 that the R-line peaks

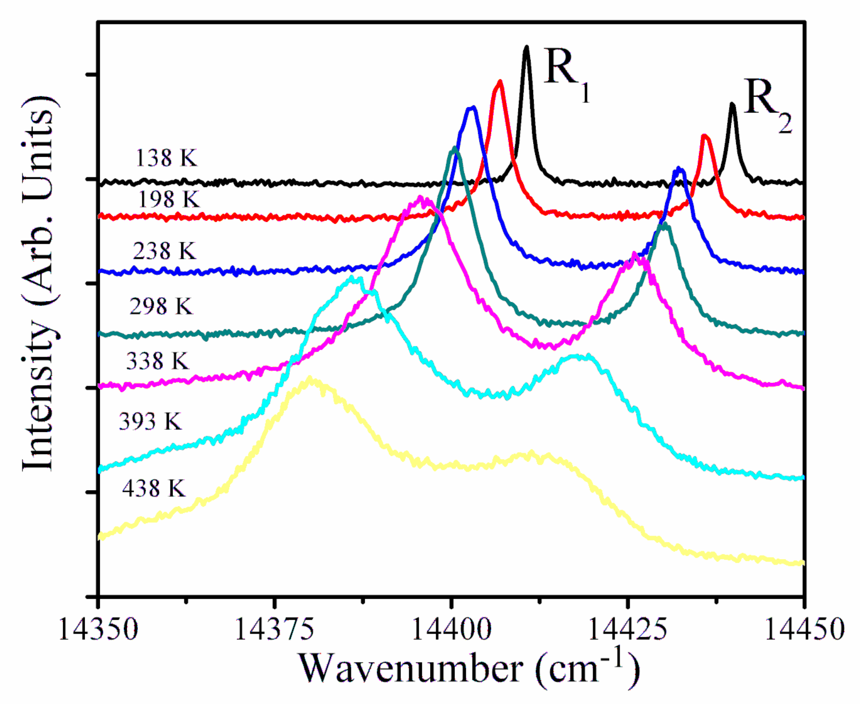

Figure 8.1 *PL spectra of ruby film at seven different temperatures.*

are blue shifted and becoming sharp at lower temperature as reported in case of bulk ruby [**11**]. The observed profile is in accordance with two-phonon Raman scattering process [**127**]. All the spectra were very well fitted to double Lorentzian line shape with the coefficients of determination for the fits $r^2 \geq 0.999$. This reveals that the sample is stress free and the line broadening is only due to the temperature variation. The variation of line-width, peak position, PL intensity and splitting of R_1 and R_2 lines as a function of temperature are shown in figure 8.2. The line- width and peak position is calculated fromthe Lorentzian fitted data. It can be observed from figure 8.2 (a) that the width of both these lines increases with temperature. The width of R_2 line is seen to be smaller than that of R_1-line, as reported in literature in case of bulk [**11**]. The width of R_1 & R_2 line in high temperature range from 300 K- 473 K is fitted well to linear fit with coefficients of determination $r^2 \sim 0.994$ & $r^2 \sim 0.989$ respectively. The R_1 and R_2 line position as a function of temperature is fitted well to cubic equations, 8.1 and 8.2 as shown in figure 8.2 (b).

$$R_1(T) = 14420 + 6.34 \times 10^{-2}\, T - 5.11 X\, 10^{-4}\, T^2 + 4.087 \times 10^{-7}\, T^3 \tag{8.1}$$

$$R_2(T) = 14450 - 1.86 \times 10^{-2} T - 1.96 \times 10^{-4} T^2 + 5.648 \times 10^{-7}\, T^3 \tag{8.2}$$

The coefficient of determination for the fits, given by Eqs. 8.1 and 8.2, $r^2 \geq 0.999$ indicating that these fits can be used with very high confidence. The PL intensity of R-line as observed from figure 8.2 (c) first increases on increasing the temperature and then decreases. The R-line splitting with temperature is shown in figure 8.2 (d). The splitting increases from 29.2 cm^{-1} to 29.6 cm^{-1} slowly on increasing the temperature from 138 K to 250 K, and then rapidly reaches a maximum value of 31.5 cm^{-1} at 400 K. On further

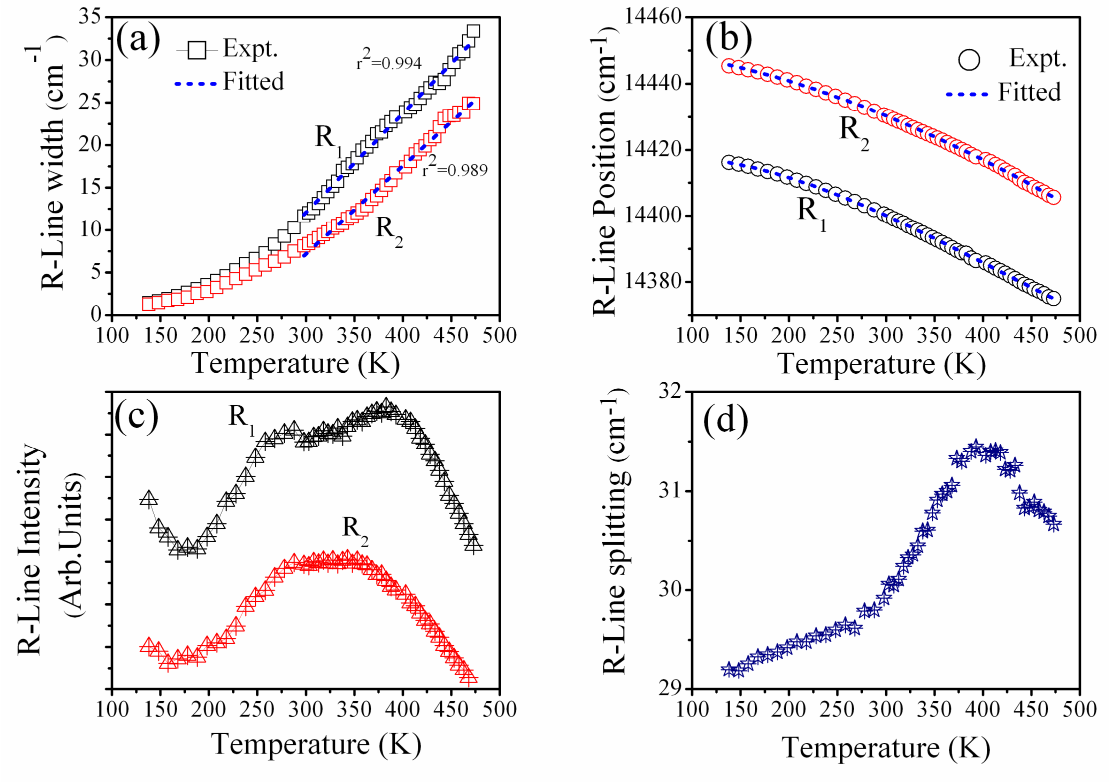

Figure 8.2 *Variation of (a) R-line width, (b) R-line position, (c) PL intensity of R-line and (d) changes in R-line splitting with temperature.*

increasing the temperature the splitting falls down. The observed splitting is in agreement with the bulk ruby crystal [**11**]. With the increase in temperature, the Cr^{3+} ion shifts slightly in relation with the surrounding oxygen resulting into the change in splitting of energy levels $2\bar{A}$ and $\bar{E}$ [**11**], figure 4.4, chapter 4.

8.1.1 Sensitivity of the PLD Ruby thin film sensor

The sensitivity; line shift per Kelvin (cm^{-1}/K), $d\bar{v}/dT$, of R-line position is shown in figure 8.3, as the coefficient for cubic term is three order of magnitude less compared to quadratic term therefore the sensitivity of R_1-line position in the range 138 K to 368 K was fitted to linear fit as shown in figure 8.3. The coefficient of determination was

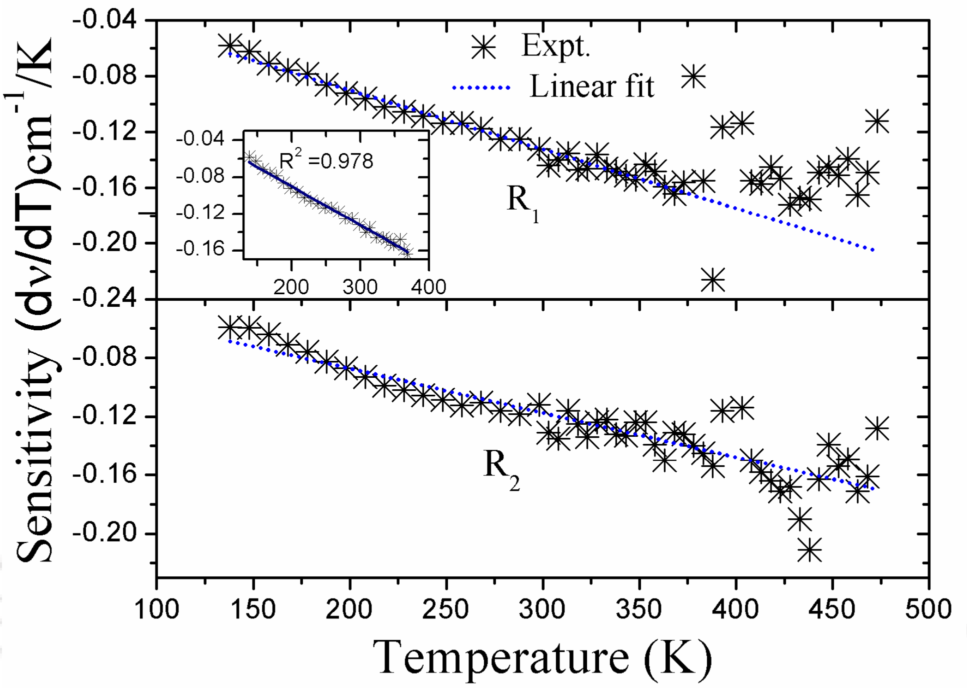

Figure 8.3 *Sensitivity of R_1 and R_2 line position with temperature. Inset shows R_1 line position fitted well to the linear fit in the range 138 K- 368 K.*

r^2 ~ 0.978, confirming the sensitivity to be linear, one of the desirable quality of any sensor. The sensitivity for R_2-line is deviating from linear behavior. The deviation from linear fit is prominent in high temperature range for both R_1 & R_2 lines. The R_1-line position can be easily used as the parameter for measuring the temperature in the range of 138 K to 368 K. Whereas, in the high temperature range of 370 K - 475 K the R_1, R_2 line-width can be used for the temperature sensing application, figure 8.2 (a).

8.2 Temperature dependent studies of Barium titanate thin film

The temperature dependent Raman spectra of BTO thin film of thickness ~ 3300 nm (sample no: BTO 6, table 5.I of chapter 5) is recorded and analyzed for temperature sensing applications in the range of 146 K – 440 K. Figure 8.4 shows the Raman spectra at 146 K, 226 K, 300 K and 466 K. The Raman bands are deconvoluted and corresponding peak positions are marked in the figure 8.4. Figure 8.4 (a) shows the low temperature rhombohedral phase at 146 K. The Raman bands were located at 156 cm^{-1}, 187 cm^{-1} A_1(1TO), 269 cm^{-1} A_1(2TO), 312 cm^{-1} B_1(1TO), 532 cm^{-1} A_1(3TO) and 718 cm^{-1}. The 269 cm^{-1} band was the most prominent band in the low temperature phase.

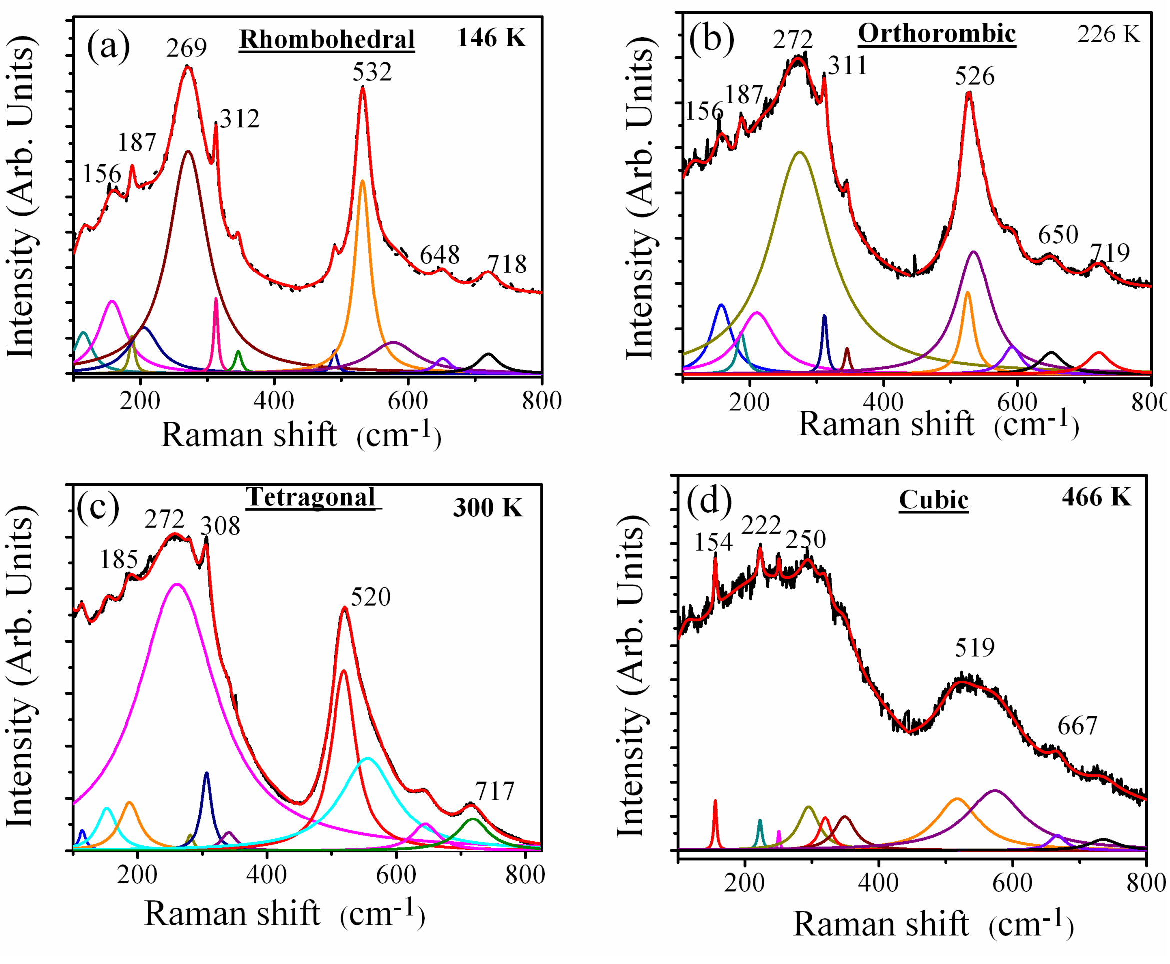

Figure 8.4 *Phase transition in BTO thin film from (a) Rombohedeal, (b) Orthorombic, (c) Tetragonal to (d) Cubic phase.*

The sharp band at 156 cm^{-1} and 187 cm^{-1} is the signature of rhombohedral phase [**235**]. With the increase in temperature to 226 K the BTO thin film was observed to be oriented to orthorhombic phase as confirmed by the shift of 269 cm^{-1} band to 272 cm^{-1} and reduction in intensity of 156 cm^{-1} and 187 cm^{-1} bands [**235**] as shown in figure 8.4 (b). Further, the orthorhombic to tetragonal transition in BTO thin film has been observed by suppression of 272 cm^{-1} band and shift of 311 cm^{-1} band to 308 cm^{-1} [**235**]. The room temperature (300 K) tetragonal phase is shown in figure 8.4 (c). On increasing the temperature to 446 K the Raman bands at 520 cm^{-1} and 308 cm^{-1} are observed to be suppressed as shown in figure 8.4 (d), indicating the cubic phase. Ideally, the cubic phase in single crystal of BTO is Raman inactive but may show Raman bands due to stress, as shown in figure 8.4 (d). The observed behavior is signature of cubic phase in BTO thin film. Therefore, it has been observed from figure 8.4 that on increasing the temperature the intensity of Raman bands has been reduced on changing the phase from rhombohedral to cubic.

Figure 8.5 (a) clearly shows the increase in broadening of Raman band at 308 cm^{-1} for BTO thin film in the temperature range of 146 K – 506 K. Peak positions also shows the shift towards the lower wave number with the increase in temperature.

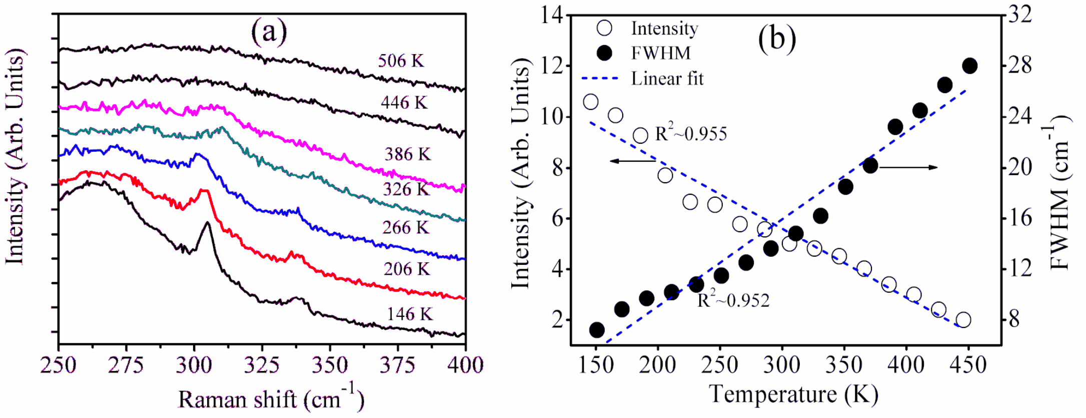

Figure 8.5 *(a) Temperature dependence of 308 cm^{-1} in the range 146 K to 506 K, corresponding, (b) integrated intensity and FWHM.*

This band is found to almost vanish above 450 K corresponding to the cubic phase at high temperature. The FWHM and integrated Raman intensity were extracted from the Lorentzian fitting of 308 cm^{-1} band and are plotted as a function of temperature in figure 8.5 (b). The change in intensity and FWHM was not abrupt at any temperature as shown in figure 8.5 (b), this confirms the diffuse phase transition in the thin film of BTO [**54**]. The Raman intensity as well as FWHM was found to vary linearly with increasing the temperature in the temperature range of 146 K to 440 K. The coefficient of determination for the linear fit of FWHM and intensity was $r^2 \sim 0.955$ and $r^2 \sim 0.952$ respectively. Similar kind of behavior in FWHM and intensity was observed in case of bulk and epitaxial BTO film [**53, 55**] prepared by pulsed laser deposition technique [**54**]. But the broadening is higher in the present case of PLD film on quartz substrate as compared to that of reported in literature [**54**]. This could be due to higher lattice mismatch in case of BTO film deposited on quartz substrates compared to film on MgO substrate [**54**].

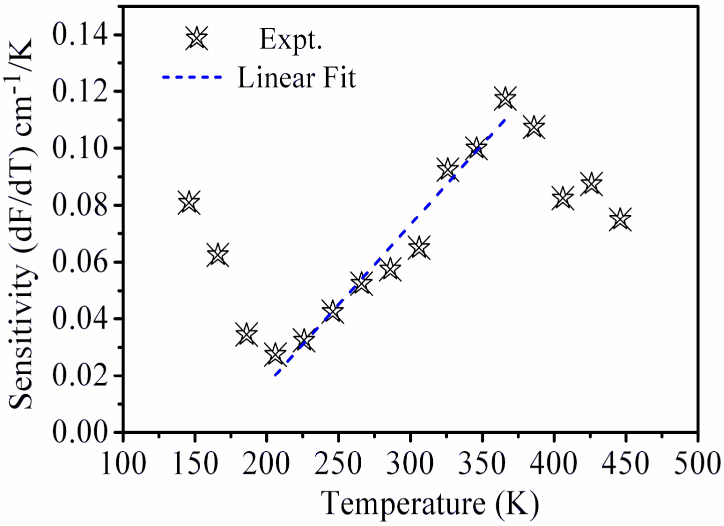

Figure 8.6 *Sensitivity of FWHM of 308 cm^{-1} Raman band with temperature. Experimental data in the range 200 K to 375 K is fitted well to linear fit.*

The sensitivity; FWHM per Kelvin (cm^{-1}/K), dF/dT, of 308 cm^{-1} Raman band, is shown in figure 8.6. In the temperature range 200 K to 375 K the sensitivity is found to be linear. Above 375 K and below 200 K, it is deviating from the linear behavior. Therefore, the BTO thin film can be used as a temperature sensor in the range of 150 K-450 K by using the combination of intensity, FWHM and the line shift of Raman band at 308 cm^{-1} corresponding to tetragonal phase of polycrystalline thin film of BTO.

Conclusion

Highly C-axis oriented epitaxial thin film of ruby was subjected to temperature dependent photoluminescence studies in the temperature range of 138 K - 473 K. The R-line width, position, peak intensity and splitting were recorded as a function of temperature. R_1-line position sensitivity, $d\bar{v}/dT$, cm^{-1}/K in the range 138 K - 368 K is very well fitted to linear fit and hence can be used as temperature sensor in this range. In the low temperature range R_1-line position can very well act as a linear temperature sensor, whereas in the high temperature range (from 370 K - 475 K), the R_1 and R_2 line-width can be used for the temperature sensing application.

The Raman bands of polycrystalline BTO thin film confirmed phase transition from low temperature rhombohedral to high temperature cubic phase. The variation in FWHM and integrated intensity of 308 cm^{-1} Raman band varied linearly with temperature in the temperature range of 146 K to 440 K, confirming its applicability as a linear temperature sensor.

Chapter 9

Conclusion

A detailed parametric characterization of ruby and BTO thin film by PLD technique was reported in the present thesis. A 2nd harmonic of Nd:YAG laser was focused onto the respective targets in oxygen ambient for deposition of thin film. The PLD thin films were subjected to XRD, laser Raman, photoluminescence, AFM, UV-Visible and profilometer studies for various characterizations. The NLO properties of both these thin films were also investigated in the present work.

Ruby thin films were deposited over wide range of deposition parameters. The effect of substrate temperature, annealing, laser fluence, oxygen gas pressure and deposition time on crystallinity and thickness of PLD ruby thin films has been documented in the present thesis. Films deposited at higher substrate temperature (750˚C) were found to be of better quality as compared to the film grown at lower substrate temperature (RT & 650˚C). Ruby films deposited on quartz substrate were found to be of amorphous in nature as compared to the film grown on sapphire substrate due to lattice matching with later. The crystallinity of the PLD ruby thin films were observed to be improved by annealing the films at 1000˚C for 2 hrs due to release of stress from the films. Further, the crystallinity and thickness of the ruby film was improved by increasing the laser fluence from ~ 2 J/cm^2 to ~ 23 J/cm^2, beyond this the film quality was deteriorated. On increasing the oxygen gas pressure from ~ 10^{-5} mbar to ~ 5 mbar the thickness of ruby film was improved due to confinement of laser produced plasma. Beyond this, the film thickness fell down due to over confinement of laser produced plasma which prohibited the impingement of ablated species on the substrate. With the increase in deposition time from 30 min to 6 hrs the crystallinity and thickness of PLD ruby thin film was found to improve. The optimum parameters for PLD deposition of ruby thin films were found to be; substrate temperature: 750˚C, substrate: sapphire, annealing: 1000˚C for 2 hrs, laser fluence: ~ 23 J/cm^2 and gas pressure: ~ 5 mbar.

The quality of PLD deposited thin film is governed by the plasma temperature and ion density of LPP. These parameters were measured by using Langmuir probe technique as a function of distance w.r.t. target, laser fluence and gas pressure in the present work. The electron temperature, T_e, was observed to decrease from 16 eV to 4.5 eV and ion density was found to reduce from 2.4 x 10^{13} cm^{-3} to 2.9 x 10^{12} cm^{-3}, on increasing the distance from 10 mm to 80 mm. It was observed that neutral formation in the LPP was dominating between 40 mm - 50 mm. Thus, 40 mm was chosen as a substrate to target distance for thin film deposition via PLD. The electron temperature was found to increase from 0.5 eV to 3.2 eV and the ion density was also found to increase from 3.6 ×10^{11} cm^{-3} to 6.8 × 10^{12} cm^{-3} with increase in laser fluence from ~ 6.2 J/cm^2 to ~ 30 J/cm^2. The increase in plasma temperature and density was fast upto a laser fluence of ~ 23 J/cm^2. Beyond ~ 23 J/cm^2, the plasma temperature and density showed the trend towards saturation. Thus, laser fluence of ~ 23 J/cm^2 was considered as optimum laser fluence and was in agreement with the thin film deposited at this fluence. At optimum deposition distance of 40 mm, electron temperature initially increased from 0.8 eV to 3.8 eV, on increasing the pressure from ~ 10^{-5} mbar to ~ 5 × 10^{-2} mbar. On further increasing the pressure from ~ 0.1 mbar to ~ 10 mbar the electron temperature was found to reduce from 2.5 eV to 0.5 eV. The corresponding ion density was observed to reduce from 2.1 ×10^{12} cm^{-3} to 6.2 × 10^{10} cm^{-3}, on increasing the gas pressure from ~

10^{-5} mbar to ~ 10 mbar. The fall in ion density was drastic from ~ 10^{-5} mbar to ~ 10^{-1} mbar and beyond that it is almost constant. Oxygen gas pressure of ~ 5 mbar was found to be appropriate for deposition of ruby film with maximum deposition rate via PLD.

Finally, the epitaxial ruby thin film was deposited on double sided polished sapphire substrate using optimized deposition parameters (substrate temperature: 750˚C, substrate: sapphire, annealing: 1000˚C for 2 hrs, laser fluence: ~ 23 J/cm^2, gas pressure: ~ 5 mbar, deposition time: 6 hrs) of PLD. The thickness of film was ~ 3500 nm. This film was subjected to Z-scan studies for determination of nonlinear absorption and nonlinear refractive index. The measured value of optical nonlinear parameters were found to be, $\beta \sim 5.2 \times 10^{-5}$ m/W and nonlinear refractive index, $n_2 \sim 3.1 \times 10^{-5}$ m^2/W. The obtained value of n_2 is three orders of magnitude larger than that of ruby crystal. This film of ruby was subjected to optical delay studies via degenerate two-wave mixing technique using 200 ns Gaussian pulse of Nd:YAG laser. On tuning the film orientation, both sub as well as superluminal pulse propagation was observed. Delay of 17 ns was observed in case of ruby film at an orientation of +45˚ which corresponds to a group velocity of 205.88 m/s. Pulse advancement of 12 ns was observed corresponding to fast light with group velocity of 291.66 m/s at -45˚ film orientation. Pulse compression and broadening was also observed.

The epitaxial ruby thin film of thickness ~ 260 nm was subjected to temperature sensing studies in the temperature range 138 K - 468 K. R_1-line position sensitivity, $d\bar{v}/dT$, cm^{-1}/ K in the range 138 K - 368 K was very well fitted to linear fit. In the low temperature range, R_1-line position can very well act as a linear temperature sensor, whereas, in the high temperature range (from 370 K - 475 K), the R_1 and R_2 line-width can be used for the temperature sensing application.

The another series of thin film fabricated via PLD was BTO thin film was deposited using PLD technique for 30 min, 1 hr, 2 hrs, 3 hrs, 4 hrs and 6 hrs on quartz substrate, using optimized deposition parameters viz. obtained from literature (substrate to target distance 40 mm, substrate temperature: 750°C, laser fluence ~ 10 J/cm^2). These films were annealed at a temperature of 1000°C for two hours. The tetragonality of the PLD BTO thin film was found to improve with increase in deposition time. The thickness of the film was found to increase from 62 nm to 3300 nm on increasing the deposition time from 30 min to 6 hrs.

The BTO film of thickness ~ 3300 nm was subjected to Z-scan and optical delay studies. The nonlinear absorption coefficient was found to be, $\beta \sim 8.6 \times 10^{-7}$ m/W. The real and imaginary part of susceptibility were found to be $\chi^{(3)}(\mathrm{Re}) \sim 7.5 \times 10^{-7}$ esu and $\chi^{(3)}(\mathrm{Im}) \sim 9.8 \times 10^{-8}$ esu respectively. A pulse delay of 13 ns was observed for +45° film orientation whereas, pulse advancement of 14 ns was observed for -45°. On increasing the film orientation on either side of normal incidence the optical delay/advancement increased and the corresponding group velocity decreased indicating that these films can be used for fine tuning of delay of the laser pulses.

This BTO film of thickness ~ 3300 nm was subjected to temperature dependent Raman studies in the range 146 K – 506 K. The FWHM and intensity of 308 cm^{-1} Raman band showed linear shift with temperature in range 146 K to 440 K. The sensitivity of

FWHM in range 200 K to 375 K was found to be linear confirming its suitability as temperature sensor.

The optical delay has also been studied in Ce:BaTiO$_3$ crystal (5 mm × 5 mm × 7 mm) via degenerate two-wave mixing using millisecond chopped pulses of a CW He:Ne laser (632.8 nm) in the present work. On increasing the flat top signal pulse width from 2 ms to 20 ms the optical delay was found to increase from 0.3 ms to 1.2 ms and the corresponding group velocity was varied from 16.67 m/s to 4.16 m/s. The pump intensity was varied from ~ 1.2 W/cm^2 to ~ 0.048 W/cm^2. In the range of ~ 1.2 W/cm^2 to ~ 0.7 W /cm^2, delay was inversely proportional to the pump intensity. Below ~ 0.7 W/cm^2 the delay was fluctuating due to low index modulation of grating. The polarization dependent studies showed that in case of S-S and P-S polarization states of pump and signal beam respectively, the transmitted signal beam was amplified and free from distortion. Transition from slow to fast light was observed on tuning the crystal orientation.

Future Scope of Work

The epitaxial ruby thin film developed in the present work can be used for fabrication of tunable optical delay line. The sensitivity of the epitaxial ruby thin film proposed as a photonic sensor can be enhanced by optimizing the Cr^{3+} concentration. The other sensing capability viz. stress and acoustic can be explored on PLD thin film of ruby.

Another solid state material in which tunable optical delay and the gain in thin film geometry is experimentally demonstrated in the present thesis is polycrystalline barium titanate thin film. The NLO properties reported in the present thesis can be improved by depositing the epitaxial film in preferred tetragonal phase by using suitable substrate e.g. MgO, for various applications. The temperature sensitivity of Raman spectra can also be modulated with the best quality BTO thin film.

Both these PLD thin film; ruby and barium titanate can be used for waveguide writing and can be tested for optical tunable delay as a function of frequency detuning, polarization and pump-probe intensity. These films can be explored for future integrated photonic device applications.

Bibliography

[1] T. H. Maiman, “Stimulated optical radiation in ruby”, Nature, **187**, 493-494 (1960).

[2] R. C. Powell, Physics of solid state laser engineering, AIP Press (1998).

[3] T. H. Maiman, R. H. Hoskins, I. J. D’Haenens, C. K. Asawa, and V. Evtuhov “Stimulated optical emission in fluorescent solids. II spectroscopy and stimulated emission in ruby”, Phys. Rev., **123**, 1151-1157 (1961).

[4] A. L. Mahan, C. Bitterli, S. M. Cannon, and D. G. Grant, “Ruby as a macroscopic fluorescing and laser materials”, J. of Opt. Soc. of Am., **59**, 49-59 (1969).

[5] D. F. Nelson and M. D. Sturge, “Relation between absorption and emission in the region of R lines of ruby”, Phy. Rev., **137**, A1117-A1130 (1965).

[6] D. C. Cronemeyer, “Optical absorption characteristics of pink ruby”, J. of Opt. Soc. of Am., **56**, 1703-1706 (1966).

[7] G. F. Imbusch, “Energy transfer in ruby”, Phys. Rev., **153**, 326-337 (1967).

[8] U. Rothamal, J. Heber and W. Grill, “Vibronic sidebands in Ruby”, *Z.Phys. B* – Cond. Mat., **50**, 297-304 (1983).

[9] G. F. Imbusch, “Energy transfer in heavily-doped ruby”, J. of Lumin., **53**, 465 – 467 (1992).

[10] R. C. Powell, B. Dibartolo, B. Birang and C. S. Naiman, “Fluorescence Studies of Energy Transfer between Single and Pair Cr^{3+} Systems in Al_2O_3”, Phys. Rev., **155**, 296- 308 (1967).

[11] D. D. Ragan, R. Gustavsen and D. Schiferl, “Calibration of the ruby R_1 R_2 fluorescence shifts as a function of temperature from 0 to 600 K”, J. Appl. Phys., **72**, 5539-5544 (1992).

[12] M. Dong-Ping , L. Yanyun, M. Ning, C. Jurong, “Theoretical calculations of thermal shifts and thermal broadenings of sharp lines and zero-field splitting for ruby part I. Thermal shifts of R_1 and R_2 lines”, J. of Phys. and Chem. of Solids, **61** , 799–808 (2000).

[13] K. T. V. Grattan, R. K. Selli, and A. W. Palmer, “Ruby fluorescence wavelength division fiber-optics temperature sensor”, Rev. Sci. Instrum., **58**, 1231-1234 (1987).

[14] H. C. Seat, J. H. Sharp, Z. Y. Zhang, K. T. V. Grattan, “Single crystal ruby fiber temperature sensor”, Sensors & actuators A, **101**, 24-29 (2002).

[15] Q. Wen, N. Yu and D. R. Clarke, "Epitaxial thin-film ruby as an ion-irradiation damage sensor", J. Appl. Phys. **80**, 3587- 3589 (1996).

[16] L. G. Tilstra, A. F. M. Arts and H.W. de Wijn, "Coherence of phonon avalanches in ruby", Phys. Rev. B, **68**, 144302 – 1 to 144302-7 (2003).

[17] H. W. de. Wijn, "Phonon physics in ruby studied by optical pumping and luminescence", J. of Lumin., **125**, 55-59 (2007).

[18] L. G. Tilstra, A. F. M. Arts, and H.W. de Wijn, "Optically excited ruby as a saser: Experiment and theory", Phys. Rev. B, **76**, 024302-1- 024302-12 (2007).

[19] J. P. Wittke, "Effects of elevated temperatures on the fluorescence and optical Maser action of Ruby", J. of Appl. Phys., **33**, 2333-2335 (1962).

[20] H. Aizawa, N. Ohishi, S. Ogawa, T. Katsumata, S. Komuro, T. Morikawa and E. Toba, "Fabrication of ruby sensor probe for the fiber-optic thermometer using fluorescence decay", Rev. Sci. Instrum., **73**, 3656-3658 (2002).

[21] Y. Shen, Y. Wang, L. Tong, and L. Ye, "Novel sapphire fiber thermometer using fluorescent decay", Sensor & Actuators A, **71**, 70-73 (1998).

[22] T. Kobayashi, T. Sekine, X. Li and Y. Yamashita, "Shock Response of Ruby Crystal Studied by Pulsed Excitation Luminescence Spectroscopy", Jpn. J. Appl. Phys., **42**, 5720–5721 (2003).

[23] G. J. Piermarini, S. Block, J. D. Barnett, and R. A. Forman, "Calibration of the pressure dependence of the R 1 ruby fluorescence line to 195 kbar", J. of Appl. Phys., **46**, 2774-2780 (1975).

[24] J.-K. Hyun, S. M. Sharma and Y. M. Gupta, "Ruby R-line shifts for shocks compression along (1102)", J. of Appl. Phys., **84**, 1947-1952 (1998).

[25] U. Gibson & M. Chernuschenko, "Ruby films as surface temperature and pressure Sensors", Opt. Express, **4**, 443-448 (1999).

[26] P. D. Horn and Y. M. Gupta, "Luminescence *R*-line spectrum of ruby crystals shocked to 125 kbar along the crystal *c* axis", Phys. Rev. B, **39**, 973-979 (1989).

[27] Y. Zhao, C. Wu, B.-S. Ham, M. K. Kim and E. Awad, "Microwave induced transparency in ruby", Phys. Rev. Lett., **79**, 641-644 (1997).

[28] B. L. Bean and J. R. Izatt, "Verification of the Kramers-Kronig relation in optically pumped ruby", J. of Opt. Soc. of Am., **63**, 832-839 (1973).

[29] T. Catunda and L. A. Cury, "Transverse self-phase modulation in ruby and $GdAlO_3$:Cr^{+3} crystal", J. Opt. Soc. Am. B, **7**, 1445-1455 (1990).

[30] S. A Boothroyd, J. Chrostowski, and M. S. O'Sullivan, "Two-wave mixing by phase and absorption grating in saturable absorbers", J. Opt. Soc. Am. B. , **6**, 766-771 (1989).

[31] L. C. Oliveira and S. C. Zilio, "Single-beam time-resolved Z-scan measurement of slow absorbers", Appl. Phys. Lett., **65**, 2121-2123 (1994).

[32] I. McMicheal, P. Yeh, and P. Beckwith, "Nondegenerate two-wave mixing in ruby", Opt. Lett., **13**, 500-502 (1988).

[33] L. W. Hillman, R. W. Boyd, J. Krasinski , C.R. Stround, Jr., "Observation of spectral hole due to the population oscillations in a homogeneously broadened optical absorption line ", Opt. Comm., **45** , 416-419 (1983).

[34] A. Szabo, "Ultra-narrow optical hole burning in ruby", J. of Lumi., **56**, 47-50 (1993).

[35] M. A. Kramer, R. W. Boyd, L. W. Hillman, and C.R. Stround, Jr., "Propagation of modulated optical fields through saturable-absorbing media: a general theory of modulation spectroscopy", J. Opt. Soc. Am., **2**, 1444-1455 (1985).

[36] M. S. Bigelow, N. N. Lepeshkin, and R. W. Boyd, "Superluminal and slow light propagation in a room temperature solid", Science, **301**, 200-202 (2003).

[37] M. S. Bigelow, N. N. Lepeshkin and R. W. Boyd, "Observation of ultraslow light propagation in a ruby crystal at room temperatures", Phys. Rev. Lett., **90**, 113903-1 to 113903-4 (2003).

[38] F. Gao, J. Xu, G. Zhang, F. Bo, and H. Liu, "Paraxial energy transport of a focused Gaussian beam in ruby with non degenerate two-wave coupling like mechanism", Appl. Phys. Lett., **92**, 021121-1 to 021121-3 (2008).

[39] L. Cerdan, R. Weigand. J. M. G. Perez, and H. Crespo, "A simple experiment on slow light in ruby", Am. J. Phys., **76**, 826-832 (2008).

[40] W. Xue, S. Sales, J. Mørk, and J. Capmany, "Widely Tunable Microwave Photonic Notch Filter Based on Slow and Fast Light Effects", IEEE Phot. Tech. Lett., **21**, 167-169 (2009).

[41] M. Santagiustina, G. Eisenstein, L. Thévenaz, J. Capmany, J. Mork, J.P. Reithmaier, A. De Rossi , S. Sales, K. Yvind, S. Combrié, J. Bourderionnet, "Slow Light Devices and Their Applications to Microwaves and Photonics", IEEE Phot. Soc. Newsletter**,** 5-12 (2012).

[42] O. Deparis and O. E. Daif, "How Much Can Slow Light Increase the Efficiency in Thin-Film Planar Solar Cell Devices", Advanced Photonics Congress © 2012 OSA ITu2C.5.pdf

[43] E. Podivilov and B. Sturman, A. Shumelyuk and S. Odoulov, "Light Pulse Slowing Down up to 0.025 cm/s by Photorefractive Two-Wave Coupling", Phys. Rev. Lett., **91**, 083902-1 to 083902-4 (2003).

[44] Z. Deng, D.-K. Qing, P. Hemmer, C. H. R. Ooi, M. S. Zubairy and M. O. Scully, "Time-Bandwidth Problem in Room Temperature Slow Light", Phys. Rev. Lett., **96**, 023602-1 to 023602-4 (2006).

[45] A. Shumelyuk, K. Shcherbin, S. Odoulov, B. Sturman, E. Podivilov and K. Buse, "Slowing Down of Light in Photorefractive Crystals with Beam Intensity Coupling Reduced to Zero", Phys. Rev. Lett., **93**, 243604-1 to 243604-4 (2004).

[46] H. N. Yum, M. Salik, G. S. Pati, S. Tseng, P.R. Hemmer and M. S. Shahriar, "Fast-light in a photorefractive crystal for gravitational wave detection", Opt. Express, **16**, 20448-20456 (2008).

[47] T. Y. Chang, R.W. Hellwarth, "Optical phase conjugation by backscattering in barium titanate", Opt. Lett., **10**, 408-410 (1985).

[48] J. Feinberg, D. Heiman, A. R. Tanguay and R. W. Hellwarth, "Photorefractive effects and light-induced charge migration in barium titanate", J. of Appl. Phys., **51**, 1297-1305 (1980).

[49] C. Yang, Y. Zhang, P. Yeh, Y. Zhu and X. Wu, "Photorefractive properties of Ce:$BaTiO_3$ crystals", Opt. comm., **113** , 416-420 (1995).

[50] W. F. Zhang, Y. B. Huang, M. S. Zhang, and Z. G. Liu, "Nonlinear optical absorption in undoped and cerium-doped $BaTiO_3$ thin films using Z-scan technique", Appl. Phys. Lett., **76**, 1003-1005 (2000).

[51] Y. Liu, Z. Chen, C. Li, D. Cui, Y. Zhou, G. Yang and Y. Zhu, "Electrical and electro-optical properties of Ce-doped barium titanate thin films prepared by pulsed laser deposition", J. Appl. Phys., **81**, 6328-6331 (1997).

[52] G. Yang, H. Wang, G. Tan, A. Jiang, Y. Zhou, Z. Chen, "Rh:$BaTiO_3$ Thin Films with Large Nonlinear Optical Properties", Appl. Opt., **41**, 1729-1732 (2002).

[53] C. H. Perry and D. B. Hall, "Temperature dependence of the Raman spectrum of $BaTiO_3$", Phy. Rev. Lett., **15**, 700-702 (1965).

[54] M. El Marssi, F. Le Marrec, I. A. Lukyanchuk, and M. G. Karkut, "Ferroelectric transition in an epitaxial barium titanate thin film: Raman spectroscopy and X-ray diffraction study", J. of App. Phys., **94**, 3307-3312 (2003).

[55] U. M. Pasha, H. Zheng, O. P. Thakur, A. Feteira, K. R. Whittle, D. C. Sinclair, and I. M. Reaney, "*In situ* Raman spectroscopy of *A*-site doped barium titanate", Appl. Phys. Lett., **91**, 062908 -1 to 062908-3 (2007).

[56] D. J. Gauthier, and A. E. Willner, “Fiber-Based Slow-Light Technologies”, J. of Light wave Tech., **26**, 3752-3762 (2008).

[57] A. Andre, M. D. Eisaman, R. L. Walsworth, A. S. Zibrov and M. D. Lukin, “Quantum control of light using electromagnetically induced transparency”, J. Phys. B: At. Mol. Opt. Phys., **38,** S589–S604 (2005).

[58] A. S. Zibrov, M. D. Lukin and M. O. Sully, “Non-degenerate parametric self-oscillations via multiwave mixing in coherent atomic media”, Phys. Rev. Lett., **83**, 4049-4052 (1999).

[59] P. W. Milonni, “Fast Light, Slow Light and Left-Handed Light”, Series in Optics and Optoelectronics (Institute of Physics Publishing Bristol and Philadelphia ISBN 0 7503 0926 1) (2005).

[60] A. Peng, M. Johnsson, W. P. Bowen, P. K. Lam, H.-A. Bachor, and J. J. Hope, “Squeezing and entanglement delay using slow light”, Phys. Rev. A, **71**, 033809-1 – 033809-5 (2005).

[61] C. Liu, Z. Dutton, C.H. Behroozi, L.V. Hau, “Observation of coherent optical information storage in an atomic medium using halted light pulses”, Nature, **409**, 490-493 (2001).

[62] D. F. Phillips, A. Fleischhauer, A. Mair, R. L. Walsworth, M. D. Lukin, “Storage of light in atomic vapor”, Phys. Rev. Lett., **86**, 783-786 (2001).

[63] S. E. Harris, “Electromagnetically induced transparency”, Phys. Today, **50**, 36-42 (1997).

[64] K.-J. Boller, A. Imamoglu, and S. E. Harris, “Observation of electromagnetically induced transparency”, Phys. Rev. Lett., **66**, 2593-2596 (1991).

[65] H. Schmidt and A. Imamoglu, “Giant Kerr nonlinearities obtained by electromagnetically induced transparency”, Opt. Lett., **21**, 1936-1938 (1996).

[66] M. D. Lukin and A. Imamoglu, “Controlling photons using electromagnetically induced transparency”, Nature, **413**, 273-276 (2001).

[67] A. K. Patnaik, J. Q. Liang, and K. Hakuta, “Slow light propagation in a thin optical fiber via electromagnetically induced transparency”, Phys. Rev. A, **66**, 063808-1 to 063808-10 (2002).

[68] K. Y. Song, M. G. Herráez and L. Thévenaz, “Observation of pulse delaying and advancement in optical fibers using stimulated Brillouin scattering”, Opt. Express, **13**, 82-88 (2005).

[69] Z. Zhu, D. J. Gauthier, Y. Okawachi, J. E. Sharping, A. L. Gaeta, R. W. Boyd and A. E. Willner, “Numerical study of all-optical slow-light delays via

stimulated brillouin scattering in an optical fiber", J. Opt. Soc. Am. B, **22**, 2378-2384 (2005).

[70] Z. Zhu, D. J. Gauthier, "Nearly transparent SBS slow light in an optical fiber", Opt. Express, **14**, 7238-7245 (2006).

[71] Y. Okawachi, M. S. Bigelow, J. E. Sharping, Z. Zhu, A. Schweinsberg, D. J. Gauthier, R. W. Boyd and A. L. Gaeta, "Tunable all-optical delays via brillouin slow light in an optical fibre", Phys. Rev. Lett., **94**, 153902-1 to 153902-4, (2005).

[72] K. Y. Song, M. G. Herraez and L. Thevenaz, "Long optically controlled delays in optical fibres", Opt. Lett., **30**, 1782-1784 (2005).

[73] A. Minardo, R. Bernini, and L. Zeni, "Low distortion brillouin slow light in optical fibres using AM modulation", Opt. Express, **14**, 5866-5876 (2006).

[74] Z. Lu, Y. Dong, and Q. Li, "Slow light in multi-line brillouin gain spectrum", Opt. Express, **15**, 1871-1877 (2007).

[75] A. Zadok, A. Eyal, and M. Tur, "Extended delay of broadband signals in stimulated Brillouin scattering slow light using synthesized pump chirp", Opt. Express, **14**, 8498-8505 (2006).

[76] T. Schneider, R. Henker, K.-U. Lauterbach, and M. Junker, "Comparison of delay enhancement mechanisms for SBS-based slow light systems", Opt. Express, **15**, 9606-9613 (2007).

[77] M. G. Herráez, K. Y. Song and L. Thévenaz, "Arbitrary-bandwidth Brillouin slow light in optical fibers", Opt. Express, **14**, 1395-1400 (2006).

[78] K. Y. Song and K. Hotate, "25 GHz bandwidth Brillouin slow light in optical fibers", Opt. Lett., **32**, 217-219 (2007).

[79] L. Yi, L. Zhan, W. Hu, and Y. Xia, "Delay of Broadband Signals Using Slow Light in Stimulated Brillouin Scattering With Phase-Modulated Pump", IEEE photon technol. Lett., **19**, 619-621 (2007).

[80] D. Dahan and G. Eisenstein "Tunable all optical delay via slow and fast light propagation in a Raman assisted fiber optical parametric amplifier: a route to all optical buffering", Opt. Express, **13**, 6234-6249 (2005).

[81] K. Lee and N. M. Lawandy, "Optically induced pulse delay in a solid-state Raman amplifier", App. Phy. Lett., **78**, 703-705 (2001).

[82] Y. A. Vlasov, M. O'Boyle, H. F. Hamann and S. J. McNab, "Active control of slow light on a chip with photonic crystal waveguides", Nature, **438**, 65-69 (2005).

[83] J. P. Hugonin, P. Lalanne, T. P. White, and T. F. Krauss, “Coupling into slow-mode photonic crystal waveguides”, Opt. Lett., **32**, 2638-2640 (2007).

[84] F. Bo, G. Zhang, and J. Xu, “Ultraslow Gaussian pulse propagation induced by a dispersive phase coupling in photorefractive bismuth silicon oxide crystals at room temperature”, Opt. Comm., **261**, 349-352 (2006).

[85] F. Bo, G. Zhang and J. Xu, “Transition between superluminal and subluminal light propagation in photorefractive $Bi_{12}SiO_{20}$ crystals”, Opt. Express, **13**, 8198-8203 (2005).

[86] Z. Guo-Quan, D. Rong and Xu. Jing-Jun, “Group Velocity Reduction of Light Pulses in Photorefractive Two-Wave Mixing”, Chin. Phys. Lett., **20**, 1725-1728 (2003).

[87] G. Zhang, R. Dong, F. Bo, and J. Xu, “Slowdown of group velocity of light by means of phase coupling in photorefractive two-wave mixing”, Appl. Opt., **43**, 1167-1173 (2004).

[88] G. Zhang, F. Bo, R. Dong, and J. Xu, “Phase-Coupling-Induced Ultraslow Light Propagation in Solids at Room Temperature”, Phys. Rev. Lett., **93**, 133903-1 to 133903-4 (2004).

[89] P.-C. Ku, F. Sedgwick, C. J. Chang-Hasnain, P. Palinginis, T. Li, H. Wang, S.-W. Chang, and S.-L. Chuang, “Slow light in semiconductor quantum wells”, Opt. Lett., **29**, 2291-2293 (2004).

[90] P. Palinginis, F. Sedgwick, S. Crankshaw, M. Moewe, and C. J. Chang-Hasnain, “Room temperature slow light in a quantum well via coherent population oscillations”, Opt. Express, **13**, 9909-9915 (2005).

[91] B. Macke, and B. Segard, “Slow light in saturable absorbers”, Phys. Rev. A, **78**, 013817-1 to 013817-7 (2008).

[92] A. C. Selden, “Slow light and saturable absorption”, Opt. & Spectrosc., **106**, 881–888 (2009).

[93] V. S. Zapasskiĭ, and G. G. Kozlov, “A saturable absorber, coherent population oscillations and slow light”, Opt. & Spectrosc., **100**, 419–424 (2006).

[94] S. E. Schwarz, and T. Y. Tan, “Wave interactions in saturable absorbers,” Appl. Phys. Lett., **10**, 4–7 (1967).

[95] P. Agruzov, A. Shamray, M. O. Miramontes, E. H. Herna´ndez, and S. Stepanov, “Slow light propagation via saturable absorption of acetylene in hollow-core photonic crystal fiber”, Appl. Phys. B, **108**, 827–832 (2012).

[96] A C. Selden, “Pulse transmission through a saturable absorber”, Br. J. Appl. Phys., **18**, 743–748 (1967).

[97] A. C. Selden, "Analysis of the saturable absorber transmission equation", J. Phys. D Appl. Phys. **3**, 1935–1943 (1970).

[98] A. Khare, "Pulsed resonance saturation spectroscopy for plasma diagnostic", Rev. Sci. Instrum., **67**, 3530-3532 (1996).

[99] L. V. Hau, S. E. Harris, Z. Dutton, C. H. Behroozi, "Light speed reduction to 17 meters per second in an ultra-cold atomic gas", Nature, **397**, 594-598 (1999).

[100] A. V. Turukhin, V. S. Sudarshanam, M. S. Shahriar, J. A. Musser, B. S. Ham, P. R. Hemmer, "observation of ultra-slow and stored light pulses in a solid", Phys. Rev. Lett., **88**, 023602-1 to 023602-4 (2002).

[101] W. Horn, J. V. Bassewitz and C. Denz, "Slow and fast light in photorefractive SBN:60", J. Opt., **12**, 104011-1 to 104011-4 (2010).

[102] P. Yeh, "Two-wave mixing in nonlinear media", IEEE J. of Q. Elec., **25**, 484-519 (1989).

[103] M. Chi., J. P. Huignard, and P. M. Petersen, "A general theory of two-wave mixing in nonlinear media", JOSA B, **26**, 1578-1584 (2009).

[104] P. Stojkov, D. Timotijevi and M. Beli, "Symmetries of two-wave mixing in photorefractive crystals", Opt. Lett., **17**, 1406-1408 (1992).

[105] Ph. Refregier, L. Solymar, H. Rajbenbach, and J. P. Huignard, "Two beam coupling in photorefractive Bi12SiO20 crystal with moving grating: Theory and experiment", J. Appl. Phys., **58**, 45-57 (1985).

[106] N. Koukourakis, T. Abdelwahab, M. Y. Li, H. Höpfner, Y. W. Lai, E. Darakis, C. Brenner, N. C. Gerhardt, and M. R.Hofmann, "Photorefractive two-wave mixing for image amplification in digital holography", Opt. Express, **19**, 22004-22023 (2011).

[107] L. Solymar, D. J. Webb, and A. Grunnet-Jepsen, "The Physics and Applications of Photorefractive Materials", (Clarendon, Oxford, 1996).

[108] P. Yeh, "Introduction to photorefractive optics", (New York: Wiley, 1993).

[109] Ph. Mauron, M. Bielmann, V. Bissig, A. Remhof and A. Zuttel, "High-pressure and high-temperature differential scanning calorimeter for combined pressure-concentration-temperature measurements of hydrides", Rev. Sci. Instrum., **80**, 095113-1 to 095113-6 (2009).

[110] M. Hoummady and D. Hauden, "Acoustic wave thermal sensitivity: temperature sensors and temperature compensation in micro sensor", Sensors & Actuators A, **44**, 177-182 (1994).

[111] J. D. N. Cheeke, C. Neron, A. Brunelle, "Gallium arsenide phosphide light-emitting diodes as general thermometers above 35 K", Rev. Sci. Instrum., **54**, 900-902 (1983).

[112] V. Chopra, G. Dharmadurai, "Effect of current on the low temperature characteristics of diode sensors", Cryogenics, **20**, 659-662 (1980).

[113] B. F. Griffing and S. A. Shivashankar, "Use of light-emitting diodes as temperature sensors", Rev. Sci. Instrum. **48**, 1225 (1977).

[114] M. Nakazawa, H. Ito, A. Usui, A. Ballato and T. Lu-kaszeck, "New quartz resonators with precision frequency linearity over a wide temperature range", proc 36th AFCS, 290-296 (1982).

[115] D. I. Forsyth, T. Sun, K. T. V. Grattan, S. A. Wade and S. F. Collins, "Characteristic of doped optical fiber for fluorescence–based fiber optics temperature systems", Rev. Sci. Instrum., **74**, 5212-5218 (2003).

[116] K. T. V. Grattan and Z. Y. Zhang, "Fibre optic fluorescence thermometry", (chapman and Hall, London, 1995).

[117] K. T. V. Grattan and T. Sun, "Fiber optic sensor technology: an overview", Sensor & Actuators, **82**, 40-61 (2000).

[118] R. M. Measures, "Structural monitoring with fibre optic technology", (Academic, San, Diego, CA, 2001), 369-449.

[119] A. Othonos and K. Kalli, "Fibre Bragg Gratings: Fundamantals ans Applications in Telecommunications and Sensing", (Artech Hoer, Boston, MA, 1999), 98-140.

[120] E. Li, X. Wang, and C. Zhang, "Fiber-optic temperature sensor based on interference of selective higher order modes", Appl. Phys. Lett., **89**, 091119-1 - 091119-4 (2006).

[121] D. Hwang, D-J. Y, Il-B. K, D-C. Seo, and Y. Chung, "Novel auto-correction method in a fiber-optics distributed temperature sensor using reflected anti-stokes Raman scattering", Opt. Express, **18**, 9747-9754 (2010).

[122] H. Guo, F. Pang, X. Zeng, Na. Chen, Z. Chen, and T. Wang, "Temperature sensor using an optical fiber couples with a thin film", Appl. Opt., **47**, 3530-3534 (2008).

[123] K. T. V. Grattan, R. K. Selli, and A.W. Palmer, "Ruby fluorescence wavelength division fiber optics temperature sensor", Rev. Sci. Instrum., **58,** 1231-1234 (1987).

[124] H. Aizawa, N. Ohishi, S. Ogawa, T. Katsumata, S. Komuro, T. Morikawa and E. Toba, "Fabrication of ruby sensor probe for the fiber-optic thermometer using fluorescence decay", Rev. Sci. Instrum., **73**, 3656-3658 (2002).

[125] I. Kamma, P. Kommidi and B. R. Reddy, "Design of a high temperature sensing systems using luminescence lifetime measurement", Rev. Sci. Instrum., **79**, 096104-1 to 096104-3 (2008).

[126] A. L. Schawlow, Advances in quantum Electronics, edited by J. R. Singer (Columbia University Press, New York, 1961).

[127] T. -H. Huang, C.-C. Hsu, C.-T. Kuo, P.Lu, W.-S. Tse, D.P. Wang, T.C. Chou and A.Y.G.Fuh, "Ruby spectral band- profile analysis for temperature sensing", J. Appl. Phys., **75**, 3599-3606 (1994).

[128] N. Yu, Q. Wen, D. R. Clarke, P. C. McIntyre, H. Kung, M.Nastasi, T. W. Simpson, I. V. Mitchell and D. Li, "Formation of iron or chromium doped epitaxial sapphire thin films on sapphire substrates", J. Appl. Phys., **78**, 5412 –5421 (1995).

[129] Q. Wen, D. R. Clarke, N. Yu and M. Nastasi, "Epitaxial growth of ruby on sapphire for an integrated thin film stress sensor", Appl. Phys. Lett., **66**, 293-295 (1995).

[130] C. Pflitsch, D. Viefhaus, B. Atakan, "CVD of Thin Ruby Films on Si(100) and Stainless Steel for Surface Temperature Sensor Applications", Chem. Vap. Depo., **13**, 420 – 426 (2007).

[131] H. Aizawa, M. Shibasaki, S.Komuro, Y. Miyazaki and T. Katsumata, "Fabrication of ruby thin film for temperature indicator application", Int. Conference., On Electrical Engineering, (2009).

[132] J. Gonzalo, R. G. San Román, J. Perrière, C.N. Afonso and R. P.Casero, "Pressure effects during pulsed-laser deposition of barium titanate thin films", Appl. Phys. A Mat. Sci. & Process., **66**, 487-491 (1998).

[133] M. E. Marssi, F. L. Marrec, I. A. Lukyanchuk and M. G. Karkut, "Ferroelectric transition in an epitaxial barium titanate thin film: Raman spectroscopy and X-ray diffraction study", J. Appl. Phys., **94**, 3307-3312 (2003).

[134] G. Yang, H. Wang, G. Tan, A. Jiang, Y. Zhou, Z. Chen, "Rh:$BaTiO_3$ Thin Films with Large Nonlinear Optical Properties", Appl. Opt., **41**, 1729-1732 (2002).

[135] W. Wei-Tian, Y. Guang, D. Ping, Z. Yue-Liang and C. Zheng-Hao, "Fe-doped $BaTiO_3$ thin films with large third-order nonlinear optical susceptibility", Chin. Phys. Let., **19**, 1122-1124 (2002).

[136] G. Yang, W. Wang, L. Yan, H. Lu, G. Yang, Z. Chen, "Z-scan determination of the large third-order optical nonlinearity of Rh:$BaTiO_3$ thin films deposited on MgO substrates", Opt. Comm., **209**, 445-449 (2002).

[137] Y. Nakata, G. Soumagne, T. Okada, M. Maeda, "Pulsed-laser deposition of barium titanate films and plume dynamics", Appl. Surf. Sci., **127-129**, 650-654 (1998).

[138] W. Shi, Z. Chen, N. Liu, H. Lu, Y. Zhou, D. Cui, and G. Yang, "Nonlinear optical properties of self-organized complex oxide Ce:$BaTiO_3$ quantum dots grown by pulsed laser deposition", Appl. Phy. Lett., **75**, 1547-1549 (1999).

[139] W. F. Zhang, Y. B. Huang, M. S. Zhang, and Z. G. Liu, "Nonlinear optical absorption in undoped and cerium-doped $BaTiO_3$ thin films using Z-scan technique", Appl. Phys. Lett., **76**, 1003-1005 (2000).

[140] Y. Liu, Z. Chen, C. Li, D. Cui, Y. Zhou, G. Yang and Y. Zhu, "Electrical and electro-optical properties of Ce-doped barium titanate thin films prepared by pulsed laser deposition", J. Appl. Phys., **81**, 6328-6331 (1997).

[141] D. Roy and S. B. Krupanidhi, "Pulsed excimer laser ablated barium titanate thin films", Appl. Phys. Lett., **61**, 2057-2059 (1992).

[142] D. Kan and Y. Shimakawa, "Controlled cation stoichiometry in pulsed laser deposition-grown $BaTiO_3$ epitaxial thin films with laser fluence", Appl. Phys. Lett., **99**, 081907-1 to 081907-3 (2011)

[143] T. García, P. Bartolo-Pérez, E. de Posada, J. L. Peña and M. Villagrán-Muniz, "Studies of Pulsed Laser Deposition Processes of $BaTiO_3$ Thin Films", Surf. and Coat.Tech., **201**, 3621-3624 (2006).

[144] C. H. Lei, "The Growth of $BaTiO_3$ Films on (001) $MgAl_2O_4$ Substrates by Pulsed Laser Deposition Technique", Thin Solid Films, **515**, 1701-1707 (2006).

[145] A. Husmann, M. Mertin, T. Klotzbücher and E. W. Kreutz, "Deposition of $BaTiO_3$ Thin Films by a Hybrid DC-Field Enhanced PLD-Process", Appl. Surf. Sci., **109/110**, 293-298 (1997).

[146] M. N. R. Ashfold, F. Claeyssens, G. M. Fuge, and S. J. Henley, "Pulsed laser ablation and deposition of thin films", Chem. Soc. Rev., **33**, 23-31 (2004).

[147] R. D. Vispute, S. Choopon, R. Enck, A. Patel, V. Talyansky, R. P. Sharma, T. Venkatesan, W. L. Sarney, L. Salamancariba, S. N. Andronescu, A. A. Iliadis and K. A. Jones, "Pulsed laser deposition and processing of wide band gap semiconductors and related materials", J. Elec. Res., **28**, 275-286 (1999).

[148] S. S. Thöny, K. E. Youden, J. S. Harris, Jr., and L. Hesselink, "Growth of epitaxial strontium barium niobate thin films by pulsed laser deposition", Appl. Phys. Lett., **65**, 2018-2020 (1994).

[149] C. Hrisey, D. B., and Hubler, G.K., (Eds.),"Pulsed Laser Deposition of Thin Films", Wiley-Interscience, New York. (1994).

[150] H. M Christen and G Eres, "Recent advances in pulsed-laser deposition of complex oxides", J. Phys.: Cond. Mat., **20,** 264005-1 to 264005-16 (2008).

[151] R. W. Eason, "Pulsed Laser Deposition of Thin Films", John Wiley & Sons, New York, 2007.

[152] M. von Allmen, A. Blatter, "Laser-Beam Interactions with Materials", Springer-Verlag, Berlin, 1995.

[153] J. C. Miller (editor), "Laser Ablation - Principles and Applications", Springer-Verlag, Berlin, 1994.

[154] T. Katase, H. Hiramatsu, T. Kamiya and H. Hosono, "Thin film growth by pulsed laser deposition and properties of 122-type iron-based superconductor AE$(Fe_{1-x}Co_x)_2As_2$ (AE=alkaline earth)", Supercond. Sci. Tech., **25**, 084015-1 to 084015-12 (2012).

[155] A. Luches and A. P. Caricato, "Matrix assisted pulsed laser evaporation: the surface cluster problem", Appl. Phy. B, **105**, 503–508 (2011).

[156] R. Teghil, A. De Bonis, A. Galasso, M. Sansone, J. V. Rau, A. Santagata, "Nanostructured molybdenum carbide thin films obtained by femtosecond pulsed laser deposition", Physica status solidi (c), **9**, 2370-2373 (2012).

[157] X. Y. Zhang, C. K. Ong, S. Y. Xu and H. C. Fang, "Observation of Growth Morphology in Pulsed-Laser Deposited Barium Ferrite Thin Films", Appl. Surf. Sci., **143**, 323-327 (1999).

[158] Transparent Conducting Oxide Thin Films. "Pulsed Laser Deposition of Thin Films" Ed. R. Eason. Wiley-Interscience, 239-260 (2007).

[159] H. M. Smith, and A. F. Turner, "Vacuum deposited thin films using a ruby laser", Appl. Opt., **4**, 147-148 (1965).

[160] R. G. Ross, P. Chaudhari, M. Kawasaki, M. B. Ketchen, and A. Gupta, " Low noise $YBa_2Cu_3O_{7-\delta}$ grain boundary junction dc SQUIDs", Appl. Phys. Lett., **57**, 727-729 (1990).

[161] C. Kwon, Q. Li , X. X. Xi, S. Bhattacharya, C. Doughty, T. Venkatesan, H. Zhang, J. W. Lynn, J. L. Peng, Z. Y. Li, N. D. Spencer, K. Feldman, "High critical current densities in ultrathin $YBa_2Cu_3O_{7-\delta}$ films sandwiched between $(Pr_xY_{1-x})Ba_2Cu_3O_{7-\delta}$ layers", Appl. Phys. Lett., **62**, 1289-1291 (1993).

[162] M. Liu, J. Liu, G. Collins, C. R. Ma, C. L. Chen, J. He, J. C. Jiang, E. L. Meletis, A. J. Jacobson and Q. Y. Zhang, "Magnetic and transport properties of epitaxial $(LaBa)Co_2O_{5.5+\delta}$ thin films on (001) $SrTiO_3$", Appl. Phys. Lett., **96**, 132106-1 to 132106-3 (2010).

[163] Y. H. Ou, Z. Huang, Y. Gao, Y. Ge, J. Wu, and J. Chu, “Characterization of $Mn_{1.56}Co_{0.96}Ni_{0.48}O_4$ films for infrared detection”, Appl. Phys. Lett., **92**, 202115-1 to 202115-3 (2008).

[164] P. R. Wilmott, P. Manoravi, and K. Holiday, “Production and characterization of Nd,Cr:GSGG thin films on Si(001) grown by pulsed laser ablation”, Appl. Phys. A, **70**, 425-429 (2000).

[165] M. P. Singh, K. D. Truong, S. Jandl, and P. Fournier, “Stabilization and functional properties of $La_3NiAlMnO_9$ and $La_3CoAlMnO_9$ magnetoelectric triple perovskites”, Appl. Phys. Lett., **94**, 171908-1 to 171908-3 (2009).

[166] D. Roy and S. B. Krupanidhi, “Pulsed excimer laser ablated barium titanate thin films”, Appl. Phys. Lett., **61**, 2057-2059 (1992).

[167] A. Gupta, G. Koren, C. C. Tsuei, A. Segmuller, and T. R. Mcguire, “Deposition of epitaxial thin films of Nd1.85Ce0.15CuO4−y by laser ablation”, Appl. Phys. Lett., **55**, 1795-1797 (1989).

[168] L. Wiedeman, and H. Helvajian, “Laser photodecomposition of sintered $YBa_2Cu_3O_{6+x}$: Ejected species population distributions and initial kinetic energies for the laser ablation wavelengths 351, 248, and 193 nm”, J. Appl. Phys., **70**, 4513-4523 (1991).

[169] W. Demtroder, and W. Jantz, “Investigation of laser-produced plasmas from metal-surfaces”, Plasma Physics, **12**, 691-703 (1970).

[170] J. Gonzalo, R. G. San Román, J. Perrière, C. N. Afonso and R. P. Casero, “Pressure effects during pulsed-laser deposition of barium titanate thin films”, Appl. Phys. A Mat. Sci. & Process., **66**, 487-491 (1998).

[171] A. A. Anderson, R. W. Eason, M. Jelinek, C. Grivas, D. Lane, K. Rogers, L.M.B. Hickey, C.Fotakis, “Growth of Ti:sapphire single crystal thin films by pulsed laser deposition”, Thin Solid Films, **300**, 68-71 (1997).

[172] R. I. Tomov, T. K. Kabadjova, P. A. Atanasov, S. Tonchev, M. Kaneva, A. Zherikhin, R. W. Eason, “$LiNbO_3$ optical waveguides deposited on sapphire by electric-field-assisted pulsed laser deposition”, Vacuum, **58** , 396-403 (2000).

[173] SeeHyung Lee, T. W. Noh, and JaiHyung Lee, “Control of epitaxial growth of pulsed laser deposited LiNbO3 films and their electrooptic effects”, Appl. Phys. Lett., **68**, 472-474 (1996).

[174] W. Wei-Tian, Y. Guang, D. Ping, Z. Yue-Liang and C. Zheng-Hao, “Fe-doped $BaTiO_3$ Thin Films with Large Third-Order Nonlinear Optical Susceptibility”, Chin. Phys. Let, **19**, 1122-1124 (2002).

[175] A. M. Marsh, S. D. Harkness, F. Qian, and R. K. Singh, "Pulsed laser deposition of high quality $LiNbO_3$ films on sapphire substrates", Appl. Phys. Lett., **62**, 952-954 (1993).

[176] SeeHyung Lee, T. K. Song, T. W. Noh, and JaiHyung Lee,"Low temperature growth of epitaxial LiNbO3 films on sapphire (0001) substrate using pulsed laser deposition", Appl. Phys. Lett., **69**, 1541 (1996).

[177] S. Amoruso, R. Bruzzese , N. Spinelli and R. Velotta, "Characterization of laser-ablation plasmas", J. Phys. B: At. Mol. Opt. Phys., **32,** R131–R172 (1999).

[178] K. J. Saji, N. V. Joshy, and M. K. Jayaraj, "Optical emission spectroscopic studies on laser ablated zinc oxide plasma", J. Appl. Phys., **100**, 043302-1 to 043302-5 (2006).

[179] K. F. Al-Shboul, S. S. Harilal, A. Hassanein, and M. Polek, "Dynamics of C_2 formation in laser–produced carbon plasma in helium environment", J. Appl. Phys., **109**, 053302-1 to 053302-6 (2011).

[180] E. Camps, L. Escobar-Alarcon, V. H. Castrejon- Sanchez, M. A. Camacho-Lopez, and S. Muhl, "Characterization of the laser ablation plasma used for the deposition of amorphous carbon", Appl. Surf. Sci., **254**, 185-188 (2007).

[181] M. Esposito, T. Lippert, C. W. Schneider, A. Wokaun, T. Donnelly, J. G. Lunney, H. Tellez, J. M. Vadillo and J. J. Laserna, "Pulsed laser ablation of silver: ion dynamics in the plasma plume", J. Opt. Adv. Mater., **12**, 677-680 (2010).

[182] S. M. Park and J. Y. Moon, "Laser ablation of graphite in an oxygen jet", J. Chem. Phys., **109**, 8124-8129 (1998).

[183] S. S. Harilal, C. V. Bindhu, M. S. Tillack, F. Najmabadi, and A. C. Gaeris, "Internal structure and expansion dynamics of laser ablation plumes into ambient gases", J. Appl. Phys., **93**, 2380-2388 (2003).

[184] S. S. Harilal, C. V. Bindhu, R. C. Issac, V.P.N. Nampoori, and C. P. G. Vallabhan, "Electron density and temperature measurement in a laser produced carbon plasma", J. Appl. Phys., **82**, 2140-2146 (1997).

[185] J. G. Lunney, B. Doggett and Y. Kaufman, "Langmuir probe diagnosis of laser ablation plasmas", J. Phys. Conference Series, **59**, 470-474 (2007).

[186] B. Toftmann, J. Schou , T. N. Hansen and J. G. Lunney, "Angular Distribution of Electron Temperature and Density in a Laser-Ablation Plume", Phys. Rev. Lett., **84**, 3998-4001 (2000).

[187] B. Doggett, C. B. Joergensen, J. G. Lunney, P. Sheerin and M. M. Turner, "Behaviour of a planar Langmuir probe in a laser ablation plasma", Appl. Surf. Sci., **247**, 134-138 (2005).

[188] A. H. Dogar, B. Ilyas, S. Ullah, A. Nadeem, and A. Qayyum, "Langmuir Probe Measurements of Nd:YAG Laser-Produced Copper Plasmas", IEEE Trans. on Plas. Sci., **39**, 897-900 (2011).

[189] B. Doggett and J. G. Lunney, "Langmuir probe characterization of laser ablation plasmas", J. Appl. Phys., **105**, 033306-1 to 033306-6 (2009).

[190] R. C. Issac, P. Gopinath, G. K. Varier, V. P. N. Nampoori and C. P. G. Vallabhan, "Twin peak distribution of electron emission profile and impact ionization of ambient molecules during laser ablation of silver target", Appl. Phys. Lett., **73**, 163-165 (1998).

[191] N. V. Joshy and M. K. Jayaraj, "Spatial investigation of ion and electron time of flight in laser ablated ZnO plasma", J. Phys. Conference series, **208**, 012131-1 to 012131-8 (2010).

[192] J. Wild, P. Kudrna, T. Gronych, J. Broz, Z. Zelinger, P. Kubat and S. Civis, "Langmuir probe measurement of plasma splitting during pulsed laser deposition", Rev. Sci. Instrum., **72,** 1597-1599 (2001).

[193] R. Swanepoel, "Determination of the thickness and optical constants of amorphous silicon," J. Phps. E: Sci. Instrum., **16**, 1214-1222 (1983).

[194] M. Sheik-Bahae, A. A. Said, T. Wei, D. Hagan, and E.W. Van Stryland, "Sensitive measurement of optical nonlinearities using a single beam", IEEE J. Quantum Electron., **26**, 760-769 (1990).

[195] F. Z. Henari , K. Morgenstern, W. J. Blau V. A. Karavanskii and V. S. Dneprovskii, "Third order nonlinearity and all optical switching in porous silicon", Appl. Phys. Lett., **67**, 323-325 (1995).

[196] D. Qu, R. Guo, S. Liu, Z. Liu, and Y. Gao, "Simple optical method for determination of crystal orientation in photorefractive crystals", Appl. Opt., **45**, 6218-6222 (2006).

[197] R W. Boyd, Nonlinear Optics (Elsevier, second edition 2003), **Chap.11**

[198] S. S. Harilal, C. V. Bindhu, V.P.N. Nampoori, & C. P. G. Vallabhan, "Influence of ambient gas on the temperature and density of laser produced carbon plasma", App. Phys. Lett., **72**, 167-169 (1998).

[199] H. Aizawa, K. Ito, S. Takahashi, S. Komuro, Y. Miyazaki and T. Katsumata, "Fabrication of Ruby thin film for temperature indicator application", ICROS-SICE International joint conference (2009).

[200] A. R. Zanatta, C. T. M. Ribeiro, U. Jahn, S. B. Aldabergenova and H. P. Strunk, "Thermally synthesized ruby microstructures and luminescence centers", J. Appl. Phys., **100**, 113112-1 - 113112-7 (2006).

[201] A. Aminzadeh and H. Sarikhani-fard, “Raman spectroscopic study of Ni/Al_2O_3 catalyst”, Spectrochimica Acta. Part A, **55**, 1421- 1425 (1999).

[202] S.-H. Shim, T. S. Duffy, R. Jeanloz, C.-S. Yoo and V. Iota, “Raman spectroscopy and x-ray diffraction of phase transitions in Cr_2O_3 to 61 GPa”, Phys. Rev. B, **69**, 144107-1 - 144107-12 (2004).

[203] M Kadleikova, J. Breza and M. Vesely, “Raman spectra of synthetic sapphire”, Microelectronics journal, **32**, 955-958 (2001).

[204] S. P. S. Poroto and R. S. Krishnan, “Raman Effect of Corundum”, J. Chem. Phys., **47**, 1009-1012 (1967).

[205] H. Yao, C. H. Yan, S. P. Denbaars and J. M. Zavada, “Optical Anisotropy Studies of Sapphire by Raman Scattering and Spectroscopic Transmission Ellipsometry”, Mat. Res. Soc. Symp. Proc., **512**, 411-416 (1998).

[206] A. Lorusso, V. Fasano, A. Perrone, and K. Lovchinov, “Y thin film grown by pulsed laser ablation”, J. Vac. Sci. Technol. A, **29**, 031502-1 - 031502-5 (2011).

[207] V. Cracium, S. Amirhaghi, D. Cracium, J. Elders, J. G. E. Gardeniers, and I. W. Boyd, “Effect of laser wavelength and fluence on the growth of ZnO thin films by pulsed laser deposition”, Appl. Surf. Sci., **86**, 99-106 (1995).

[208] C. Wang, B. L. Cheng, S.Y. Wang, H. B. Lu, Y.L. Zhou, Z. H. Chen, and G. Z. Yang, “Effect of oxygen pressure on lattice parameter, orientation, surface morphology and deposition rate of $(Ba_{0.02}Sr_{0.98})TiO_3$ thin film grown on MgO substrate by pulsed laser deposition ”, Thin solid films, **485**, 82-89 (2005).

[209] X. J. Zhang, W. Ji, and S. H. Tang, “Determination of optical nonlinearities and carrier lifetime in ZnO”, J. Opt. Soc. Am. B, **14**, 1951-1995 (1997).

[210] V. Kumari, V. Kumar, B. P. Malik, D. Mohan, and R. M. Mehra, “Laser induced nonlinear optical properties of zinc oxide thin film prepared by sol-gel method”, J. Nano- Electron. Phys., **3**, 601-609 (2011).

[211] H. Liu and W. Jia, “Photoluminescence and fast nonlinear optical response of barium titanate crystals”, J. of Lumi., **76 & 77**, 100-103 (1998).

[212] P. Mathey, A. Dazzi, P. Jullien, D. Rytz, and P. Moretti, “Two-wave mixing at 854 nm in $BaTiO_3$:Rh planar waveguide implanted with He^+”, Opt. Mat., **18**, 69-71 (2001).

[213] L.- Z. Xuan, S.-H. Pan, Z.-H. Chen, R.-P. Wang, W.-S. Shi and C.-L. Li, “Second –harmonic generation in $BaTiO_3$ films doped with cerium”, Appl. Phys. Lett, **73**, 2896-2898 (1998).

[214] L. Huang, Z. Chen, J. D. Wilson, S. Banerjee, R. D. Robinson, I. P. Herman, R. Laibowitz and S. O’Brien,“Barium titanate nanocrystals and nanocrystal thin

films: synthesis, ferroelectricity, and dielectric properties", Journal of appl. Phys., **100**, 034316-1 to 034316-10 (2006).

[215] M.–S. Zhang, J. Yu, J. Chu, Q. Chen and W. Chen, "Microstructure and photoluminescence of barium titanate nanocrystals synthesized by the hydrothermal process", J. of Mat. Proc. Tech., **137**, 78-81 (2003).

[216] P. Ji-hua, L. Wen-Fang, H. Bing, H. Fang-Liang, and DU Jun, "Synthesis of tetragonal $BaTiO_3$ film on Ti substrate by micro-arc oxidation", Trans. Nonferrous Met. Soc. China, **18**, 1117-1121 (2008).

[217] H.-W. Lee, S. Moon, C.-H. Choi, and D. K. Kim, "Synthesis and Size Control of Tetragonal Barium Titanate Nanopowders by Facile Solvothermal Method", J. Am. Ceram. Soc., **95**, 2429–2434 (2012).

[218] D. A. Tenne and X. Xi, "Raman spectroscopy of ferroelectric thin film and superlattices", J. Am. Ceram. Soc., **91**, 1820-1834 (2008).

[219] L. Rimai, J. L. Parsons and J. T. Hickmott and T. Nakamura, "Raman spectrum of long-wavelength phonons in tetragonal barium titanate", Phy. Rev., **168**, 623-630 (1968).

[220] S. J. Lee, H. R. Yang, E. J. Kim, Y. L. Lee and C. H. Kwak, "Kinetics of two wave mixing gain for moving grating technique in photorefractive $BaTiO_3$ crystal", Opt. Express, **16**, 19615-19628 (2008).

[221] L. K. Lam, T. Y. Chang, J. Feinberg, and R. W. Hellwarth, "Photorefractive-index gratings formed by nanosecond optical pulses in $BaTiO_3$", Opt. Lett., **6**, 475-477 (1981).

[222] G. C. Valley, "Short-pulse grating formation in photorefractive materials", IEEE J. Quantum Electron., **19**, 1637-1645 (1983).

[223] A. Roy and K. Singh, "Cross and parallel polarization coupling in transmission-type degenerate four-wave mixing in compound semiconductor photorefractive crystal: Orientational dependence", J. Modern Opt., **41**, 987–1000 (1994).

[224] S. H. Lin, K. Y. Hsu, and P. Yeh, "Experimental observation of the slowdown of optical beams by a volume-index grating in a photorefractive $LiNbO_3$ crystal", Opt. Lett., **25**, 1582–1584 (2000).

[225] F. Gao, J. Xu, H. Qiao, Q. Wu, Y. Xu, and G. Zhang, "Observation of superluminal and slowdown light propagation in doped lithium niobate crystals", Opt. Comm., **257**, 185-190 (2006).

[226] J. Joseph, K. Singh, and P. K. C. Pillai, "Crystal orientation dependence of the SNR for signal beam amplification in photorefractive $BaTiO_3$", Opt. & Laser Tech., **23**, 237-240 (1991).

[227] M. R. Belic, D. Timotijevic, M. Petrovic, and M. V. Jaric, "Exact solution to photorefractive two-wave mixing with arbitrary modulation depth", Opt. Comm., **123**, 201-206 (1996).

[228] W. Krolikowski, and M. Cronin-Golomb, "Photorefractive wave mixing with finite beams", Opt. Comm., **89**, 88-98 (1992).

[229] V. V. Shepelevich, N. N. Egorov, and V. Shepelevich, "Orientation and polarization effects of two-beam coupling in a cubic optically active photorefractive piezoelectric BSO crystal", J. Opt. Soc. Am. B, **11**, 1394-1402 (1994).

[230] C. T. Field and F. M. Davidson, "Photorefractive two-wave mixing in the presence of high –speed optical phase modulation", Appl. Opt., **32**, 5285-5298 (1993).

[231] F. Arrieta-Y´a˜nez, O. G Calder´on and S. Melle, "Slow and fast light based on coherent population oscillations in erbium-doped fibres", J. Opt., **12**, 104002-1 - 104002-6 (2010).

[232] M. Amemiya, "Pulse broadening due to higher order dispersion and its transmission limit", J. of Light wave Tech., **20**, 591-597 (2002).

[233] R. V. Nair and R. Vijaya, "Photonic crystal sensors: An overview", Progress in quantum electronics, **34**, 89-134 (2010).

[234] F. Berghmans, T. Geernaert, S. Sulejmani, H. Thienpont, G. V. Steenberge, B. V. Hoe, P. Dubruel, W. Urbanczyk, P. Mergo, D. J. Webb, K. Kalli, J. V. Roosbroeck, and K. Sugden, "Photonic crystal fiber Bragg gratingbased sensors – opportunities for applications in healthcare", SPIE-OSA-IEEE, **8311**, 831102-1 - 831102-10 (2011).

[235] X. Wang, X. Deng, H. Wen, and L. Li, "Phase transition and high dielectric constant of bulk dense nanograin barium titanate ceramics", Appl. Phys. Lett. **89**, 162902-1 - 162902-3 (2006).

List of publications

Referred Journals

1. **Satchi Kumari** and Alika Khare, "*Optical and Structural Characterization of Pulsed Laser Deposited Ruby Thin Films for Temperature Sensing Application*", Applied surface science **265**, 180– 186 (2013).
2. **Satchi Kumari** and Alika Khare, "*Effect of pump-probe polarization and crystal orientation on pulse propagation in Ce:BaTiO*$_3$ *via degenerate two wave mixing* IEEE", Journal of Quantum Electronics **48**, 1036-1039 (2012).
3. **Satchi Kumari** and Alika Khare,"*Determination of the crystallographic orientations of a Ce:BaTiO*$_3$ *crystal via backward two-wave mixing*", Journal of Optics **41**, 154-157 (2012).
4. **Satchi Kumari**, Archana Kushwaha and Alika Khare, "*Spatial distribution of electron temperature and Ion density in laser induced ruby* (Al_2O_3:Cr^{3+}) *plasma using Langmuir probe*", Journal of Instrumentation Science and Technology, **7**, C05017 (2012).
5. **Satchi Kumari** and Alika Khare, "*Effect of pump intensity on slowing down of light in Ce:BaTiO*$_3$ *crystal via Degenerate Two-Wave mixing using chopped pulses*", IEEE Journal of Quantum Electronics **47**, 972 (2011).
6. **Satchi Kumari** and Alika Khare, "*Epitaxial ruby thin film based photonic sensor for temperature measurement*", Review of Scientific Instruments **82**, 066106 (2011).

To be Communicated

1. **Satchi Kumari** and Alika Khare,*"Sub and superluminal pulse propagation in thin film of Ruby via degenerate two-wave mixing"*.
2. **Satchi Kumari** and Alika Khare, "*A comparative study of spatial distribution of plasma parameters along and perpendicular to plasma flow direction via planar Langmuir probe*".
3. **Satchi Kumari** and Alika Khare, "*Optical nonlinearity in epitaxial ruby thin film*".
4. **Satchi Kumari** and Alika Khare, *"pulsed laser deposited barium titanate thin film as Raman temperature sensor"*.
5. **Satchi Kumari** and Alika Khare, "*correlation between plasma parameters and PLD Thin Films of Ruby (Al_2O_3: Cr^{3+})"*.

Conference presentation

1. **Satchi Kumari** and Alika Khare, "*Temperature Dependent Raman Studies of Barium Titanate Thin Film Deposited via Pulsed Laser Deposition*", DAE-BRNS 6th national symposium on pulsed laser deposition of thin films and nanostructured materials, PLD-2011, IISc Bengaluru 9 -11th Nov. 2011
2. **Satchi Kumari** and Alika Khare, *"Effect of Background Oxygen Pressure on Pulsed Laser Deposited Thin Films of Ruby", DAE-BRNS 6th* national symposium on pulsed laser deposition of thin films and nanostructured materials, **PLD-2011**, MRS, IISc Bengaluru 9 -11th Nov. 2011

3. **Satchi Kumari,** Archana Kushwaha and Alika Khare, *"Langmuir Probe Studies of Laser Induced Ruby (Al_2O_3:Cr^{3+}) Plasma",* 26th National Symposium on Plasma Science & Technology, **PLASMA-2011,** BIT Patna 20-23rd Dec 2011, **(PSSI Poster Award).**
4. **Satchi Kumari** and Alika Khare, *"Effect of Laser Fluence on Pulsed Laser Deposited Thin Films of Ruby",* 26th National Symposium on Plasma Science & Technology, **PLASMA-2011,** BIT Patna 20-23rd Dec 2011.
5. Archana Kushwaha, **Satchi Kumari** and Alika Khare, "*Effect of Excitation intensity on Two photon induced UV Photoluminescence in ZnO thin films using He:Ne laser*", **PLD-2011**, MRS, IISc Bengaluru 9 -11th Nov. 2011.
6. **Satchi Kumari,** *Archana Kushwaha* and Alika Khare, *"Spatial distribution of electron temperature and Ion density in laser induced ruby plasma using Langmuir probe",* 15th International symposium on Laser aided plasma diagnostics, **LAPD-15,** jeju, Korea, 9-13th Oct 2011 (Oral presentation).
7. **Satchi Kumari** and Alika Khare, *"Tetragonal Barium Titanate Thin Film via Pulsed Laser Deposition Technique", CMDAYS* Guwahati, Aug 24-26th 2011.
8. **Satchi Kumari** and Alika Khare, *"Effect of crystal orientation on temporal delay in Ce: $BaTiO_3$ via degenerate two-wave mixing",* INTERNATIONAL CONFERENCE ON CONTEMPORARY TRENDS IN OPTICS AND OPTOELECTRONICS, IIST Thiruvananthapuram, January 17-19th 2011.
9. **Satchi Kumari** and Alika Khare, *"Determination of the crystallographic orientations of Ce:$BaTiO_3$ Titanate crystal via backward two-wave mixing",* INTERNATIONAL CONFERENCE ON CONTEMPORARY TRENDS IN OPTICS AND OPTOELECTRONICS, IIST Thiruvananthapuram , January 17-19th 2011.

10. **Satchi Kumari** and Alika Khare, *"Slowing down of light in Ce:BaTiO$_3$ crystal via Degenerate two-wave mixing using chopped pulses*", **Photonics 2010** ~ international Conference on Fiber Optics & Photonics , IIT Guwahati Dec. 2010.
11. **Satchi Kumari** and Alika Khare, *"Pulsed Laser Deposited Ruby Thin Film as Temperature Sensor",* 25th National Symposium on Plasma Science & Technology (**PLASMA-2010**).
12. **Satchi Kumari** and Alika Khare, *"Photoluminescence Studies of Pulsed laser deposited thin films of Ruby",* 4th National Symposium on Plasma Science & Technology (**PLASMA-2009**), NIT Hamirpur (HP) 8-11th Dec, 2009.
13. **Satchi Kumari** and Alika Khare, *"Thin film of ruby by pulsed laser deposition technique"*, **RACMP 09** NIT Hamirpur (23-24 may 2009).

School /Workshop Attended

1. Quality Improvement Programme on Computational techniques in physics, 1st - 6th august, 2011 at Indian Institute of Technology Guwahati (India).
2. SERC Preparatory School on Modern Optics, 10 rd -23rd November, 2010 at Indian Institute of Technology Guwahati (India).
3. DST-SERC School on Plasma Diagnostics, 20st-31st July, 2009 at Institute for Plasma Research, Gandhinagar (India).
4. National workshop on plasma-surface interactions and processing (NWPSIP-09), 25th -27th May, 2009 at NIT Hamirpur, Himachal Pradesh (India).